Multiple scattering theory for the description of defects in metallic alloys and oxide systems

Dissertation

zur Erlangung des Doktorgrades der Naturwissenschaften
(*Dr. rer. nat.*)

der

Naturwissenschaftlichen Fakultät II
Chemie, Physik und Mathematik

der Martin-Luther-Universität
Halle-Wittenberg

vorgelegt von

Herrn Martin Hoffmann

geb. am 25. Dezember 1984 in Querfurt

Gutachter:

- Prof. Dr. Wolfram Hergert
- PD Dr. Semjon Stepanow
- PD Dr. Manuel Richter

Die Verteidigung fand am 31. März 2016 statt.

Contents

List of abbreviations

ASA atomic sphere approximation

ASD antisite disorder

ATA Average t matrix approximation

BS Bounding sphere

BSF Bloch spectral function

CFP Crystal field parameter

CPA coherent potential approximation

DLM Local moment theory

DMI Dzyaloshinskii-Moriya interaction

DOS Density of states

ED Exact diagonalization

E_F Fermi energy

EMTO Exact muffin-tin orbital method

ETT electronic topological transitions; also Lifshitz transitions

fcc face-centered cubic

FCDA Full-charge density approximation

GF Green's function

GGA Generalized gradient approximation

hcp hexagonal closed packed

IS Intermediate spin

LDA Local density approximation

LDOS Local density of states

LRO Long-range order

LRO Long-range order

MAE Magnetic anisotropy energy

MC Monte Carlo

MFA Mean-field approximation

MOPW Modified orthogonalized plane wave method

MS-CPA Multi-sublattice CPA

MS-NL-CPA Multi-sublattice non-local CPA

MT Muffin-tin

MTJ Magnetic tunnel junction

PDOS Partial density of states

PES photoemission spectroscopy

RS_{FM} Ferromagnetic reference state

RS_{PM} Paramagnetic reference state

sc simple cubic

SCO $SrCoO_3$

SFMO Sr_2FeMoO_6

SIC Self-interaction correction

sp-STM Spin-polarized surface tunneling microscopy

SRO Short-range order

SRO Short-range order

V_O Oxygen vacancy; oxygen deficiency

WSC Wigner-Seitz cell

Chapter 1.

Introduction

Materials research has a crucial role in the development of many technical applications used in our daily life. The composition and structure of the built-in materials became in the last years more and more involved, and their accessible length scales much smaller. In particular, fundamental research is searching for the understanding of the basic principles of such complex materials and their properties. Besides the experimental investigations and findings, theoretical models and first-principles calculations can largely contribute to the materials sciences concerning predictions or further atomistic understanding.

This thesis reports the results of the theoretical investigation focused on the influence of defects at different dimensions and length scales on crucial material properties. Depending on the dimension of the system, the defects might have different degrees of freedom to occupy different sites in a lattice structure. Their relative positions can be completely uncorrelated, limited to a particular lattice site, or anything in between. This variation in different disorder regimes was the main topic of this thesis (see figure 1.2). I used for the computation mainly the Green's function method HUTSEPOT [1]. The Green's function (GF) method proved to describe reliably magnetic properties and can cover the different defect problems and describe well physical properties of materials, as the result sections will show.

Among many other interesting topics, the research has been focused in the last years on the improvement of computational hardware like its data storage capacity, the methods of data storage, weight reduction or reduction in energy consumption and unwanted heat emission. Since these hardware elements became more and more microscopic, atomistic understanding and basic research is critical. Here the possible research topics have increased continuously with strong developments in measurement, material characterization, and growing techniques. For example, the spin-polarized surface tunneling microscopy (sp-STM) allows nowadays to investigate single magnetic atoms on a metallic surface [E11]. Such magnetic adatoms are discussed in the context of tiny magnetic memories and need a high magnetic moment with a high stability. In the past, the electronic states of the typical transition metal adatom hybridized with those of the surface and the stability was quickly lost [2–6]. This hybridization was overcome, e.g., in larger clusters [2, 3] or insulating buffer layers [4–6]. However, it is shown that the large magnetic moments of the rare-earth atoms like Holmium might be in particular well suited for a stable magnetic orientation [E11]. In particular, the magneto-crystalline anisotropy of the underlying threefold symmetry of the considered Pt surface plays a crucial role for the long lifetime observed in recent experiments. The strongly localized f-states of Holmium made it necessary to take into account the general crystal-field Hamiltonian. The theo-

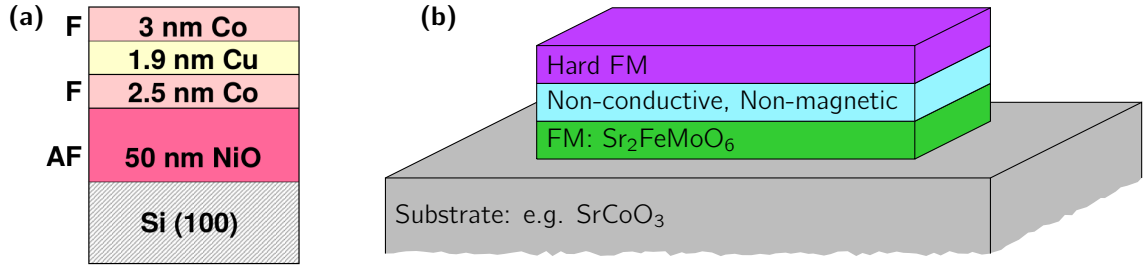

Figure 1.1: (a) Experimental realization of a spin-valve with metallic thin films [9], (b) A possible magnetic tunnel junction built from oxide thin films.

retical calculation of the crystal-field parameters was implemented into HUTSEPOT. The Green's function method allows in the context of the multiple scattering theory the description of a single impurity in a perfect host system with the embedded cluster model [7]. Therein, a single adatom has no degree of freedom in terms of a disordered defect (see figure 1.2).

Magnetic properties also became important for spintronic applications. They may reduce the electrical current inside the computer hardware that would also reduce Joule heating and allow smaller structures in, e.g, transistors. Additionally, spintronic devices are extremely sensitive to changing magnetic fields, and they are used as magnetic field sensors in our daily live. Such devices, e.g., spin valves or magnetic tunnel junctions (MTJ) use the giant magnetoresistance or tunnel magnetoresistance effect, respectively [8]. Both devices use the spin-dependent scattering of electron currents at material interfaces. In figure 1.1, two possible realizations are sketched. They consist of two ferromagnetic (FM) layers separated by a non-magnetic layer, either conductive or not. The magnetic orientation in one layer is pinned (hard magnetization) while the other should switch more easily (soft magnetization). In a magnetic field, the magnetization of the soft FM layer can switch, and the difference in the magnetization directions of the two layers can be detected by an electric current. The magnetic pinning can be realized either by a higher magnetic coercitivity in one material with the hard magnetization or via the exchange coupling at the interface with an antiferromagnetic film (see figure 1.1a).

The sensitivity of a spin valve structure depends on the strength of the magnetoresistance effect. In a simple model, the tunnel magnetoresistance effect is [8]

$$\mathrm{TMR} = \frac{P_1 P_2}{1 - P_1 P_2} \tag{1.1}$$

with P_1 and P_2, the spin polarizations of the density of states of the two magnetic electrodes, respectively. Thus, a high spin polarization is crucial. Besides other materials, several complex oxide compound show half-metallic characteristics, e.g., Zn-Ferrite $ZnFe_2O_4$ or the double perovskite Sr_2FeMoO_6 (SFMO). The usage of the latter is sketched in figure 1.1b. Since the lattice of the oxides often mismatches with those of the common substrates like Si, a conductive oxide with the perovskite lattice structure, e.g., $SrCoO_3$ (SCO), might be used as an electrode.

For these two complex oxides systems – SCO and SFMO – I used the Green's function method to have deeper insight into the magnetic coupling mechanisms, the dependencies

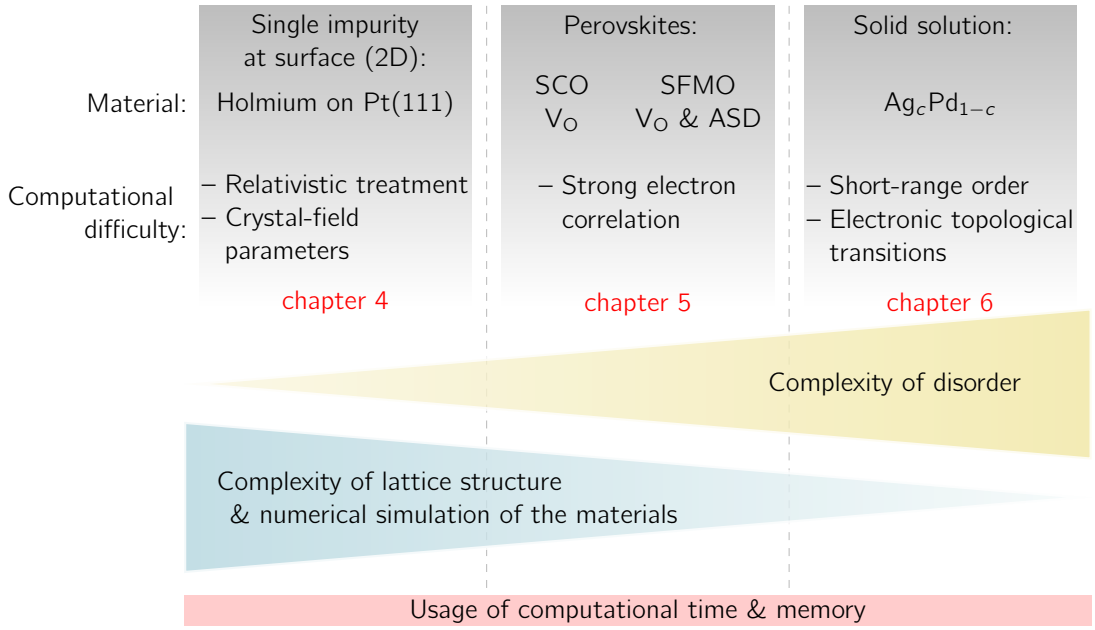

Figure 1.2: Schematic picture of the stepwise improvement in the description of disorder for the considered materials. On the other hand, the completely of the investigated material system had to be lowered in order to stay at a reasonable level of computational effort.

of the magnetic moments and the magnetic transition temperatures of oxide materials. Additionally, these properties vary under a chemical disorder, atomic deficiency or structural changes. Oxygen deficiency (oxygen vacancy – V_O) is for example quite typical for all oxide materials and reduces in SCO the Curie temperature T_C [10]. On the other hand, the high Curie temperature of the SFMO bulk samples (420 K to 450 K) [11–14] is desired for possible applications as spin valves or MTJ but lost as soon as SFMO is grown as a thin film ($T_C \approx 300$ K) [15, 16]. Epitaxial strain resulting from the surface or a swap of an Fe ion to a site of a Mo ion and vice versa (antisite defect or antisite disorder – ASD) were discussed besides the always present V_O as an origin for this reduction. ASD is typical for double perovskite materials ($Sr_2BB'O_6$) where the oxygen environment around the transition metal atoms B or B' is similar, and a switch of sites is very likely.

These defects are usually point defects in a perfect crystal and can be included in theoretical calculations. Larger lattice imperfections like stacking faults or dislocations are much harder to investigate by *ab initio* methods and were neglected in this work. However, they might also influence the magnetic properties. Anyway, point defects are usually considered in a supercell, e.g., for SFMO in the work of Muñoz-García *et al.* [17]. This allows already a detailed look into local properties but completely neglects possible disorder of those defects. The concept of multiple scattering theory offers in a quite natural way the opportunity to include randomly distributed point defects. They are included in an effective medium in the coherent potential approximation (CPA) [18, 19]. For SCO, an increase of oxygen vacancies reduces the magnetic transition temperature [E4], which agreed well with the experiments [10]. In contrast, the simulations show an

increase of T_C with more oxygen vacancies for SFMO [E2, E3].

Nevertheless, the description of the point defects in the two oxide materials within the CPA presents only an completely uncorrelated regime of disordered defects (see figure 1.2). The numerical results are reasonable only at the low concentration limit, since the lattice structure might become unstable for higher amounts of oxygen vacancies. This instability was shown, e.g., of SCO [20]. Beside, as a single-site approximation, the CPA completely neglects potential short-range order (SRO). Hence, there are possible extensions described in the literature. In HUTSEPOT, the multi-sublattice non-local CPA (MS-NL-CPA) is implemented [21] but it has a large numerical effort in respect of calculation time and memory. Therefore, I did not study the influence of SRO for a complex oxide but rather for the simple nonmagnetic alloy system Ag_cPd_{1-c} (see figure 1.2). This investigation was focused only on the electronic structure and the structural equilibrium properties [E12].

At first, two basic ordering regimes were studied. The CPA was used to model the whole concentration range of the AgPd alloy. The change of the elastic properties in dependence of chemical disorder agreed well with previous CPA calculations within the EMTO method [E12, 22, 23]. On the other hand, Müller and Zunger [24] proposed the ordered phases of Ag_cPd_{1-c} at particular alloy compositions $c_{Ag} = 0.25$, 0.5 and 0.75. The MS-NL-CPA allowed an interpolation between these ordered phases simulating the tendency of long-range order (LRO) over the whole concentration range.

Both SRO regimes, uncorrelated disorder or LRO, were compared to each other. Their elastic properties show a characteristic deviation from the linear dependence (Vegard's law [25]). In general, such a deviation might be connected to substantial variations in the electronic structure, changes in the connectivity of the Fermi surface – called Lifshitz transitions or electronic topological transitions (ETT). Based on the their restricted computational possibilities, Bruno *et al.* [26–28] showed this connection only for few concentrations and with possible numerical uncertainties. The connection could be verified with HUTSEPOT for a larger concentration range in Ag_cPd_{1-c} [E12].

Then, the effect of a particular SRO regime on the electronic structure was investigated. The different disorder regimes caused variations in the density of states (DOS), which might be large enough to be visible in valence photoemission spectroscopy (PES) experiments. This introduces new ways to investigate SRO via PES and numerical calculations.

This thesis is organized into five chapters and ends with a conclusion in chapter 7. The following chapter 2 summarizes the basic computational details used in the thesis – the basics of the DFT, the multiple scattering theory, and the Monte Carlo method. More advanced numerical methods for the explicit derivation of particular physical observables are addressed in chapter 3. As the overview in figure 1.2 visualizes, the results were discussed beginning with the low dimensional system, the Holmium adatoms on platinum (chapter 4). The magnetic properties of the two complex oxides and their changes due to point defects are discussed in chapter 5, while chapter 6 contains the results for the Ag-Pd alloy system and its electronic structure.

Chapter 2.

Theoretical Basics

2.1. First-principles methodology

Like any first-principles or *ab initio* method, the Green's function method solves the quantum mechanical many-body problem for an arrangement of atoms build from a nucleus and electrons. Although a parameter-free solution without any approximation would be favored, some approximations are needed due to the huge number of degrees of freedom when using a realistic number of atoms. The Born-Oppenheimer (adiabatic approximation) assumes the positions in the ensemble $\{\alpha\}$ of the N_n nuclei as fixed during the timescale of the electronic movements. The charge Z_α of the nuclei at the positions $\boldsymbol{R}_\alpha$, creates the potential

$$V_{\{\alpha\}}(\boldsymbol{r}) = -\sum_{\alpha}^{N_\mathrm{n}} \frac{2Z_\alpha}{|\boldsymbol{r} - \boldsymbol{R}_\alpha|} \,. \tag{2.1}$$

With this adiabatic approximation, the stationary Schrödinger equation can written as

$$\widehat{H}_{\{\alpha\}} \boldsymbol{\Psi} = E \boldsymbol{\Psi} \,, \tag{2.2}$$

with the Hamiltonian

$$\widehat{H}_{\{\alpha\}} = \underbrace{-\sum_{i}^{N_\mathrm{e}} \nabla_i^2}_{T_\mathrm{e}} + \underbrace{\sum_{i}^{N_\mathrm{e}} \left(V_{\{\alpha\}}(\boldsymbol{r}_i) + \widetilde{V}_\mathrm{ext} \right)}_{V_\mathrm{ext}} + \underbrace{\sum_{\substack{i,j \\ i \neq j}}^{N_\mathrm{e}} \frac{1}{|\boldsymbol{r}_i - \boldsymbol{r}_j|}}_{V_\mathrm{ee}} \,, \tag{2.3}$$

for all N_e electrons (written in atomic units)[1] and the wave function of the N_e electrons at $\boldsymbol{r}$ with the spin s

$$\boldsymbol{\Psi}(\boldsymbol{r}_1, s_1, \boldsymbol{r}_2, s_2, \ldots, \boldsymbol{r}_{N_\mathrm{e}}, s_{N_\mathrm{e}}) \,. \tag{2.4}$$

The terms in (2.3) represent the kinetic energy of the electrons T_e, the external potential combined with the potentials from the atomic cores V_ext and the electrostatic interaction between all electrons V_ee. In this context only the time-independent, non-relativistic

[1] It is $\hbar = 1$, $m = 1/2$ and $\frac{e^2}{4\pi\varepsilon_0} = \epsilon^2 = 2$. The length scales are given in Bohr radius a_B. The energy is given in Rydberg (1 Ryd).

Schrödinger equation is discussed because the main topics of this thesis are ground state properties for light elements.

Since the number of electrons is too large to solve this equation directly, there are several models developed. The first model – the Thomas-Fermi model [29, 30] – divides the system into different cells and assumes for each of them a homogeneous electron density. The problem can be also solved approximating $\boldsymbol{\Psi}$ with a product of single electron wave functions $\psi_i(\boldsymbol{r}, s)$, as suggested by Hartree [31]. Nevertheless, the Pauli principle should be valid and can be realized in the Hartree-Fock approximation [32] with a Slater determinant of single-electron wave functions

$$\boldsymbol{\Psi} \approx \frac{1}{\sqrt{N_\mathrm{e}}} \begin{vmatrix} \psi_1(\boldsymbol{r}_1, s_1) & \cdots & \psi_1(\boldsymbol{r}_{N_\mathrm{e}}, s_{N_\mathrm{e}}) \\ \vdots & \ddots & \vdots \\ \psi_{N_\mathrm{e}}(\boldsymbol{r}_1, s_1) & \cdots & \psi_{N_\mathrm{e}}(\boldsymbol{r}_{N_\mathrm{e}}, s_{N_\mathrm{e}}) \end{vmatrix} . \tag{2.5}$$

In those approximations, the electron density derived from the single electron wave functions

$$\varrho_s(\boldsymbol{r}) = \sum_i |\psi_i(\boldsymbol{r}, s)|^2 \tag{2.6}$$

plays a fundamental role.[2]

2.1.1. Basics of density functional theory

The density functional theory (DFT) gives the connection between the ground state and the electron density $\varrho(\boldsymbol{r})$. Therewith, all the degrees of freedom in the all-electron wave function (2.4) are reduced to only the three parameters x, y, and z of the real space coordinate $\boldsymbol{r}$. This connection is based on two theorems proved by Hohenberg and Kohn [33]:

- for each $V_\mathrm{ext}(\boldsymbol{r})$ exists the total energy as a functional of the charge density $\widehat{E}[\varrho]$,
- $\widehat{E}[\varrho]$ fulfills the variational principle

  $$\widehat{E}[\varrho(\boldsymbol{r})] \geq \widehat{E}[\varrho_0(\boldsymbol{r})] = E_0 \,, \tag{2.7}$$

  where E_0 is the ground state total energy as long as $\varrho_0(\boldsymbol{r})$ is the exact charge density describing the real system.

Consequently, all physical observables of the system, which are the expectation values of the corresponding operators with the wave function, are functionals of the electron density. In particular, the total energy in (2.2) becomes a functional

$$\widehat{E}[\varrho] = \underbrace{\widehat{T}[\varrho] + \widehat{V}_\mathrm{ee}[\varrho]}_{=:\widehat{F}[\varrho]} + \int V_\mathrm{ext}(\boldsymbol{r})\varrho(\boldsymbol{r})\mathrm{d}\boldsymbol{r} \,, \tag{2.8}$$

with the contribution of the external potentials. The functionals of the kinetic energy and the electron-electron interaction are combined to $\widehat{F}[\varrho]$. The exact form of the electron-electron interaction functional is not known explicitly. The Hohenberg-Kohn theorems do not state a method how to achieve the ground state density.

[2] The spin index s of the charge density is only written when it is explicitly needed.

2.1.2. Kohn-Sham equations

Kohn and Sham [34] used an effective single particle system

$$\widehat{H}_{\mathrm{KS}} = -\nabla^2 + V_{\mathrm{eff}}(\boldsymbol{r}) \,, \tag{2.9}$$

which behaves like a non-interacting electron system. The wave function is again the Slater determinant and the exact electron density is recovered

$$\varrho_s(\boldsymbol{r}) = \sum_i^N |\psi_i(\boldsymbol{r}, \boldsymbol{s})|^2 \,. \tag{2.10}$$

Due to the non-interacting electrons, the kinetic energy as an expectation value with the single electron wave functions

$$T_{\mathrm{KS}} = \sum_i^N \left\langle \psi_i \left| -\nabla^2 \right| \psi_i \right\rangle \,, \tag{2.11}$$

is not exactly $\widehat{T}[\varrho]$ from (2.8). Its difference is combined with all non-classical terms of the electron-electron interactions into the exchange-correlation energy term

$$\widehat{F}[\varrho] = T_{\mathrm{KS}} + \iint \frac{\varrho(\boldsymbol{r})\varrho(\boldsymbol{r}')}{|\boldsymbol{r} - \boldsymbol{r}'|} \mathrm{d}\boldsymbol{r}\, \mathrm{d}\boldsymbol{r}' + \widehat{E}_{\mathrm{xc}}[\varrho] \,. \tag{2.12}$$

By means of the variation of the charge density

$$\frac{\partial \widehat{E}[\varrho]}{\partial \varrho(\boldsymbol{r})} = \frac{\partial T_{\mathrm{KS}}}{\partial \varrho(\boldsymbol{r})} + \underbrace{V_{\mathrm{ext}}(\boldsymbol{r}) + 2\int \frac{\varrho(\boldsymbol{r}')}{|\boldsymbol{r} - \boldsymbol{r}'|} \mathrm{d}\boldsymbol{r}' + \frac{\partial \widehat{E}_{\mathrm{xc}}[\varrho]}{\partial \varrho(\boldsymbol{r})}}_{V_{\mathrm{eff}}(\boldsymbol{r})} = \mu \,. \tag{2.13}$$

Thereby, Lagrange multiplier μ conserves the number of particles.

The single particle system (2.9) is determined by the effective potential $V_{\mathrm{eff}}(\boldsymbol{r})$ in (2.13) and it will return the exact single particle electron density $\varrho(\boldsymbol{r})$ (2.10). The latter, however, is not known but it can be obtained iteratively by using (2.9) and a starting density $\varrho_\nu(\boldsymbol{r})$ for $V_{\mathrm{eff}}(\boldsymbol{r})$ in

$$\widehat{H}_{\mathrm{KS}} \psi_\nu(\boldsymbol{r}) = \epsilon \psi_\nu(\boldsymbol{r}) \,. \tag{2.14}$$

A new density $\varrho_{\nu+1}(\boldsymbol{r})$ is calculated from the obtained wave function $\psi_\nu(\boldsymbol{r})$ with (2.10) and yields a new $V_{\mathrm{eff}}(\boldsymbol{r})$ for (2.14). These calculation steps are repeated until the difference between the charge densities

$$|\varrho_\nu(\boldsymbol{r}) - \varrho_{\nu+1}(\boldsymbol{r})| < \delta \,, \tag{2.15}$$

reaches a given accuracy δ.

2.1.3. Formulation within the multiple scattering theory

The multiple scattering theory leads in a natural way to the Green's function of the system. In general, a Green's function can be used to solve any inhomogeneous differential equation of the type [35]

$$[\varepsilon - \widehat{L}(\boldsymbol{r})]G(\varepsilon;\boldsymbol{r},\boldsymbol{r}') = \delta(\boldsymbol{r}-\boldsymbol{r}')\,. \tag{2.16}$$

The variable ε is complex with the eigenvalues $\lambda \equiv \mathrm{Re}\{\varepsilon\}$ and $\widehat{L}(\boldsymbol{r})$ is a time-independent, linear, hermitian differential operator with a complete set of eigenfunctions $\{\phi_n(\boldsymbol{r})\}$

$$\widehat{L}(\boldsymbol{r})\phi_n(\boldsymbol{r}) = \lambda_n\phi_n(\boldsymbol{r})\,. \tag{2.17}$$

The Hamiltonian (2.14) is obviously a similar kind of differential equation as (2.17) and can be solved with a Green's function approach [35, section 3]. The values ε represent complex energies. The usage of Dirac's bra $\langle\boldsymbol{r}|$ and ket $|\boldsymbol{r}\rangle$ notation of the position operator $\langle\boldsymbol{r}|G(\varepsilon)|\boldsymbol{r}'\rangle = G(\varepsilon;\boldsymbol{r},\boldsymbol{r}')$ allows a simpler equation

$$(\varepsilon - \widehat{H}_{\mathrm{KS}})G(\varepsilon) = 1 \;\Rightarrow\; G(\varepsilon) = (\varepsilon - \widehat{H}_{\mathrm{KS}})^{-1}\,. \tag{2.18}$$

If the effective potential in (2.9) or any kind of potential V is considered as a perturbation of the undisturbed Hamiltonian $\widehat{H}_0 = -\nabla^2$, two Green's functions can be derived

$$G_0(\varepsilon) = (\varepsilon - \widehat{H}_0)^{-1} \;\Rightarrow\; (\varepsilon - \widehat{H}_0) = G_0(\varepsilon)^{-1}\,, \tag{2.19}$$

$$G(\varepsilon) = (\varepsilon - \widehat{H}_{\mathrm{KS}})^{-1} \;\Rightarrow\; (\varepsilon - \widehat{H}_{\mathrm{KS}}) = (\varepsilon - \widehat{H}_0 - V) = G(\varepsilon)^{-1}\,. \tag{2.20}$$

By plugging (2.19) into (2.20) a Dyson equation is obtained [36, section 3.1.2]

$$G(\varepsilon) = G_0(\varepsilon)\left[1 - VG_0(\varepsilon)\right]^{-1} = \left[1 - G_0(\varepsilon)V\right]^{-1} G_0(\varepsilon)\,, \tag{2.21}$$

$$= G_0(\varepsilon) + G(\varepsilon)VG_0(\varepsilon) = G_0(\varepsilon) + G_0(\varepsilon)VG(\varepsilon)\,. \tag{2.22}$$

The latter equation defines an infinite Born series (iterative solution). With the so-called T-operator or scattering matrix T,

$$T(\varepsilon) = V + VG_0(\varepsilon)V + VG_0(\varepsilon)VG_0(\varepsilon)V + \dots\,, \tag{2.23}$$

the Dyson equation can be reformulated to

$$G(\varepsilon) = G_0(\varepsilon) + G_0(\varepsilon)T(\varepsilon)G_0(\varepsilon)\,. \tag{2.24}$$

For a single scattering potential at site n, the single-site T-operator, also called t matrix, is defined by

$$t^n(\varepsilon) = V_n + V_nG_0(\varepsilon)t^n\,. \tag{2.25}$$

The latter equation accounts for the electron scattering at a single potential (see blue lines in figure 2.1). Thus, the T-operator for an ensemble of N scatterers can be rewritten in terms of this single-site T-operator

$$T(\varepsilon) = \sum_n t^n(\varepsilon) + \sum_{n,m} t^n(\varepsilon)G_0(\varepsilon)(1-\delta_{nm})t^m(\varepsilon) + \\ + \sum_{n,m,k} t^n(\varepsilon)G_0(\varepsilon)(1-\delta_{nm})t^m(\varepsilon)G_0(\varepsilon)(1-\delta_{mk})t^k(\varepsilon) + \dots\,, \tag{2.26}$$

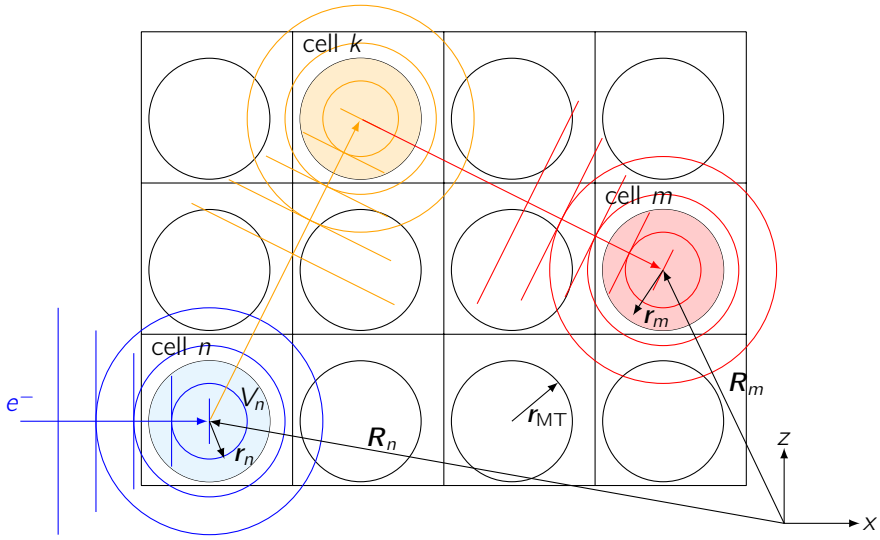

Figure 2.1: Schematic picture of the electronic scattering described by the multiple scattering theory for a periodic lattice of spherical potentials V_n. The potentials do not overlap with each other and have the muffin-tin radius $\boldsymbol{r}_{\mathrm{MT}}$. A plane wave is scattered at the potential in cell n and emits a spherical wave (blue lines). The resulting wave can be again scattered, e.g, at cell k towards cell m (orange and red lines). The uppercase vector $\boldsymbol{R}_n$ points to the origin of the potential. The lowercase vector $\boldsymbol{r}_n$ describes a point inside the potential.

whereas this scattering operator can be rewritten in terms of the scattering path operator $\tau^{nm}(\varepsilon)$ [36, section 3.3.3]

$$T(\varepsilon) = \sum_{n,m} \tau^{nm}(\varepsilon)\,. \tag{2.27}$$

The scattering path operator fulfills again a Dyson equation

$$\tau^{nm}(\varepsilon) = t^n(\varepsilon)\delta_{nm} + \sum_k t^n(\varepsilon) G_0(\varepsilon)(1-\delta_{nk})\tau^{km}(\varepsilon)\,, \tag{2.28}$$

and describes the scattering path from the potential in cell n to the potential in cell m via several other potentials symbolized as the one in the cell k (see figure 2.1). In addition, also the Green's function can be expressed with (2.28)

$$G(\varepsilon) = G_0(\varepsilon) + \sum_{n,m} G_0(\varepsilon)\tau^{nm}(\varepsilon)G_0(\varepsilon)\,. \tag{2.29}$$

Thus, either the Green's function or the scattering path operator can be used for the full description of the scattering in the system.

For the practical solution, the above formalism is written in an angular momentum and partial wave representation. All quantities are expressed as matrices in terms of the eigenfunctions of the angular momentum operators, the spherical harmonics $Y_L(\hat{\boldsymbol{r}})$ with $L = (l, m)$, and the Bessel, Neumann and Hankel–functions [36, section 3.4.5]. The matrices with an angular momentum index are combined for all sites into a single matrix, a

so-called supermatrix. The multiple indices of a supermatrix are indicated by underlining. Thereby, the matrices for the scattering path operator (2.28), the single-site scattering matrix (2.25), and the so-called *bare structure constants* $G_0(\varepsilon)$ are written as

$$\underline{\tau}(\varepsilon) = \{\tau^{nm}_{LL'}(\varepsilon)\} \tag{2.30}$$
$$\underline{t}(\varepsilon) = \{t^{n}_{LL'}(\varepsilon)\} \tag{2.31}$$
$$\underline{G}_0(\varepsilon) = \{G^{nm}_{0,LL'}(\varepsilon)(1-\delta_{nm})\} \tag{2.32}$$

It follows the *main equation* of the Green's function method [1, 36]

$$\underline{\tau}(\varepsilon) = [\underline{t}^{-1}(\varepsilon) - \underline{G}_0(\varepsilon)]^{-1}\,. \tag{2.33}$$

The latter equation visualizes the separation of the structural and chemical contributions at the different sites, since the quantity $\underline{G}_0(\varepsilon)$ contains all the information of the lattice without the potentials (see (2.19)), whereas the information of the chemical compound is included in $\underline{t}(\varepsilon)$ via the potentials (see (2.25)). In addition, this formalism allows the description of disorder as a logical consequence as described in section 3.4, but complicates the calculation of the position dependent properties like structural relaxations or phonon spectra.

2.1.4. Potentials in the Green's function method

In the GF method, the potentials in the single-site scattering matrix (2.25) are included by different concepts. The simplest assumption for those potentials is a collection of regularly arranged, spherically symmetric *muffin-tin* (MT) potentials with the radius r_{MT}, which do not overlap with each other (see underlying spheres in figure 2.1).

However, Gonis showed that all equations discussed in section 2.1.3 are also valid for overlapping and arbitrarily shaped potentials [37]. This allowed a representation of the potentials, e.g., with the atomic sphere approximation (ASA). In the ASA, the radius of the spherical potentials at every site is chosen such that the sphere volume is the same as the volume of the Wigner-Seitz cells (WSC) at the corresponding site.

On the other hand, a full-potential implementation is also possible in the GF method but demands very large computational resources. A simplified version of this full-potential approach, the so-called full-charge density approximation (FCDA), can be used. It is based on the work of Kollar, Vitos, and Skriver [38]. The convex polyhedra for the WSC with the volume Ω is build by a Voronoi cell construction [39]. A shape function is introduced to take into account the non-spherical shape of the WSC [36, section 4]

$$\sigma(\boldsymbol{r}) = \begin{cases} 1 & \boldsymbol{r} \in \Omega \\ 0 & \boldsymbol{r} \notin \Omega \end{cases}\,. \tag{2.34}$$

It has to be expanded into spherical harmonics

$$\sigma(\boldsymbol{r}) = \sum_L \sigma_L(r) Y_L(\hat{\boldsymbol{r}})\,, \tag{2.35}$$

with the coefficients

$$\sigma_L(r) = \int_\Omega \mathrm{d}\boldsymbol{r}\, \sigma(\boldsymbol{r}) Y_L^*(\hat{\boldsymbol{r}})\,. \tag{2.36}$$

The FCDA was used throughout this thesis to improve the accuracy of the calculations for complex unit cell geometries.

2.1.5. The choice of the exchange-correlation functional

The exact form of the exchange-correlation functional in (2.13) was so far not necessary for the theoretical methodology. Since it is unknown for complex systems, there is only an approximation possible. In this work, unless otherwise stated, the very reliable generalized gradient approximation (GGA) by Perdew-Burke-Ernzerhof (PBE) [40] was used. Other approximations like the local density approximation (LDA) of Perdew and Wang [41] or variations of the generalized gradient approximation (e.g. PBEsol [42]) were always tested beforehand but showed no qualitative changes in the electronic or magnetic properties of the investigated material systems in chapter 4 or 5. On the other hand, the differences in the exchange-correlation functionals became more critical in the context of equilibrium properties discussed in more detail in chapter 6. Therein, the numerical results obtained for different exchange functionals are compared with each other.

2.2. Monte Carlo Simulations

Another basic computational concept used in this work was the Monte Carlo (MC) simulation technique from statistical physics. It was applied to calculate averaged properties of a model Hamiltonian $\widehat{H}$. This model Hamiltonian was in particular the Heisenberg Hamiltonian, which is more elaborately discussed in section 3.3.1. Nevertheless, the underlying concepts of the statistical physics in the Monte Carlo method are applied to many different topics. They will be recalled briefly in the following.

The averaged total energy of the system with N sites is (see e.g. [43, section 5.3])

$$\overline{E} = \langle \widehat{H} \rangle_T / N\,, \tag{2.37}$$

with the thermal average in the canonical ensemble $\langle \cdot \rangle_T$. The thermal average is expressed as a phase space integral for any physical observable $A(\boldsymbol{c})$ with its degrees of freedom collected into a single vector $\boldsymbol{c}$. Thereby, $A(\boldsymbol{c})$ can be, e.g., the Hamiltonian itself $A = \widehat{H}$, or the total magnetic moment $A = \sum_i^N \boldsymbol{m}_i$. The phase space for $\sum_i^N \boldsymbol{m}_i$ is spanned by all the magnetic moments sitting at the lattice sites, so a vector of a certain configuration of magnetic moments would be $\boldsymbol{c} = (\boldsymbol{m}_1, \boldsymbol{m}_2, \ldots, \boldsymbol{m}_N)$. The phase space integral over

the ensemble $\{\boldsymbol{c}\}$ of all $\boldsymbol{c}$ gives the thermal average

$$\langle A(\boldsymbol{c})\rangle_T = \frac{1}{Z}\int \mathrm{d}\boldsymbol{c}\, \underbrace{\exp\left(-\frac{\widehat{H}(\boldsymbol{c})}{k_\mathrm{B}T}\right)}_{p^*(\boldsymbol{c}):=} A(\boldsymbol{c})\,, \tag{2.38}$$

$$Z = \int \mathrm{d}\boldsymbol{c}\, \exp\left(-\frac{\widehat{H}(\boldsymbol{c})}{k_\mathrm{B}T}\right)\,. \tag{2.39}$$

Here the normalized Boltzmann factor $p(\boldsymbol{c}) = p^*(\boldsymbol{c})/Z$ acts like the probability density describing the statistical weight of the configuration $\boldsymbol{c}$.

As a starting point, the integral over $\{\boldsymbol{c}\}$ is substituted by a sum over a subset of phase space points (a set of N_MC points), called *simple sampling* [43, section 2.1.2]

$$\langle A(\boldsymbol{c})\rangle_T \approx \overline{A(\boldsymbol{c})} = \frac{\sum_{l=1}^{N_\mathrm{MC}} \exp\left(-\widehat{H}(\boldsymbol{c}_l)/k_\mathrm{B}T\right) A(\boldsymbol{c}_l)}{\sum_{l=1}^{N_\mathrm{MC}} \exp\left(-\widehat{H}(\boldsymbol{c}_l)/k_\mathrm{B}T\right)}\,. \tag{2.40}$$

As any statistical method, it can only be approximative. Unfortunately, the N_MC states in (2.40) has to be chosen randomly. It turns out that a simple random sampling technique generates the points in the phase space with a narrow Gaussian probability distribution, which is not useful for all temperatures [43, section 2.1.5]. Hence, a subset of phase space points from a regime, which is important at a certain temperature T, is needed. If such a subset is found according to the probability $P(\boldsymbol{c}_l)$, the simple sampling (2.40) can be substituted by

$$\overline{A(\boldsymbol{c})} = \frac{\sum_{l=1}^{N_\mathrm{MC}} \exp\left(-\widehat{H}(\boldsymbol{c}_l)/k_\mathrm{B}T\right) A(\boldsymbol{c}_l)/P(\boldsymbol{c}_l)}{\sum_{l=1}^{N_\mathrm{MC}} \exp\left(-\widehat{H}(\boldsymbol{c}_l)/k_\mathrm{B}T\right)/P(\boldsymbol{c}_l)}\,. \tag{2.41}$$

With the Boltzmann factor $p^*(\boldsymbol{c})$ as a choice for this probability function $P(\boldsymbol{c}_l)$, (2.41) reduces to a simple arithmetic average, the *importance sampling*,

$$\langle A(\boldsymbol{c})\rangle_T \approx \overline{A(\boldsymbol{c})} = \frac{1}{N_\mathrm{MC}}\sum_{l=1}^{N_\mathrm{MC}} A(\boldsymbol{c}_l)\,. \tag{2.42}$$

Metropolis *et al.* [44] used a Markov process, where the following state $\boldsymbol{c}_{l+1}$ is constructed from the previous one with a suitable transition probability $W(\boldsymbol{c}_l \to \boldsymbol{c}_{l+1})$. They showed that with $N_\mathrm{MC} \to \infty$ the distribution function $P(\boldsymbol{c}_l)$ tends towards $p(\boldsymbol{c})$. A proper condition is the principle of detailed balance

$$P_\mathrm{eq}(\boldsymbol{c}_l)W(\boldsymbol{c}_l \to \boldsymbol{c}_{l'}) = P_\mathrm{eq}(\boldsymbol{c}_{l'})W(\boldsymbol{c}_{l'} \to \boldsymbol{c}_l)\,, \tag{2.43}$$

which implies that the ratio between the two transition probabilities depends only on the energy change $\Delta\widehat{H} = \widehat{H}(\boldsymbol{c}_{l'}) - \widehat{H}(\boldsymbol{c}_l)$,

$$\frac{W(\boldsymbol{c}_l \to \boldsymbol{c}_{l'})}{W(\boldsymbol{c}_{l'} \to \boldsymbol{c}_l)} = \exp\left(-\frac{\Delta\widehat{H}}{k_\mathrm{B}T}\right)\,. \tag{2.44}$$

The transition probability W is not uniquely defined and a common choice is [44, 45]

$$W(\boldsymbol{c}_l \to \boldsymbol{c}_{l'}) = \min\left(1, \exp\left[-\frac{E_l - E_{l'}}{k_\mathrm{B}T}\right]\right) . \tag{2.45}$$

Chapter 3.

Calculation of Material Properties

3.1. Electronic structure from the Green's function

All relevant features of the electronic structure can be obtained directly from the calculated Green's function. In real space, the Green's function in the spectral representation between cell n and m is written as [36]

$$G(\varepsilon; \boldsymbol{r} + \boldsymbol{R}_n, \boldsymbol{r}' + \boldsymbol{R}_m) = \sum_{LL'} Y_L(\widehat{\boldsymbol{r}}) G^{nm}_{LL'}(\varepsilon; r, r') Y^*_{L'}(\widehat{\boldsymbol{r}}') \,, \tag{3.1}$$

with the complex energies ε, which have a small imaginary part, and the expansion coefficients

$$\begin{aligned} G^{nm}_{LL'}(\varepsilon; r, r') = & \sum_{L''L'''} Z_{LL''}(\varepsilon; r) \tau^{nm}_{L''L'''}(\varepsilon) Z_{L'L'''}(\varepsilon; r') \\ & - \sum_{L''} J_{LL''}(\varepsilon; r) Z_{L'L''}(\varepsilon; r) \,. \end{aligned} \tag{3.2}$$

The $G_{LL'}(\varepsilon; r)$ are expressed in terms of the regular and irregular scattering solutions $Z_{LL''}(\varepsilon; r)$ and $J_{LL''}(\varepsilon; r)$, respectively. All physical quantities, which are derived in the following, can be described by using only the diagonal parts of the Green's function (3.1)

$$G(\varepsilon; \boldsymbol{r} + \boldsymbol{R}_n) \equiv G(\varepsilon; \boldsymbol{r} + \boldsymbol{R}_n, \boldsymbol{r} + \boldsymbol{R}_n) \,, \tag{3.3}$$

$$G_{LL'}(\varepsilon; r) \equiv G^{nn}_{LL'}(\varepsilon; r, r) \,. \tag{3.4}$$

For example, the charge density[1] inside a particular cell n is defined as the imaginary part of an integral over the Green's function along a contour in the complex plain [36, section 18.2.1]

$$\varrho(\boldsymbol{r}) = -\frac{1}{\pi} \mathrm{Im} \int_{\curvearrowright} \mathrm{d}\varepsilon \, G(\varepsilon; \boldsymbol{r} + \boldsymbol{R}_n) \,. \tag{3.5}$$

By using the Gaunt coefficients

$$C^{L'}_{LL''} = \int \mathrm{d}\boldsymbol{r} \, Y_L(\widehat{\boldsymbol{r}}) Y^*_{L'}(\widehat{\boldsymbol{r}}) Y_{L''}(\widehat{\boldsymbol{r}}) \,, \tag{3.6}$$

[1] The spin dependency s of the charge density is at the moment dropped.

the charge density can be expanded as

$$\varrho(\boldsymbol{r}) = \sum_L \varrho_L(r) Y_L^*(\widehat{\boldsymbol{r}}) \,, \tag{3.7}$$

$$\varrho_L(r) = -\frac{1}{2\pi \mathrm{i}} \sum_{L'L''} C_{LL''}^{L'} \big(G_{L'L''}(r) - G_{L''L'}(r)^* \big) \,, \tag{3.8}$$

where

$$G_{LL'}(r) = \int_{\curvearrowright} \mathrm{d}\varepsilon \, G_{LL'}(\varepsilon; r) \,. \tag{3.9}$$

Since the charge density is confined to a WSC, it has to be multiplied with the shape function (2.34)

$$\varrho_L(\boldsymbol{r}) \sigma(\boldsymbol{r}) = \sum_L \overline{\varrho}_L(r) Y_L^*(\widehat{\boldsymbol{r}}) \,, \tag{3.10}$$

$$\overline{\varrho}_L(r) = \sum_{L'L''} C_{L''L}^{L'} \varrho_{L'}(r) \sigma_{L''}(r) \,. \tag{3.11}$$

The charge inside the WSC (with volume Ω) can be calculated from the charge distribution (3.5) [36, section 18.2.2]

$$Q = \int_\Omega \mathrm{d}\boldsymbol{r} \, \varrho(\boldsymbol{r}) \,. \tag{3.12}$$

The latter can be simplified by taking into account the simple relation of the shape function inside the MT sphere with the radius r_{MT}. Only the spherical contribution with $L = (l, m) = (0, 0)$ is nonzero

$$\sigma_L(r) = \sqrt{4\pi} \, \delta_{L,(0,0)} \,, \; r \leq r_{\mathrm{MT}} \,. \tag{3.13}$$

The charge reads finally

$$Q = \sqrt{4\pi} \int_0^{r_{\mathrm{MT}}} \mathrm{d}r \, r^2 \varrho_{(0,0)}(r) + \int_{r_{\mathrm{MT}}}^{r_{\mathrm{BS}}} \mathrm{d}r \, r^2 \sum_L \varrho_L(r) \sigma_L(r) \,. \tag{3.14}$$

The radius r_{BS} corresponds to the so-called bounding sphere (BS), which completely circumscribes the convex polyhedra of the WSC.

The electronic structure of the atoms or ions and their bonding is strongly determined by the behavior of the valence electrons – electrons, which occupy partially filled states. The DOS of such states is usually broadly distributed and close to the Fermi energy E_{F} (see figure 3.1, like, e.g., the $2p$ states of oxygen or the $3d$ states of cobalt in SCO (see figure 5.2). The filled electron shells are in contrast deep below E_{F} and yield a narrow band width. Therefore, most computational methods and in particular the GF method have to consider the valence electrons and the core electrons separately. Other computational methods – so-called all-electron codes like, e.g., the Elk code[2] – treat all electrons on the same footing but need typically a higher number of basis functions and longer computing times.

[2] All-electron full-potential linearized augmented-plane wave code (`http://elk.sourceforge.net/`).

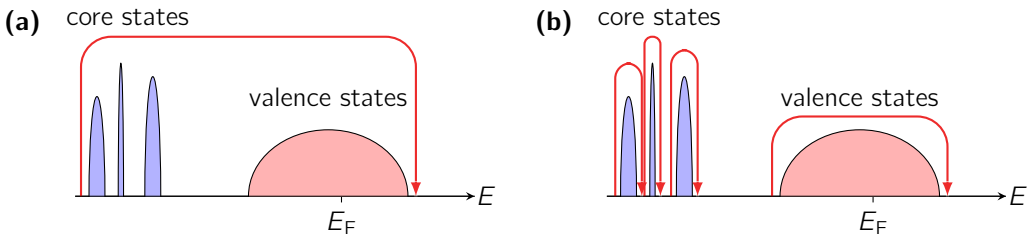

Figure 3.1: Schematic picture of the DOS of the valence and core electronic states as red or blue filled areas, respectively. The red line indicates the integration contour, e.g., in (3.5). Two different possibilities for the integration contour are depicted in (a) and (b).

While the valence electrons are solved in the GF method based on the scattering problem, the core energies are usually obtained from the numerical solution of the Dirac equation with atomic boundary conditions [36, section 22.3]. These atomic boundary conditions mean that the core-wave functions are computed as atomic like states. In HUTSEPOT, the eigenvalues of the core states are calculated with the program of Liberman *et al.* [46].

Often, energetically higher lying core levels occur where the wave functions have a significant extension and should be treated as *semi-core states*. This happens, e.g., for heavier atoms or stronger lattice distortions, when the distance between atoms becomes shorter. These semi-core states can be treated in a similar manner as valence states, either in real or reciprocal space. Depending on the atomic types, the integration contour can be chosen differently, either one contour over all states (see figure 3.1a), so they are treated all on the same footing or individual contours for the core and valence states (see figure 3.1b). The latter allows the description of the valence or the core states with independent approximations, either by the t matrix approximation, in real space or in reciprocal space [1].

In this work, the description of the f states of the rare-earth metals was needed (see chapter 4). The f shells lie very deep below E_F and are strongly localized. Thus, they can be treated as core states, although they are not filled. This *open-core model* was discussed, e.g., by Richter *et al.* [47, 48].

3.1.1. Separation of states with orthogonalization

For many applications and in particular for the description of the crystal field parameter in section 3.3.3, it is mandatory to completely separate the core states from the valence states. However, the energy dependent wave functions in HUTSEPOT do not allow such a separation right from the beginning. If the GF method finds a resonant state in the calculation, the state is considered, independently from the starting assumptions, as either core or valence states.

A possible solution is the orthogonalization of the core wave functions with respect to the valence state wave function like it is done in a modified orthogonalized plane wave (MOPW) method [49]. The orthogonalization of the valence state wave functions $|\phi_L^{\mathrm{v}}(\varepsilon;\boldsymbol{r})\rangle$

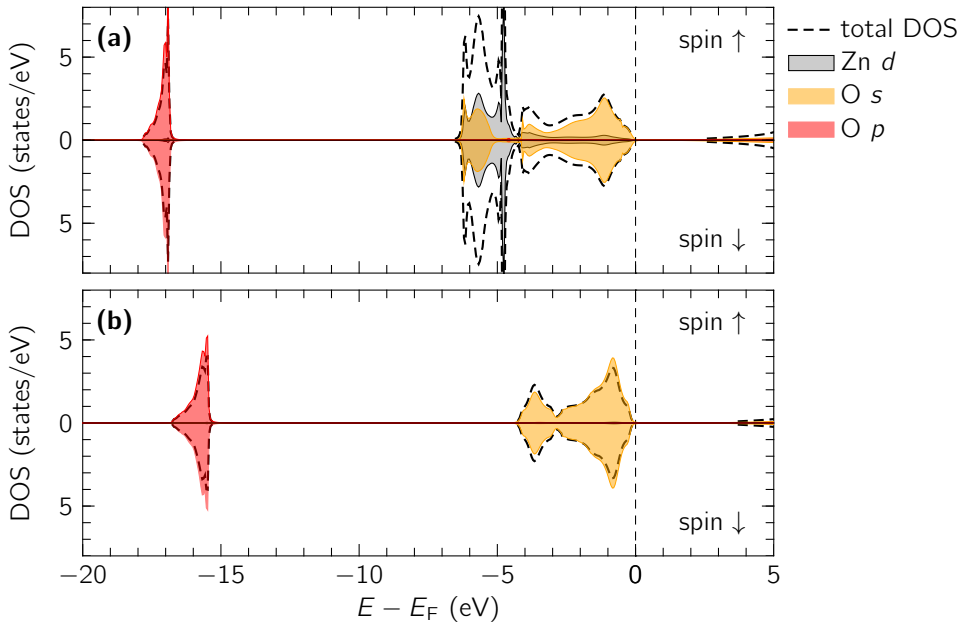

Figure 3.2: Calculated total DOS of ZnO and PDOS of the Zn d, O s and O p states. The results are compared in respect of the orthogonalization of the $3d$ states of Zn: (a) As valence states; (b) As core states with orthogonalization.

with those of the core states $|\phi^{\mathrm{c}}_{L'}(\varepsilon;\boldsymbol{r})\rangle$ is [50, section 2.2]

$$|\phi_L(\varepsilon;\boldsymbol{r})\rangle^{\mathrm{OPW}} = |\phi^{\mathrm{v}}_L(\varepsilon;\boldsymbol{r})\rangle - \sum_{L'} |\phi^{\mathrm{c}}_{L'}(\varepsilon;\boldsymbol{r})\rangle\langle\phi^{\mathrm{c}}_{L'}(\varepsilon;\boldsymbol{r})|\phi^{\mathrm{v}}_L(\varepsilon;\boldsymbol{r})\rangle\,. \tag{3.15}$$

This orthogonalization technique was demonstrated for the transition metal monoxide ZnO, as a brief example. In ZnO, the $3d$ states of Zn are fully occupied though appear in a conventional DOS calculation[3] energetically between the $2s$ and $2p$ states of oxygen (see figure 3.2a). But with the orthogonalized core states, the $3d$ states of Zn can be treated as core states and completely vanish in the resulting DOS, while the shape of the O p states changes drastically (see figure 3.2b).

3.1.2. Local density of states

The real-space integral of the Green's function over the volume of the WSC of site n yields the local density of states (LDOS) for the two spin channels $s = \uparrow$ or $\downarrow$ [36, section 18.2.3]

$$D_s(\varepsilon) = -\frac{1}{\pi}\mathrm{Im}\int_{\Omega} \mathrm{d}\boldsymbol{r}\, G_s(\varepsilon;\boldsymbol{r}+\boldsymbol{R}_n)\,, \tag{3.16}$$

$$= -\frac{1}{\pi}\mathrm{Im}\int_{\mathrm{BS}} \mathrm{d}\boldsymbol{r}\, G_s(\varepsilon;\boldsymbol{r}+\boldsymbol{R}_n)\sigma(\boldsymbol{r})\,. \tag{3.17}$$

[3]The self-consistent and DOS calculations were done with HUTSEPOT for the experimental crystal structure of wurzite type [51, overview in table 1.2]. They were not intended as an extensive description of ZnO but rather as a simple visualization of the effect of orthogonalized core states. So, the calculation settings were not fully optimized.

With the expansions of the diagonal Green's function (3.4) and the shape function (2.35) follows

$$D_s(\varepsilon) = -\frac{1}{\pi}\mathrm{Im}\sum_{LL'L''}\int_0^{r_{\mathrm{BS}}} \mathrm{d}r\, r^2 G_{LL's}(\varepsilon;r) C^{L'}_{LL''}\sigma_{L''}(r)\,, \tag{3.18}$$

$$= -\frac{1}{\pi}\mathrm{Im}\sum_{LL'}\int_0^{r_{\mathrm{BS}}} \mathrm{d}r\, r^2 G_{LL's}(\varepsilon;r)\sigma_{L'L}(r)\,, \tag{3.19}$$

where

$$\sigma_{L'L}(r) = C^{L'}_{LL''}\sigma_{L''}(r)\,. \tag{3.20}$$

If the angular momentum representation of the LDOS (3.17) is defined as a *density matrix* [36]

$$D_{LL's}(\varepsilon) = -\frac{1}{\pi}\mathrm{Im}\sum_{L''}\int_0^{r_{\mathrm{BS}}} \mathrm{d}r\, r^2 G_{LL''s}(\varepsilon;r)\sigma_{L''L'}(r)\,, \tag{3.21}$$

(3.19) can be expressed as a trace

$$D_s(\varepsilon) = \mathrm{Tr}\{D_{LLs}(\varepsilon)\} = \sum_L D_{LLs}(\varepsilon)\,. \tag{3.22}$$

The diagonal elements $D_{Ls}(\varepsilon) \equiv D_{LLs}(\varepsilon)$ can be sorted according to the crystal symmetry into *s*-,*p*-,*d*-like and so forth partial components, the partial density of states (PDOS)

$$D_s(\varepsilon) = \sum_L D_{Ls}(\varepsilon) = \sum_{lm} D_{lms}(\varepsilon) = \sum_l \sum_{m=-l}^{l} D_{lms}(\varepsilon)\,, \tag{3.23}$$

by using crystal symmetry adapted spherical harmonics. The latter are defined via an unitary transformation of the spherical harmonics in such a way that the Green's function in (3.21) becomes diagonal [52]

$$\sum_{L''L'''} U^{\dagger}_{LL''} G^{nn}_{L''L'''}(\varepsilon;r) U^{\dagger}_{L'''L'} = \delta_{LL'}\widetilde{G}^{nn}_{LL'}(\varepsilon;r)\,. \tag{3.24}$$

3.1.3. Band structure and Fermi surface

For a more detailed picture of the electronic structure, the whole band structure can be visualized with the Bloch spectral function (BSF) [28]. The BSF describes the DOS at any $\boldsymbol{k}$ point in the reciprocal space and consists, for an ideal system, of a sum of δ functions, either as a function of the real energy ϵ at a fixed $\boldsymbol{k}$

$$A_{\mathrm{B}}(\epsilon;\boldsymbol{k}) = \sum_\nu \delta(\epsilon - \epsilon_\nu(\boldsymbol{k}))\,, \tag{3.25}$$

$$= -\frac{1}{\pi}\mathrm{Im}\lim_{\eta\to 0^+}\sum_\nu \frac{1}{\epsilon - \epsilon_\nu(\boldsymbol{k}) + \mathrm{i}\eta}\,, \tag{3.26}$$

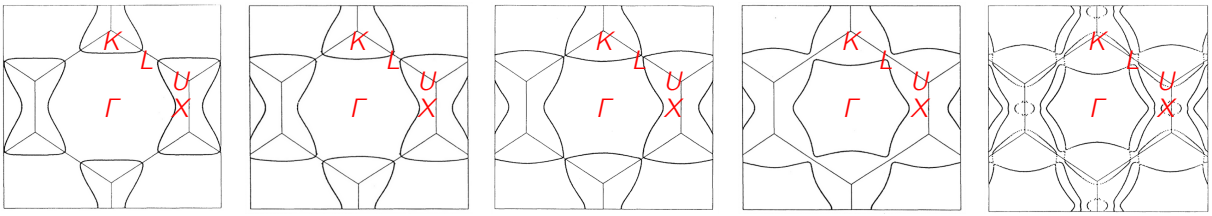

(a) Ag **(b)** $Ag_{0.8}Pd_{0.2}$ **(c)** $Ag_{0.7}Pd_{0.3}$ **(d)** $Ag_{0.6}Pd_{0.4}$ **(e)** Pd

Figure 3.3: Cut through the $\Gamma KLUX$ plane of the Brillouin zone of the Ag_cPd_{1-c} alloy with increasing amount of palladium calculated by Bruno *et al.* [28] with a fully-relativistic KKR-CPA method. The black lines indicate the Fermi surface.

or as a function of the $\boldsymbol{k}$ point at fixed ϵ

$$A_{\mathrm{B}}(\epsilon;\boldsymbol{k}) = \sum_{\nu} \delta(k_{\zeta} - k_{\zeta\nu}(\epsilon))\,, \tag{3.27}$$

$$= -\frac{1}{\pi}\mathrm{Im}\lim_{\xi\to 0^+}\sum_{\nu}\frac{C_{\zeta\nu}}{k_{\zeta} - k_{\zeta\nu}(\epsilon) + \mathrm{i}\xi}\,, \tag{3.28}$$

along a direction labeled ζ [28]. The BSF can be calculated directly from the imaginary part of the Fourier transformed Green's function $G(\varepsilon;\boldsymbol{k})$ [53]

$$A_{\mathrm{B}}(\epsilon;\boldsymbol{k}) = -\frac{1}{\pi}\mathrm{Im}\,G(\varepsilon;\boldsymbol{k})\,. \tag{3.29}$$

Peaks in (3.29) define occupied electronic states according to (3.26) or (3.28) and, therewith, the band structure. An integral over the $\boldsymbol{k}$ points yields again the DOS. If the energy is fixed to the Fermi energy $\epsilon = E_{\mathrm{F}}$, the discontinuity of the BSF defines the Fermi surface. This definition of the Fermi surface holds true also in the case of an averaged Green's function [28, 53]. The concept of the effective medium description within the coherent potential approximation is described in more detail in section 3.4.2. For example, the Fermi surface for varying chemical composition of the alloy Ag_cPd_{1-c} [28] is presented in figures 3.3a to 3.3e. The palladium content in pure silver is gradually increased. Thereby, electrons from the Ag d states are removed and the connectivity across the Brillouin zone can vary – so-called electronic topological transitions (ETT) or Lifshitz transitions.

3.1.4. Electronic correlation effects

The conventional exchange-correlation functionals (LDA or GGA) are typically sufficient to describe material perperties of metallic systems (see section 6.2.1) but they often underestimate the strongly localized character of, e.g., d states of the transition metal atoms or f states of the rare earth metal atoms. The repulsion between different orbitals due to electron hopping has to be considered. In such strong localized systems, the character of the conductance might be wrongly described. The numerical calculations might obtain a wrong band gap, no band gap at all, or a wrong energy-dependent splitting of the d

states. The latter can lead, e.g., to an overestimation of the critical temperature T_t for the magnetic phase transition, as obtained in chapter 5 in the calculations of T_t for SCO and SFMO within the GGA (see figures 5.5 or 5.12).

For the description of such localized states, the self-interaction correction (SIC) scheme proofed to be very useful [52]. It is also implemented in HUTSEPOT. Within the SIC, the double-counting term inside the LDSA can be corrected for a chosen state. As previously shown for the LDOS density matrix (3.21), also the charge density (3.5) can be decomposed into the different angular momentum contributions by using the unitary transformation (3.24). The charge density of a single electron at site n, the angular momentum L, and the spin s is

$$\varrho_{nLs}(\boldsymbol{r}) = -\frac{1}{\pi}\mathrm{Im}\int_{\curvearrowright E_\mathrm{B}}^{E_\mathrm{F}} \mathrm{d}\varepsilon\, G^{nn}_{LLs}(\varepsilon;\boldsymbol{r}+\boldsymbol{R}_n)\,, \tag{3.30}$$

where the integral is calculated along a contour from the bottom of the band E_B up to the Fermi energy E_F [52].

The effective potential within the SIC and the LDA is then obtained by subtracting the Hartree potential V_H and the exchange-correlation potential $V_\mathrm{xc}^\mathrm{LDA}$ from the original effective potential (2.13)

$$V^{\text{SIC-LDA}}_{\text{eff},nLs}(\boldsymbol{r}) = V^{\text{LDA}}_{\text{eff},s}(\boldsymbol{r}) - V_\mathrm{H}\left[\varrho_{nLs}\right](\boldsymbol{r}) - V^{\text{LDA}}_{\text{xc}}\left[\varrho_{nLs},0\right](\boldsymbol{r})\,. \tag{3.31}$$

The two latter terms in (3.31), V_H and $V_\mathrm{xc}^\mathrm{LDA}$, are calculated for the charge density (3.30). The exchange-correlation potential depends on the chosen spin channel. The SIC potential (3.31) is used for the computation of a SIC single scattering solution $t^{n,\text{SIC-LDA}}_{Ls}$ while the normal single-site scattering t matrix t^n_{Ls} is calculated from the original effective potential $V^\mathrm{LDA}_{\mathrm{eff},s}(\boldsymbol{r})$. For each corrected state $\widetilde{L} = (\widetilde{l},\widetilde{m})$, $\widetilde{s}$, the $\widetilde{L}$th matrix element of the original t matrix is substituted by the corresponding element of the SIC t matrix

$$\widetilde{t}^n_{Ls} = t^n_{Ls}(1-\delta_{L\widetilde{L}}\delta_{s\widetilde{s}}) + t^{n,\text{SIC-LDA}}_{\widetilde{L}\widetilde{s}}\delta_{L\widetilde{L}}\delta_{s\widetilde{s}}\,. \tag{3.32}$$

Finally, the new t matrix in (3.32) determines a new SIC-LDA charge density for (3.31). This procedure for the calculation of $\varrho_{nLs}(\boldsymbol{r})$ is repeated till self-consistency.

The ground state properties obtained within the SIC agree well with measurements for, e.g., transition metal monoxides [54] or rare earth-atoms like cerium [52]. Nevertheless, the localization of the corrected states tends to be overestimated, e.g., the calculation of the DOS within the SIC yields for bulk SFMO a half-metallic band-gap, but it is far too large when compared with experimental observations [55]. Therefore, the electron correlation effects were also taken into account with the Hubbard model [56]. The Hubbard Hamiltonian $\widehat{H}_U$ allows for the orbital degeneracy of the $3d$ orbitals in the form of [57]

$$\widehat{H}_U = \frac{U}{2}\sum_{m,m',s}\widehat{n}_{m,s}\widehat{n}_{m',-s} + \frac{U-J}{2}\sum_{m\neq m',s}\widehat{n}_{m,s}\widehat{n}_{m',s}\,. \tag{3.33}$$

The first term in (3.33) describes the on-site repulsion, where $\widehat{n}_{m,s} = \widehat{a}^\dagger_s\widehat{a}_s$ is the number of electrons operator with spin s and the projection of the orbital momentum m ($m, m' =$

$-2, -1, \ldots, 2$ for d electrons). Its expectation value is the occupation number n_{ms}. The parameters U and J represent the spherically averaged matrix elements of the screened Coulomb electron-electron interaction.

However, the expectation value of the Hamiltonian (3.33) reads differently for a non-integer or an integer number of d electrons. The latter represents the correct form of the density functional for (3.33). The difference between the two cases is expressed by the LDA+U functional [58]

$$E_{\mathrm{LDA}+U} = E_{\mathrm{LDA}} + \frac{U-J}{2} \sum_s \left(n_{ms} - n_{ms}^2\right) . \tag{3.34}$$

For the sake of simplicity, the difference $U - J$ is defined as U_{eff} in the following context.

If the charge density (3.30) is expressed as a density matrix

$$\varrho_{nLs,L's'}(\boldsymbol{r}) = -\frac{1}{\pi} \mathrm{Im} \int_{\curvearrowright E_{\mathrm{B}}}^{E_{\mathrm{F}}} \mathrm{d}\varepsilon \, G_{LL'ss'}(\varepsilon; \boldsymbol{r} + \boldsymbol{R}_n) , \tag{3.35}$$

and $\varrho_{mm's}(\boldsymbol{r}) = \varrho_{nLs,L's}(\boldsymbol{r})$ is the density matrix of the d electrons ($l = 2$), equation (3.34) can be rewritten as [58]

$$E_{\mathrm{LDA}+U} = E_{\mathrm{LDA}} + \frac{U_{\mathrm{eff}}}{2} \sum_s \left[\sum_m \varrho_{mm}^s - \sum_{mm'} \varrho_{mm'}^s \varrho_{m'm}^s) \right] . \tag{3.36}$$

Its derivative yields the matrix elements of the one-electron potential

$$V_{mm's} \equiv \frac{\delta E_{\mathrm{LDA}+U}}{\delta \varrho_{mm's}} = \frac{\delta E_{\mathrm{LDA}}}{\delta \varrho_{mm's}} + U_{\mathrm{eff}} \left[\frac{1}{2} \delta_{mm'} - \varrho_{mm's} \right] . \tag{3.37}$$

The total energy is then given by

$$E_{\mathrm{LDA}+U} = E_{\mathrm{LDA}} + \frac{U_{\mathrm{eff}}}{2} \sum_{m,m',s} \varrho_{mm's} \varrho_{mm's} . \tag{3.38}$$

Although (3.38) is formulated in terms of the LDA exchange-correlation functional, the GGA exchange-correlation functional can be applied in exactly the same way.

3.2. Calculation of equilibrium properties

The equilibrium ground state or better to say the thermodynamic state of a system is determined by the pressure P, the temperature T and the specific volume V, which are linked by an equation of states (EOS) [59]. For solids, the influence of the temperature is small in respect of its effect on the equilibrium state of a gas and it is, therefore, sufficient to consider only the isothermal equation of states. In the numerical calculations, a set of total energies at different volumes is calculated and fitted to an EOS. The fitting parameters are the thermodynamic quantities in the equilibrium ground state.

3.2.1. Murnaghan equation of states

A simple EOS follows from the definition of the bulk modulus as the volume derivative of the pressure,

$$B(V) = -V\frac{\partial P}{\partial V}\,, \tag{3.39}$$

shows by itself a negligible pressure dependence [59, 60]

$$\frac{\partial B}{\partial P} \approx B_0' = \left.\frac{\partial B}{\partial P}\right|_{V=V_0,P=0}\,. \tag{3.40}$$

Thereby, V_0 is the equilibrium volume, B_0 equals $B(V_0, P = 0)$ and B_0' is the so-called Grüneisen constant. With (3.39), it follows

$$B_0' = -\frac{V}{B}\frac{\partial B}{\partial V}\,. \tag{3.41}$$

Integrating over the volume from V_0 to V yields [60]

$$B(V) = B_0\left(\frac{V_0}{V}\right)^{B_0'}\,. \tag{3.42}$$

A second integration gives the Murnaghan EOS [61, 62]

$$P(V) = \frac{B_0}{B_0'}\left[\left(\frac{V_0}{V}\right)^{B_0'} - 1\right]\,. \tag{3.43}$$

3.2.2. Birch-Murnaghan equation of states

The concept of Murnaghan was further developed by Birch leading to the second- and third-order Birch-Murnaghan equation of states [59, 63, 64]. The latter is more flexible and often used in literature. The pressure is written as

$$P(V) = \frac{3}{2}B_0\left[\left(\frac{V_0}{V}\right)^{7/3} - \left(\frac{V_0}{V}\right)^{5/3}\right]\left\{1 + \frac{3}{4}(B_0' - 4)\left[\left(\frac{V_0}{V}\right)^{2/3} - 1\right]\right\}\,. \tag{3.44}$$

For a brief overview of its derivation, a closer look to the thermodynamic potentials is necessary. The mechanical term $p\mathrm{d}V$ of the Helmholtz free energy F contains information about the stress and the infinitesimal strain [65]

$$\mathrm{d}F = V\sum_{lm}\sigma_{lm}\mathrm{d}\varepsilon_{lm} - S\mathrm{d}T + \sum_i \mu_i \mathrm{d}N_i\,, \tag{3.45}$$

with the stress tensor σ_{lm} and the strain tensor ε_{lm}. The last two terms in (3.45) can be neglected in an *ab initio* calculation for a closed system at 0 K. When the remaining term is integrated and the elastic tensor $\sigma_{lm} = c_{lmik}\varepsilon_{ik}$ is inserted, it follows

$$F = V\frac{1}{2}c_{lmik}\varepsilon_{ik}\varepsilon_{lm}\,. \tag{3.46}$$

The strain tensor is determined by the components of a displacement vector $\boldsymbol{u}$ or by the coordinates of the strained $\boldsymbol{r}'$ and unstrained $\boldsymbol{r}$ states. Since only the hydrostatic pressure is considered, the variation for all three directions in space is the same [59] and the strain tensor becomes

$$\varepsilon_{ik} = \varepsilon\delta_{ik}\,. \tag{3.47}$$

The dilatation ε in (3.47) is negative for positive pressures. Thus, the compression $f = -\varepsilon$ can be introduced. The free energy can now be expanded in terms of this compression f

$$F = a(T)f^2 + b(T)f^3 + c(T)f^4 + \dots\,. \tag{3.48}$$

For the third-order Birch-Murnaghan EOS, the free energy (3.48) is expanded up to the third order

$$F \approx a(T)f^2 + b(T)f^3\,. \tag{3.49}$$

The derivative of F is given by

$$\left(\frac{\partial F}{\partial f}\right)_T = 2af + 3bf^2 = 2af\left(1 + \frac{3bf}{2a}\right). \tag{3.50}$$

Since the pressure is the volume derivative of the free energy, P becomes

$$P(V) = -\left(\frac{\partial F}{\partial V}\right)_T = -\left(\frac{\partial F}{\partial f}\right)_T \frac{\mathrm{d}f}{\mathrm{d}V}\,, \tag{3.51}$$

$$= 3B_0 f(v)(1 + 2f(V))^{5/2}\left(1 + \frac{3bf(V)}{2a}\right). \tag{3.52}$$

Therein, the parameters a and b are determined from the conditions that the two quantities $B(V)$ and $B'(V)$ turn into the equilibrium values B_0 or B_0' at zero pressure (f becomes zero). Both quantities can be expressed via (3.39) or (3.40) in terms of $P(V)$ or $f(V)$, The two equations form a system of equations with the solution of

$$a = \frac{3}{2}B_0\,, \tag{3.53}$$

$$b = \frac{3}{2}B_0(B_0' - 4)\,. \tag{3.54}$$

Finally, plugging the function $f(V)$ [59]

$$f(V) = \frac{1}{2}\left[\left(\frac{V_0}{V}\right)^{2/3} - 1\right], \tag{3.55}$$

and the parameter a and b into (3.52) leads to the third-order Birch-Murnaghan EOS (3.44). Additional integration yields the free energy or, for $T = 0$, the total energy

$$E(V) = E_0 + \frac{9}{16}B_0V_0 \times$$
$$\times \left\{\left[\left(\frac{V_0}{V}\right)^{2/3} - 1\right]^3 B_0' - \left[\left(\frac{V_0}{V}\right)^{2/3} - 1\right]^2 \left[4\left(\frac{V_0}{V}\right)^{2/3} - 6\right]\right\}. \tag{3.56}$$

In (3.56) only the quantities B_0, V_0, and E_0 have a unit and are given in GPa, Å^3, and Ryd, respectively.[4]

[4]The conversion factor into energy units is 1 GPa Å^3 = 10^{-21} J or 1 GPa Å^3 = 0.000 458 737 Ryd.

3.2.3. Other equation of states

There are several other concepts for an EOS, e.g., the Vinet EOS [66, 67] or the Morse EOS [68]. The total energy in terms of the Morse EOS is given by

$$E(w) = a + be^{-\lambda w} + ce^{-2\lambda w} \,. \tag{3.57}$$

The parameter w represents the averaged Wigner-Seitz radius, while λ, a, b, and c are the four independent Morse parameters.

3.2.4. Deviation from the Vegard's law

If the chemical composition in a solid solution is changed continuously, all equilibrium properties vary in first order linearly with the concentration c. This is the essence of the Vegard's law [25]. However, such linear behavior is more the exception and there is usually a characteristic deviation from this linear behavior. Following [22], the anomalies of a general equilibrium observable A are defined as

$$\Delta A(c) = A(c) - \overline{A}(c) \tag{3.58}$$

$$\overline{A}(c) = A(0) + c\,[A(1) - A(0)] \,, \tag{3.59}$$

where $A(0)$ and $A(1)$ are the corresponding values for the pure constituents (for the Ag_cPd_{1-c} alloy, they are Pd and Ag, respectively [E12]).

3.3. Magnetic properties

Another ground state material property originates from permanent magnetic dipole moments $\boldsymbol{m}$. Such magnetic moments result from not fully filled electron shells (open shells) [69], which are present, e.g., in transition metal atoms (d shells) or rare earth metal atoms (f shells). The corresponding macroscopic quantity, the total magnetic moment per volume unit, is the magnetization of the material [70]

$$\boldsymbol{M} = \boldsymbol{m}\frac{N}{V} \,. \tag{3.60}$$

Together with an external magnetic field $\boldsymbol{H}$, the magnetic induction $\boldsymbol{B}$ (also named magnetic field)[5] inside the material is

$$\boldsymbol{B} = \mu_0(\boldsymbol{H} + \boldsymbol{M}) \,, \tag{3.61}$$

with the magnetic permeability of free space μ_0. The susceptibility χ_T describes the linear response of the magnetization to an external magnetic field $\boldsymbol{H}$

$$\boldsymbol{M} = \chi_T \boldsymbol{H} \,. \tag{3.62}$$

[5]This technical term follows the common usage in literature. The letter determines which physical quantity is meant.

Therein, χ_T is a negative constant for diamagnetic materials, practically zero for nearly free electrons (Pauli paramagnetism) and positive and temperature dependent for localized moments (Langevin paramagnetism) [70].

When the temperature falls below a critical temperature T_t, the moments might show spontaneously a collective magnetic order. This order can be parallel (ferromagnetic – FM) with the Curie temperature T_C, antiparallel (antiferromagnetic – AFM) with the Néel temperature T_N or more complex, e.g., antiparallel with a different size of the magnetic moments (ferrimagnetic – FiM), helically ordered or forming a spin glass structure. The collective magnetism can not be attributed to a simple dipole-dipole interaction but to an only quantum mechanically explainable *magnetic exchange interaction* between the permanent magnetic moments [69]. Although this technical term, magnetic exchange interaction, conveys a magnetic character of this interaction, its nature is mainly electrostatic [71].

3.3.1. Heisenberg model

The classical Heisenberg model offers a reasonable description for localized moments $\boldsymbol{m} = (m_x, m_y, m_z)$ not only in insulators but also in metallic systems [69, section 8]. It can be expressed in a general form

$$\widehat{H}_{\mathrm{H}} = -\sum_{i \neq j} J_{ij} \boldsymbol{m}_i \cdot \boldsymbol{m}_j + \mu_{\mathrm{B}} \sum_i \boldsymbol{m}_i \cdot \boldsymbol{B} + \widehat{H}_{\mathrm{MAE}} \,. \tag{3.63}$$

The first sum in (3.63) runs in general over all magnetic sites i and j with the magnetic moments $\boldsymbol{m}_i$ and $\boldsymbol{m}_j$, which are coupled via the magnetic exchange interactions J_{ij}. The second term – Zeeman term – appears when an external homogeneous magnetic field $\boldsymbol{B}$ is applied. The last contribution in (3.63) represents the magnetic anisotropy energy (MAE), which is described in more detail in section 3.3.3.

The nature of the magnetic moment in the general Heisenberg Hamiltonian (3.63) is regarded by inclusion of the Landé factor g. If the magnetic moments result purely from the electron spin, then $g = g_S$ is ≈ 2. Otherwise, e.g., for the rare earth metals, the total angular momentum $J = L + S$ is taken into account by

$$g_J = 1 + \frac{J(J+1) - L(L+1) + S(S+1)}{2J(J+1)} \,, \tag{3.64}$$

where L and S are the orbital and spin angular momentum quantum numbers, respectively.

3.3.2. Magnetic force theorem

The magnetic coupling constants in (3.63) can be calculated from *ab initio* via the magnetic force theorem [72]. It is derived on the basis of the Heisenberg Hamiltonian (3.63) and the localized magnetic moments. The z-direction is defined as the direction all moments align in the case of ferromagnetic order. When a single spin moment at the origin is rotated about a small angle θ, the energy variation is given by [72]

$$\delta E_0 = 2 \sum_j J_{0j} (1 - \cos\theta) \simeq J_0 \theta^2 \text{ with } J_0 = \sum_j J_{0j} \,. \tag{3.65}$$

If two spin moments at site i and j are rotated towards opposite angles $\pm\theta/2$, the energy variation is given by

$$\delta E'_{ij} = \delta E_{ij} - \delta E_i - \delta E_j = J_{ij}(1-\cos\theta) \simeq \frac{1}{2} J_{ij}\theta^2 \,. \tag{3.66}$$

An equation to calculate these energy variations from first-principles follows from the local force theorem [73]. In first order, the energy variation can be written as

$$\delta E = \int^{E_\mathrm{F}} \mathrm{d}\varepsilon\, \varepsilon \delta D_s(\varepsilon) = E_\mathrm{F}\, \delta z - \int^{E_\mathrm{F}} \mathrm{d}\varepsilon\, \delta N(\varepsilon) = -\int^{E_\mathrm{F}} \mathrm{d}\varepsilon\, \delta N(\varepsilon)\,, \tag{3.67}$$

with the density of states $D_s(\varepsilon) = \mathrm{d}N/\mathrm{d}\varepsilon$. The variation of the number of electrons δz is zero, since the number of electrons remains constant for a magnetic excitation.

The variation $\delta N(\varepsilon) = N'(\varepsilon) - N(\varepsilon)$ in (3.67) is derived by starting from the Lloyd equation [74]

$$N(\varepsilon) = N_0(\varepsilon) + \frac{1}{\pi}\mathrm{Im}\mathrm{Tr}\ln \underline{\tau}(\varepsilon)\,, \tag{3.68}$$

and defining the perturbed scattering path operator by [72]

$$\underline{\tau}' = \underline{\tau}(\underline{1} + \delta\underline{t}^{-1} \times \underline{\tau})\,, \tag{3.69}$$

where $\underline{1}$ represents the two-dimensional unit matrix and $\times$ indicates a matrix product. The energy variation (3.67) becomes

$$\delta E = \frac{1}{\pi}\mathrm{Im}\int^{E_\mathrm{F}} \mathrm{d}\varepsilon\, \mathrm{Tr}\ln(\underline{1} + \delta\underline{t}^{-1} \times \underline{\tau})\,. \tag{3.70}$$

The variation of the scattering t matrix is found from its spinor structure at the site i

$$\underline{t}^i = {}^1\!/_2(\underline{t}^i_\uparrow + \underline{t}^i_\downarrow)\underline{1} + {}^1\!/_2(\underline{t}^i_\uparrow - \underline{t}^i_\downarrow)(\boldsymbol{e}_i \cdot \underline{\boldsymbol{\sigma}})\,, \tag{3.71}$$

with the Pauli matrices $\underline{\boldsymbol{\sigma}}$. Its variation is

$$(\delta\underline{t}^i)^{-1} = {}^1\!/_2 \underbrace{\left((\underline{t}^i_\uparrow)^{-1} - (\underline{t}^i_\downarrow)^{-1}\right)}_{=:\underline{\Delta}_i}(\delta\boldsymbol{e}_i \cdot \underline{\boldsymbol{\sigma}})\,. \tag{3.72}$$

To estimate the effective interaction of the moment at the origin ($i = 0$) with the rest of the system, a rotation around the y-axis is considered

$$\delta\boldsymbol{e}_0 = (\sin\theta, 0, \cos\theta - 1)\,. \tag{3.73}$$

Under consideration of the scalar product between the vector $\delta\boldsymbol{e}_0$ and the Pauli matrices, (3.72) yields

$$(\delta\underline{t}^i)^{-1} = {}^1\!/_2\delta_{i0}\underline{\Delta}_i \begin{pmatrix} \cos\theta - 1 & \sin\theta \\ \sin\theta & 1 - \cos\theta \end{pmatrix}\,. \tag{3.74}$$

On the other hand, at the origin, only the matrix elements $\underline{\tau}^{00}$ are relevant for (3.70) and it becomes

$$\underline{\tau}^{00} = \begin{pmatrix} \underline{\tau}_{\uparrow}^{00} & 0 \\ 0 & \underline{\tau}_{\downarrow}^{00} \end{pmatrix}, \tag{3.75}$$

in the ferromagnetic ground state. Finally, the trace in (3.70) over the 2×2 matrix can be written as a determinant

$$\mathrm{Tr} \ln \left(\underline{1} + (\delta \underline{t}^0)^{-1} \times \underline{\tau}^{00} \right) = \mathrm{Tr}_L \ln \det \left(\underline{1} + (\delta \underline{t}^0)^{-1} \times \underline{\tau}^{00} \right), \tag{3.76}$$

while the trace over the angular momentum indices remains and is expressed as Tr_L. Thus, the energy variation is given by

$$\delta E_0 = \frac{1}{\pi} \int^{E_\mathrm{F}} \mathrm{d}\varepsilon \, \mathrm{Im} \mathrm{Tr}_L \ln \left\{ 1 - {}^1\!/_2 [\underline{\Delta}_0 (\underline{\tau}_{\uparrow}^{00} - \underline{\tau}_{\downarrow}^{00}) + \underline{\Delta}_0 \underline{\tau}_{\uparrow}^{00} \underline{\Delta}_0 \underline{\tau}_{\downarrow}^{00}] (1 - \cos\theta) \right\}, \tag{3.77}$$

Since the angle θ is small, the cosine in (3.77) is expanded ($1 - \cos\theta \approx \theta^2/2$) and, then, the natural logarithm is expanded ($\ln(1+x) \approx x$). From the comparison with (3.65), it follows

$$J_0 = -\frac{1}{4\pi} \int^{E_\mathrm{F}} \mathrm{d}\varepsilon \, \mathrm{Im} \mathrm{Tr}_L \left\{ \underline{\Delta}_0 (\underline{\tau}_{\uparrow}^{00} - \underline{\tau}_{\downarrow}^{00}) + \underline{\Delta}_0 \underline{\tau}_{\uparrow}^{00} \underline{\Delta}_0 \underline{\tau}_{\downarrow}^{00} \right\}. \tag{3.78}$$

For the general magnetic exchange interactions between site i and site j, each moment is rotated by $\theta/2$

$$\delta \boldsymbol{e}_i = (+\sin\frac{\theta}{2}, 0, \cos\frac{\theta}{2} - 1), \tag{3.79}$$

$$\delta \boldsymbol{e}_j = (-\sin\frac{\theta}{2}, 0, \cos\frac{\theta}{2} - 1), \tag{3.80}$$

$$\delta \boldsymbol{e}_0 = (0, 0, 1). \tag{3.81}$$

The matrices $\underline{1} + \delta \underline{t}^{-1} \times \underline{\tau}$ in (3.70) become more complicated and the full derivation is waived at this point. However, by taking into account the terms up to the second order in θ, Liechtenstein *et al.* found [72]

$$J_{ij} = \frac{1}{4\pi} \int^{E_\mathrm{F}} \mathrm{d}\varepsilon \, \mathrm{Im} \mathrm{Tr}_L \left(\underline{\Delta}_i \underline{\tau}_{\uparrow}^{ij} \underline{\Delta}_j \underline{\tau}_{\downarrow}^{ji} \right). \tag{3.82}$$

3.3.3. Magnetic anisotropy

The magnetic anisotropy determines the intrinsic orientation of the magnetic moments in an ordered state. For example, the magnetization of a ferromagnetic state is isotropic and might orient in any direction, if the last two terms in (3.63) are zero ($\boldsymbol{B} = 0$ and $\widehat{H}_\mathrm{MAE} = 0$). In a magnetic field $|\boldsymbol{B}| \neq 0$, the magnetic moments are aligned parallel along the field direction. This orientation mechanism might compete with the given direction of the magnetic anisotropy, which has two contributions: the dipole-dipole interaction, so-called Dzyaloshinskii-Moriya interaction (DMI), and the coupling of the electron orbits to

the crystalline electric field (CF) [69]. The latter is often referred as the magnetocrystalline anisotropy. The energy scale of both contributions is small in respect of the energy scale of the magnetic exchange interactions. Hence, they are neglected in all bulk calculations throughout this thesis.

Nevertheless, the magnetocrystalline anisotropy becomes crucial for surfaces and clusters of atoms, since the classical Heisenberg model (3.63) yields no spontaneous magnetization in two-dimensional systems without the MAE (see Mermin-Wagner theorem [69]). Thus, the term $\widehat{H}_{\mathrm{MAE}}$ was in particular considered in this thesis in the context of a single holmium atom at a platinum surface (see chapter 4). The most simple anisotropy contribution appears for an uniaxial ferromagnet [69]

$$\widehat{H}_{\mathrm{MAE}} = \widehat{H}_{\mathrm{uni}} = -Km_z^2\,, \tag{3.83}$$

The single anisotropy parameter K in (3.83) is often sufficient to describe, e.g., resonance experiments. It defines in the considered material an easy and a hard magnetization axis, either parallel or perpendicular to the z-direction and can be calculated directly within the GF method [75]. For an atomic cluster or ultra thin film, the easy axis is typically oriented out-of-plane.

However, (3.83) could not explain the experimental findings for the Holmium on Pt(111) system [E11]. The complex symmetry of the threefold (111) surface made it necessary to use a full crystal field Hamiltonian

$$\widehat{H}_{\mathrm{MAE}} = \widehat{H}_{\mathrm{CF}} = \sum_{n=0}^{\infty}\sum_{m=0}^{n} B_n^m \widehat{O}_n^m\,, \tag{3.84}$$

with the anisotropy constants or crystal field parameters B_n^m (CFP). The Hamiltonian (3.84) acts on the total angular momentum states $|JM\rangle$. Hence, the quantities in (3.63) have to expressed as operators as well.

The underlying crystal symmetry is included within the crystal field or Stevens' operators $\widehat{O}_n^m$. The $\widehat{O}_n^m$ are polynomials of the order n in the operator $\widehat{J}_z$ and of the order m in the ladder operators $\widehat{J}_+$ and $\widehat{J}_-$. The latter raise or lower M by one, respectively. Due to symmetry reasons the operators appear only in even powers of $n \leq 2l$. Terms with $m = 0$ contain only powers of $\widehat{J}_z$. Thus, the first nonzero term in (3.84) is $n = 2$ and $m = 0$ with [76]

$$\widehat{O}_2^0 = 3\widehat{J}_z^2 - J(J+1)\,. \tag{3.85}$$

which is proportional to the uniaxial anisotropy (3.83) with $B_2^0 \propto K$.

The first-principle calculation of the anisotropy parameters

In general, the parameter B_n^m of the crystal field Hamiltonian (3.84) for a rare earth metal atom can be calculated from first-principles starting from the energy of the interaction of the $4f$ electrons with all other charges [77]

$$E_{4f} = \int\int \mathrm{d}\boldsymbol{R}\,\mathrm{d}\boldsymbol{r}\,\frac{\varrho(\boldsymbol{R})\varrho_{4f}(\boldsymbol{r})}{|\boldsymbol{R}-\boldsymbol{r}|}\,. \tag{3.86}$$

Since the $4f$ states were treated as core states, their charge density $\varrho_{4f}(\boldsymbol{r})$ was separated from all other charges of the crystal $\varrho(\boldsymbol{R})$ (nuclei, core electrons and valence electrons) via the orthogonalization described in section 3.1.1.

In a first order perturbation theory, an unperturbed $4f$ state from the ground state multiplet of a free rare earth metal atom $|R_{4f}; JM\rangle$ with n_{4f} unfilled f shells is disturbed by a small electrostatic potential $V(\boldsymbol{r})$ and leads to the expectation value of the interaction energy [78]

$$E_{4f}(M) = \langle R_{4f}; JM| \sum_{i}^{n_{4f}} V_{\text{asph}}(\boldsymbol{r}_i) |R_{4f}; JM\rangle \,. \tag{3.87}$$

The non-spherical potential V_{asph} includes all charges in the crystal $\varrho(\boldsymbol{R})$ without the non-spherical $4f$ charge of the considered rare earth atom. This potential is expanded in terms of the real spherical harmonics[6] $\mathcal{Y}_L(\widehat{\boldsymbol{r}})$, centered at the rare earth atoms ($\forall\ l > 0$ and $L = (l, m)$) with the unit vector $\widehat{\boldsymbol{r}}$

$$V(\boldsymbol{r}) = \sum_{L} V_L(r) \mathcal{Y}_L(\widehat{\boldsymbol{r}}) \,. \tag{3.88}$$

If every unfilled electron shell is assumed to have the same radial wave function R_{4f}, (3.87) can be separated into two expectation values, one for the radial and one for the spherical contributions, respectively,

$$E_{4f}(M) = \sum_{L} \langle R_{4f}|V_L(r)|R_{4f}\rangle \langle JM| \sum_{i}^{n_{4f}} \mathcal{Y}_L(\widehat{\boldsymbol{r}}) |JM\rangle \,. \tag{3.89}$$

The first term represents an integral over the radial components. In the second expectation value, the Steven operator equivalents [76, 79] substitute the sum

$$\sum_{i}^{n_{4f}} \mathcal{Y}_L(x_i, y_i, z_i) \rightarrow C_L \theta_l(J) \widehat{O}_l^m(\widehat{J}_x, \widehat{J}_y, \widehat{J}_z) \,, \tag{3.90}$$

where the factors $\theta_l(J)$ for the rare earth metal atoms R^{3+} are tabulated in [76, 79]. The numerical prefactors C_L of the real spherical harmonics appear explicitly because the Steven operator equivalents were formerly written only for the x, y and z depend polynomials of $\mathcal{Y}_L(\widehat{\boldsymbol{r}})$. Thus, (3.89) reads

$$E_{4f}(M) = \sum_{L} \int \mathrm{d}r\, r^2 R_{4f}^2(r) V_L(r)\ C_L \theta_l(J) \langle JM|\widehat{O}_l^m(\widehat{J}_x, \widehat{J}_y, \widehat{J}_z)|JM\rangle \,. \tag{3.91}$$

A comparison of (3.91) with the expectation value $\langle JM|\widehat{H}_{\text{CF}}|JM\rangle$ of the crystal field Hamiltonian (3.84) shows that the radial part of the $4f$ charge density (the square of the wave function corresponds to the charge density) determines the CFP [77, 79]

$$B_l^m = \theta_l(J) A_l^m \langle r^l \rangle = \theta_l(J) C_L \int \mathrm{d}r\, r^2 \varrho_{4f}(r) V_L(r) \,. \tag{3.92}$$

[6] Please note the use of real spherical harmonics, in contrast to the complex spherical harmonics $Y_L(\widehat{\boldsymbol{r}})$ used for the earlier expansions of charge density or Green's function. Although, the expansions in section 3.1 can be formulated within the real spherical harmonics as well.

To evaluate (3.92), the denominator of the potential $V(\boldsymbol{r}) = \int \mathrm{d}\boldsymbol{r}' \, \frac{\varrho(\boldsymbol{r}')}{|\boldsymbol{r}-\boldsymbol{r}'|}$ is expanded

$$V_L(r) = \frac{4\pi}{2l+1} \int \mathrm{d}\boldsymbol{r}' \, \varrho(\boldsymbol{r}') \mathcal{Y}_L(\widehat{\boldsymbol{r}}') \frac{r_<^l}{r_>^{l+1}} \,, \tag{3.93}$$

with $r_< = \min(r, r')$ and $r_> = \max(r, r')$. Finally, the CFP will take the form

$$\left[A_l^m \langle r^l \rangle\right] = \frac{4\pi}{2l+1} C_L \int^{\infty} \mathrm{d}\boldsymbol{r}' \, \varrho(\boldsymbol{r}') \mathcal{Y}_L(\widehat{\boldsymbol{r}}') \int \mathrm{d}r \, r^2 \varrho_{4f}(r) \frac{r_<^l}{r_>^{l+1}} \,. \tag{3.94}$$

3.3.4. Magnetic transition temperature

The Heisenberg model allows to determine the magnetic transition temperature T_t. The most simple approximation accounts for the collective interaction of all other magnetic moments with the one at the origin as an additional molecular magnetic field. This mean-field approximation (MFA) can be obtained from the effective coupling constant J_0 in (3.78) but it often overestimates T_t with respect to the experimental measurements.

A more reliable method to obtain the critical temperature is a Monte Carlo simulation (see section 2.2) for the classical Heisenberg Hamiltonian (3.63). Its temperature dependence is introduced by (2.45). The thermal average (2.38) of the magnetization, the susceptibility, and the heat capacity is calculated via the importance sampling (2.42). Therein, the magnetization and its square are [43]

$$\overline{\boldsymbol{M}} = \frac{1}{N_\mathrm{MC}} \sum_{l=1}^{N_\mathrm{MC}} \sum_i \boldsymbol{m}_i \,, \tag{3.95}$$

$$\overline{|\boldsymbol{M}|^2} = \frac{1}{N_\mathrm{MC}} \sum_{l=1}^{N_\mathrm{MC}} \left| \sum_i \boldsymbol{m}_i \right|^2 . \tag{3.96}$$

These averages yield the magnetic susceptibility

$$\chi_T = \frac{1}{k_\mathrm{B} T} \left(\overline{\boldsymbol{M}^2} - (\overline{\boldsymbol{M}})^2 \right) . \tag{3.97}$$

The heat capacity C is obtained from the averages of the total energy

$$C = \frac{1}{k_\mathrm{B} T^2} \left(\overline{E^2} - (\overline{E})^2 \right) , \tag{3.98}$$

with

$$\overline{E} = \frac{1}{N_\mathrm{MC}} \sum_{l=1}^{N_\mathrm{MC}} E_l \,, \tag{3.99}$$

$$\overline{E^2} = \frac{1}{N_\mathrm{MC}} \sum_{l=1}^{N_\mathrm{MC}} E_l^2 \,. \tag{3.100}$$

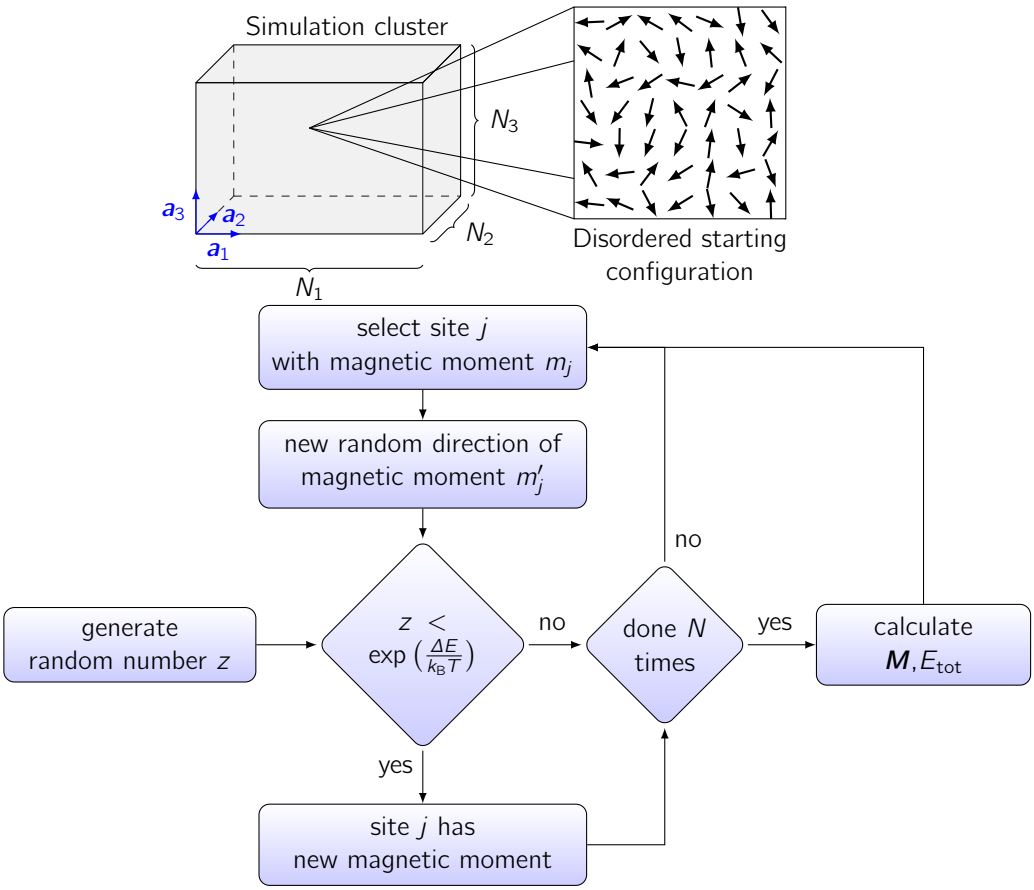

Figure 3.4: Schematic picture of the Monte Carlo procedure for one Monte Carlo step (see text). The averages of the magnetization $\boldsymbol{M}$ and the total energy E_l are taken over N_{MC} MC steps and are given by (3.95) or (3.99). At the top, the supercell and a disordered starting configuration are sketched.

The energy for every Monte Carlo step in (3.99) and (3.100) is calculated by taken into account the Heisenberg Hamiltonian (3.63)

$$E_l = -\sum_i \boldsymbol{m}_i \cdot \left[\left(\sum_j J_{ij} \boldsymbol{m}_j \right) + \mu_{\mathrm{B}} \boldsymbol{B} \right] . \tag{3.101}$$

The magnetic transition temperature can be traced in all these thermodynamic quantities. At T_{C}, the magnetization of a ferromagnet shows a second order phase transition with $M \neq 0$ for $T < T_{\mathrm{C}}$. For an antiferromagnet, the susceptibility, the heat capacity, or the Binder cumulant [43] is a better choice to obtain T_{N}. The susceptibility follows in general a Curie-Weiss law-like behavior above the transition temperature

$$\chi_T \propto \frac{1}{T - \Theta} , \tag{3.102}$$

with the Weiss temperature Θ, which depends on the magnetic character of the investigated material [70, page 56]

- $\Theta = 0$ for a paramagnet,
- $\Theta > 0$ for a ferromagnet with $\Theta = T_{\mathrm{C}}$,
- $\Theta < 0$ for a antiferromagnet with $\Theta = -T_{\mathrm{N}}$.

In the course of a practical calculation, the first-principles J_{ij} (3.82) were calculated within a small unit cell. This unit cell is repeated $N_1 \times N_2 \times N_3$ times in the direction of the three lattice vectors $\boldsymbol{a}_1$, $\boldsymbol{a}_2$, or $\boldsymbol{a}_3$ (see figure 3.4), since a large number of atoms is needed for reasonable statistics in the following MC simulation. Depending on the investigated system, periodic boundary conditions in one, two, or three dimensions can be applied modeling, e.g., a wire, a layer, or a bulk sample.

The schematic sequence of the Monte Carlo simulation is depicted by figure 3.4. Within the $N_1 \times N_2 \times N_3$ supercell, the magnetic moment at the lattice site i interacts with its neighbors at the site j via J_{ij}. In terms of section 2.2, the enemble of all magnetic moments $\{\boldsymbol{m}\}$ forms the configuration $\boldsymbol{c}_l$. During one MC run, a lattice site j with the magnetic moment vector $\boldsymbol{m}_j$ is chosen and a new direction of the magnetic $\boldsymbol{m}'_j$ is specified by random numbers. If the new magnetic moment $\boldsymbol{m}'_j$ is substituted in $\{\boldsymbol{m}\}$, it defines a new configuration $\boldsymbol{c}_{l'}$. The energy difference between the two configurations determines via (2.45) whether the moment at the lattice site j is either $\boldsymbol{m}'_j$ or $\boldsymbol{m}_j$. Performing this procedure for all N sites of the lattice is defined as one MC step.

Starting from a high-temperature disordered state above T_{t} (see figure 3.4), the temperature was stepwise reduced by 5 K. At every temperature T, the thermal equilibrium is expected to be reached after 20 000 MC steps. Afterwards, the thermal averages were computed over additional 20 000 MC steps. Further computational details of this MC scheme can be found in [54, 80, 81].

Finally, $T_{\mathrm{t}}^{\mathrm{MC}}$ was obtained from the fitting of the temperature dependency of the magnetic susceptibility, crosschecked by the temperature dependence of the saturation magnetization or the heat capacity. The obtained transition temperatures have been observed within an uncertainty range of ± 5 K. In addition, the kind of magnetic order at the ground state was obtained from the orientation of the magnetic moments at low temperatures and the temperature dependence of χ_T (3.102).

3.4. Disorder

All material properties discussed until know are only considered for a perfect periodic crystal structure with a particular chemical composition. However, chemical and magnetic disorder might be present in any material either as points defect like, e.g., a missing or an additional atom, or as the mixing of two or more metallic components in an alloy. When chemical disorder appears, one or more sublattices i in a periodically repeated unit cell might be occupied by two or more atomic types having a noninteger occupation number σ_i. This is for a binary system with two atomic types A and B expressed as the spinlike occupation number operator

$$\sigma_i = \begin{cases} +1 & \text{type A} \\ -1 & \text{type B} \end{cases} . \tag{3.103}$$

A typical examples of an alloy is the metallic, binary solid solution Ag-Pd, which is totally miscible at all concentrations [E12].

For the description of such order/disorder, the n-site correlation function

$$\xi_f^{(n)} = \langle \underbrace{\sigma_i \sigma_j \ldots \sigma_k}_{\text{including } n\text{-sites}} \rangle_f \,, \tag{3.104}$$

with the average $\langle \cdot \rangle_f$ over all sites i in the cluster f has to be considered. It describes in statistical physics the variation of the system density with respect to a reference particle – the short-range order (SRO). This concept is more generally useful for fluids, gases, colloids etc., where the function depends smoothly from radius r around the reference point. In the case of a solids, the function shows only delta peaks when r matches the radii of the coordination shells.

The pair correlation function ($n = 2$) for the first coordination shell $\xi_1^{(2)} = \langle \sigma_i \sigma_j \rangle_f$ is used, e.g., by Peil *et al.* [82]. It is connected with another often used disorder description, the Warren-Cowley SRO parameter, via [82]

$$\alpha_1 = \frac{\xi_1^{(2)} - \sigma^2}{1 - \sigma^2} \,. \tag{3.105}$$

The pair correlation function is in (3.105) compared with the one of the completely disordered configuration $\xi_1^{(2)} = \sigma^2$. It corresponds to $\sigma = 2c - 1 \equiv \xi^{(1)}$ in a binary system of atomic types A and B with the concentrations $c_A = c$ and $c_B = 1 - c$, respectively.

The original definition of the Warren-Cowley SRO parameter for the s-th shell while being at a site with a B atom is [83, 84]

$$\alpha_s = 1 - \frac{n_s}{c_A C_s} \,, \tag{3.106}$$

where n_s is the number of A atoms among the C_s atoms in the s-th shell (coordination number C_s). Another way to write (3.106) is defined by the probability $p_{BA}(r) = n_s / C_s$ of finding a A atom at the distance r around a B atom

$$\alpha_{BA}(r) = 1 - \frac{p_{BA}(r)}{c_A} \,. \tag{3.107}$$

The SRO parameter is smaller than zero for an ordered system, zero for a completely random disorder, and positive in case of segregation. The minimum depends on the concentration of the different types [85, 86]

$$-\frac{c}{1-c} \leq \alpha_1 \leq 1, \quad c \leq 1/2 \,, \tag{3.108}$$

$$-\frac{1-c}{c} \leq \alpha_1 \leq 1, \quad c \geq 1/2 \,, \tag{3.109}$$

which is derived from simple probability arguments.

These definitions were used to quantify different amounts of short-range order, since the underlying multiple scattering theory of the Green's function method is well suited to handle disorder or impurities. In particular, the separation of structural and chemical contributions in (2.33) or the Dyson equation (2.24) allows the introduction of an effective medium taking into account different chemical occupation.

3.4.1. Impurity model and embedded clusters

The most simple approximation of a disordered material can be understood as a single impurity atom in a perfect host structure, which is actually not real disorder but a point defect. The multiple scattering is particular well suited to solve such an impurity problem [7].

A single impurity atom sitting at the lattice origin in an ideal host crystal can be treated as a perturbation of the host material. It is considered in the t matrices (2.31) [36, section 23.5.1]

$$\underline{t}^n(\varepsilon) = \begin{cases} \underline{t}_{\text{imp}}(\varepsilon) & n = 0\,, \\ \underline{t}_{\text{host}}(\varepsilon) & \forall n \neq 0\,. \end{cases} \tag{3.110}$$

When they are explicitly plugged into the expression of the scattering path operator (2.28), it follows

$$\begin{aligned} \underline{\tau}^{nm}(\varepsilon) = {} & \underline{t}_{\text{host}}(\varepsilon)\left(\delta_{nm} + \sum_{k\neq n} \underline{G}_0^{nk}(\varepsilon)\underline{\tau}^{km}(\varepsilon)\right) \\ & + \delta_{i0}\left[\left(\underline{t}_{\text{imp}}(\varepsilon) - \underline{t}_{\text{host}}(\varepsilon)\right)\left(\delta_{0j} + \sum_{k\neq 0} \underline{G}_0^{0k}(\varepsilon)\underline{\tau}^{km}(\varepsilon)\right)\right]. \end{aligned} \tag{3.111}$$

The impurity t matrix in (3.111) violates the translational invariance of the lattice. This problem can be circumvented by a lattice Fourier transformation, which yields [36]

$$\begin{aligned} \underline{\tau}(\varepsilon;\boldsymbol{k},\boldsymbol{k}') = {} & \underline{t}_{\text{host}}(\varepsilon)\left(\delta_{\boldsymbol{k}\boldsymbol{k}'} + \underline{G}_0(\varepsilon;\boldsymbol{k})\underline{\tau}(\varepsilon;\boldsymbol{k},\boldsymbol{k}')\right) \\ & + |O_{\text{tg}}|^{-1}\left(\underline{t}_{\text{imp}}(\varepsilon) - \underline{t}_{\text{host}}(\varepsilon)\right)\left(1 + \sum_{\boldsymbol{k}''} \underline{G}_0(\varepsilon;\boldsymbol{k}'')\underline{\tau}(\varepsilon;\boldsymbol{k}'',\boldsymbol{k}')\right). \end{aligned} \tag{3.112}$$

The quantity O_{tg} in (3.112) is the order of the translational group of the lattice consisting of the host atoms only. By defining in correspondence with (2.33)

$$\underline{\tau}_{\text{host}}(\varepsilon;\boldsymbol{k}) = \left[\underline{t}_{\text{host}}^{-1}(\varepsilon) - \underline{G}_0(\varepsilon;\boldsymbol{k})\right]^{-1}, \tag{3.113}$$

$$\underline{\tau}_{\text{host}}^{00}(\varepsilon) = |O_{\text{tg}}|^{-1}\sum_{\boldsymbol{k}} \underline{\tau}_{\text{host}}(\varepsilon;\boldsymbol{k})\,, \tag{3.114}$$

Equation (3.112) can be rewritten as

$$\begin{aligned} \underline{\tau}(\varepsilon;\boldsymbol{k},\boldsymbol{k}') = {} & \underline{t}_{\text{host}}(\varepsilon)\delta_{\boldsymbol{k}\boldsymbol{k}'} \\ & - |O_{\text{tg}}|^{-1}\underline{\tau}_{\text{host}}(\varepsilon;\boldsymbol{k})\underline{D}_{\text{imp}}^{00}(\varepsilon)\left(\underline{t}_{\text{imp}}^{-1}(\varepsilon) - \underline{t}_{\text{host}}^{-1}(\varepsilon)\right)\underline{\tau}_{\text{host}}(\varepsilon;\boldsymbol{k}')\,, \end{aligned} \tag{3.115}$$

with the so-called *impurity matrix*

$$\underline{D}_{\text{imp}}^{00}(\varepsilon) = \left[\underline{1} + \underline{\tau}_{\text{host}}^{00}(\varepsilon)\left(\underline{t}_{\text{imp}}^{-1}(\varepsilon) - \underline{t}_{\text{host}}^{-1}(\varepsilon)\right)\right]^{-1}. \tag{3.116}$$

Finally, the scattering path operator at the origin is

$$\underline{\tau}^{00}(\varepsilon) = |O_{\mathrm{tg}}|^{-1} \sum_{\boldsymbol{k},\boldsymbol{k}'} \underline{\tau}(\varepsilon;\boldsymbol{k},\boldsymbol{k}') = \underline{D}^{00}_{\mathrm{imp}}(\varepsilon)\underline{\tau}^{00}_{\mathrm{host}}(\varepsilon)\,. \tag{3.117}$$

and can be used to determine e.g. the charge density, the density of states or any other desired physical observable.

In summary, the single-scattering t matrices in (2.33) were substituted for particular impurity sites. The same concept can be generalized either in an effective description of random disorder in the coherent potential approximation (CPA) described in section 3.4.2 or for the embedded cluster method [36, section 24]. The latter takes into account not a single impurity as (3.110) but a whole cluster $\mathcal{C} = \{\boldsymbol{R}_n\}$ of impurities or interacting host atoms with the single-site scattering t matrices

$$\underline{t}^n(\varepsilon) = \begin{cases} \underline{t}^n(\varepsilon) & \boldsymbol{R}_n \in \mathcal{C}\,, \\ \underline{t}_{\mathrm{host}}(\varepsilon) & \boldsymbol{R}_n \notin \mathcal{C}\,. \end{cases} \tag{3.118}$$

Thereby, two diagonal supermatrix quantities are defined. When only unperturbed host atoms would occupy $\mathcal{C}$

$$\underline{\boldsymbol{t}}_{\mathrm{host}}(\varepsilon) = \left\{\underline{t}^n(\varepsilon)\delta_{nm} | \underline{t}^n(\varepsilon) = \underline{t}_{\mathrm{host}}(\varepsilon), \forall \boldsymbol{R}_n \in \mathcal{C}\right\}, \tag{3.119}$$

or the cluster is actually occupied

$$\underline{\boldsymbol{t}}_{\mathcal{C}}(\varepsilon) = \left\{\underline{t}^n(\varepsilon)\delta_{nm} | \underline{t}^n \neq \underline{t}_{\mathrm{host}}(\varepsilon), \forall \boldsymbol{R}_n \in \mathcal{C}\right\}. \tag{3.120}$$

The following scattering path operator comprising all sites of $\mathcal{C}$ is

$$\underline{\tau}_{\mathcal{C}}(\varepsilon) = \underline{\tau}_{\mathrm{host}}(\varepsilon)\left[1 - \left(\underline{\boldsymbol{t}}^{-1}_{\mathrm{host}}(\varepsilon) - \underline{\boldsymbol{t}}^{-1}_{\mathcal{C}}(\varepsilon)\right)\underline{\tau}_{\mathrm{host}}(\varepsilon)\right]^{-1}, \tag{3.121}$$

similar as (3.117) with (3.116).

3.4.2. Substitutional disorder

The same ideas as for the impurity model were used to model a locally unknown distribution of different atomic species through an effective medium description – the coherent potential approximation (CPA) [18, 19]. The same single-site t matrix $\underline{t}_{\mathrm{c}}$ appears on every scattering site of a coherent lattice, which restores on-average the translational invariance. Therewith, the site-diagonal scattering path operator can be expressed similar to (2.33) [36, section 23.7]

$$\underline{\tau}^{ij}(\varepsilon) = \frac{1}{\Omega_{\mathrm{BZ}}} \int_{\Omega_{\mathrm{BZ}}} \mathrm{d}\boldsymbol{k}\, \left(\underline{t}^{-1}_{\mathrm{c}}(\varepsilon) - \underline{G}_0(\varepsilon;\boldsymbol{k})\right)^{-1} \mathrm{e}^{\mathrm{i}\boldsymbol{k}\cdot(\boldsymbol{R}_n - \boldsymbol{R}_m)}\,. \tag{3.122}$$

By using the *restricted ensemble average* described in [36, section 23.2], the scattering path operator for the unit cell at the origin[7] can be written

$$\langle \underline{\tau}^{00}_{\mathrm{c}}(\varepsilon)\rangle_{(0=\alpha)} \equiv \underline{\tau}^{00}_{\alpha}(\varepsilon)\,, \tag{3.123}$$

[7]The index 0 labels an arbitrarily chosen unit cell (notation used as in [36]).

where

$$\underline{\tau}_{\alpha}^{00}(\varepsilon) = \underline{D}_{\alpha}^{00}(\varepsilon)\underline{\tau}_{c}^{00}(\varepsilon)\,, \tag{3.124}$$

and

$$\underline{D}_{\alpha}^{00}(\varepsilon) = \left[\underline{1} + \underline{\tau}_{c}^{00}(\varepsilon)\left(\underline{t}_{\alpha}^{-1}(\varepsilon) - \underline{t}_{c}^{-1}(\varepsilon)\right)\right]^{-1}. \tag{3.125}$$

In (3.123), α represents one atomic type, e.g., either A or B for a binary material system A_cB_{1-c}. The impurity matrix (3.125) resembles the one in (3.116) but exhibits now an adapted scattering path operator and single-site t matrix which match to the CPA problem. Then, the CPA condition can be expressed equivalently in different notations

$$c\underline{\tau}_{A}^{00}(\varepsilon) + (1-c)\underline{\tau}_{B}^{00}(\varepsilon) = \underline{\tau}_{c}^{00}(\varepsilon)\,, \tag{3.126}$$

$$c\underline{D}_{A}^{00}(\varepsilon) + (1-c)\underline{D}_{B}^{00}(\varepsilon) = \underline{1}\,, \tag{3.127}$$

$$c\underline{X}_{A}^{00}(\varepsilon) + (1-c)\underline{X}_{B}^{00}(\varepsilon) = \underline{0}\,, \tag{3.128}$$

with the *excess scattering matrix*

$$\underline{X}_{\alpha}(\varepsilon) = \left[\left(\underline{t}_{\alpha}^{-1}(\varepsilon) - \underline{t}_{c}^{-1}(\varepsilon)\right) + \underline{\tau}_{c}^{00}(\varepsilon)\right]^{-1}. \tag{3.129}$$

The CPA conditions (3.126) to (3.128) have to be iterated self-consistently, since the initial single-site t matrix in (3.122) is only a guess.

In particular (3.128) allows an efficient numerical solution [87, 88]. If it is assumed that (3.128) is not fullfilled in the n-th step of the self-consistent iteration, a nonzero matrix is given in the n-th step

$$\underline{X}_{c}^{(n)}(\varepsilon) \equiv \sum_{\alpha=1}^{m} c_{\alpha}\underline{X}_{\alpha}^{(n)}(\varepsilon) \neq 0\,;\ \sum_{\alpha=1}^{m} c_{\alpha} = 1\,, \tag{3.130}$$

with the generalization to m components. A guess for the coherent t matrix is found by substituting $\underline{t}_{c}(\varepsilon)$ in (3.129) by the t matrix of the n-th step $\underline{t}_{c}^{(n)}(\varepsilon)$

$$\left(\underline{t}_{c}^{(n+1)}(\varepsilon)\right)^{-1} = \left(\underline{t}_{c}^{(n)}(\varepsilon)\right)^{-1} - \left[\left(\underline{X}_{\alpha}^{(n)}(\varepsilon)\right)^{-1} + \underline{\tau}_{c}^{00(n)}(\varepsilon)\right]^{-1}. \tag{3.131}$$

The latter equation shows a stable convergence by starting from the initial ansatz of the average t matrix approximation (ATA) [87]

$$\underline{t}_{c}^{(0)} = \sum_{\alpha=1}^{m} c_{\alpha}\underline{t}_{\alpha}(\varepsilon)\,. \tag{3.132}$$

In terms of the SRO parameter, this fully random distribution modeled by the CPA represents the completely uncorrelated case $\alpha = 0$. It covers the most pronounced concentration effects of the chemical disorder but is only a single-site approximation of the complete problem.

The above equations can be again generalized for a complex lattice with more then one sublattice using as before in section 2.1.3 the concept of a supermatrix for the coherent single-site t matrix [36, section 23.7.2]

$$\underline{t}_{\mathrm{c}}^{-1}(\varepsilon) = \begin{pmatrix} \ddots & & & & \\ & \left(\underline{t}_{\mathrm{X}}^{i}(\varepsilon)\right)^{-1} & \underline{0} & \underline{0} & \\ & \underline{0} & \left(\underline{t}_{\mathrm{c}}^{j}(\varepsilon)\right)^{-1} & \underline{0} & \\ & \underline{0} & \underline{0} & \left(\underline{t}_{\mathrm{Y}}^{k}(\varepsilon)\right)^{-1} & \\ & & & & \ddots \end{pmatrix} . \tag{3.133}$$

In (3.133), the ordered sublattice i is occupied by atomic type X, the ordered sublattice k by Y and the sublattice j varies statistically between either A or B. This approach represents a single-site, multi-sublattice CPA (MS-CPA) [89]. The SRO parameter for a MS-CPA setup might be already nonzero depending on the choice of the complex lattice structure. An example of a complex supercell is discussed in section 6.2.2 for the AgPd alloy. Its physical properties were compared with results for $\alpha = 0$.

3.4.3. Disordered magnetic moments

The same theoretical ideas as used for the CPA allow to describe disordered magnetic states at finite temperatures. In contrast, conventional *ab initio* calculations describe the ground state at 0 K. They provide often good results for ordered magnetic systems but fail in the description of the paramagnetic state above the magnetic transition temperature T_{t}.

In the disordered local moment theory (DLM) [90, 91], arrangements of local magnetic moments $\{\boldsymbol{S}_i\}$ at the sites i are assumed to fluctuate independently from each other. Above T_{t}, the orientations of those local moments are randomly distributed and the average magnetization per site is zero. It is modeled within the CPA with two single-site t matrices, one with spin up and the other with spin down. The resulting scattering path operator for the effective medium $\underline{\tau}_{\mathrm{c}}^{ij}$ can be plugged into (3.82) and the corresponding J_{ij} are calculated. In practice, it can be understood as a change of the underlying reference state for the J_{ij} calculation. Thus, the J_{ij} are calculated either for the ground state at 0 K or for the paramagnetic state at a high temperature. In order to distinguish between both approximations, the labels $\mathrm{RS}_{\mathrm{FM}}$ and $\mathrm{RS}_{\mathrm{PM}}$ were introduced for the ferromagnetic or the paramagnetic reference state, respectively.

Few general conclusions can be drawn from the idea of the random orientation of the magnetic moments. It causes, on the one hand, an increase in the extent of the orbitals. Since the overlap of the involved orbitals determines strongly the strength of the magnetic exchange interactions, the strength of the J_{ij} becomes larger, in case of a DLM calculation. This means that the resulting transition temperature can either be enhanced or reduced, depending on the type of magnetic exchange, e.g., a reduction for antiferromagnetic (super-) exchange. On the other hand, in the paramagnetic phase, the total magnetization inside the unit cell vanishes, which will erase induced magnetic moments.

Although the DLM model was applied successfully in previous studies, it is still based on a single-site approximation. An indication of this problem was found for the investi-

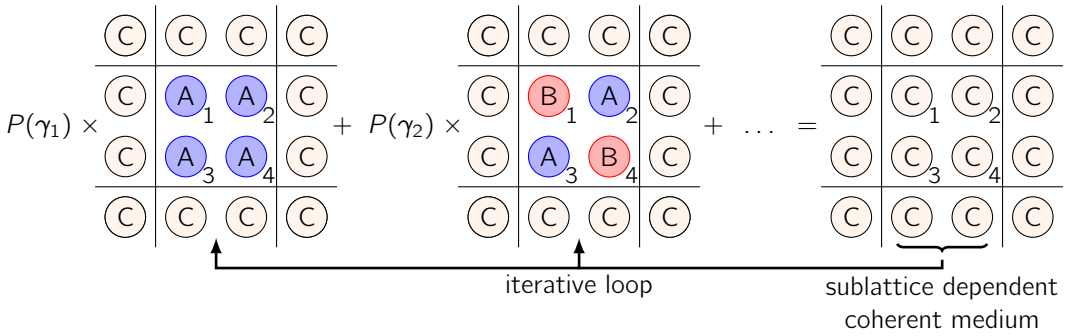

Figure 3.5: Sketch of the MS-NL-CPA for a lattice with four basis sites ($N_{\text{sub}} = 4$ and $N_{\text{c}} = 1$) and two kinds A and B. It results in $2^{N_{\text{sub}}} = 2^4 = 16$ possible configurations γ_i with $i = 1, \ldots, 16$. They are weighted with the probabilities $P(\gamma_i)$.

gation of the magnetic properties of Ni. Only a non-local DLM approach could describe the moments in Ni sufficiently [92, 93]. This approach, however, involves too much computational effort for complex unit cells and could not be used in this thesis.

3.4.4. Including short-range order

Although the CPA appeared often as a powerful tool describing all kinds of disorder, it remains a single-site approximation. Therefore, a strong interest exists to extent the CPA scheme using, e.g., a supercell approach but taking into account local environment effects [82].

An alternative approach, the multi-sublattice, non-local extension of the original CPA theory (MS-NL-CPA) is implemented within HUTSEPOT [21]. The goal of this development was the self-consistent construction of a richer effective medium description for a partially disordered system. The condition (3.128) of on-average no extra scattering from any portion of the bulk is generalized to multisite substitutions involving more than one atom at the time. The general concept of the MS-CPA remains the same, but instead of a single t matrix a cavity with more than one sublattice is introduced (sketched in figure 3.5 for 4 sublattices).

The corresponding scattering path operator that replaces (3.122) reads in particular [21, E12]

$$\underline{\tau}_{I,s;J,t}(\varepsilon) = \frac{1}{\Omega} \sum_{n=1}^{N_{\text{c}}} \left(\int_{\Omega_{\boldsymbol{K}_n}} \mathrm{d}\boldsymbol{k} \, \left(\underline{t}^{s,t}(\varepsilon; \boldsymbol{K}_n) - \underline{G}_0^{s,t}(\varepsilon; \boldsymbol{k}) \right)^{-1} \right)_{I,s;J,t} \mathrm{e}^{+\mathrm{i}\boldsymbol{K}_n \cdot (\boldsymbol{R}_I - \boldsymbol{R}_J)} , \tag{3.134}$$

where $\{\boldsymbol{K}_n\}$ denotes a set of $I, J = 1, \ldots, N_{\text{c}}$ *cluster momenta* [94] in a coarse grained treatment of reciprocal space [95]. The original Brillouin zone Ω is now partitioned into sub-regions $\Omega_{\boldsymbol{K}_n}$ of alike effective medium properties, while explicit dependence on the direct space sublattice indexes $s, t = 1, \ldots, N_{sub}$ and a matching phase modification of the structure constants allows to generalize the original non-local treatment to cases of complex unit cells in arbitrary geometries. The vectors $\boldsymbol{R}_I$, $\boldsymbol{R}_j$ and $\boldsymbol{K}_n$ refer to a lattice Fourier transform.

Table 3.1: List of the $N_{\text{sub}} = 2$ nonequivalent sublattices used in the supercell with basis vectors: $\boldsymbol{R}_1 = a_{\text{lat}}(0, 1/2, 1/2)$, $\boldsymbol{R}_2 = a_{\text{lat}}(1/2, 0, 1/2)$, $\boldsymbol{R}_3 = a_{\text{lat}}(1, 1, 0)$.

Sublattice	Origin	Sublattice	Origin
$\boldsymbol{a}_1$	$(0, 0, 0)$	$\boldsymbol{a}_2$	$(1/2, 1/2, 0)$

The established CPA procedure for the self-consistent determination of the effective medium is then followed straightforwardly. In particular, different assumptions concerning the degree of SRO to be modeled enter the framework in terms of a multisite probability distribution $P(\gamma)$ for combined element substitutions in certain configurations $\gamma = \{\gamma_{1,1}, \ldots, \gamma_{I,s}, \ldots, \gamma_{N_c, N_{\text{sub}}}\}$

$$\underline{\tau}(\varepsilon) = \sum_{\gamma}^{N_{tot}} P(\gamma) \underline{\tau}_{\gamma}(\varepsilon)\,, \tag{3.135}$$

with $N_{tot} = N_c \times N_{\text{sub}}$.

The underlying concept of the MS-NL-CPA is shown with an example system of a binary alloy in fcc structure. In the usual CPA only one sublattice would be needed but for a further approximation of SRO $N_{\text{sub}} = 2$ might be used. The structure of such a cell is given in table 3.1.

With a binary alloy of A and B type atoms, there are 4 different possible configurations γ_i going into (3.135):

$$\gamma_1 = \{A, A\},\ \gamma_2 = \{A, B\},\ \gamma_3 = \{B, A\},\ \text{and}\ \gamma_4 = \{B, B\}\,. \tag{3.136}$$

Their probability $P(\gamma_i)$ is the parameter to model different short-range order scenarios. But the $P(\gamma_i)$ are not completely free to chose and, since the sum of the probabilities and the type concentrations have to be one, they have to satisfy the following restrictions

$$\sum_i P(\gamma_i) = 1\,, \tag{3.137}$$

$$1/N_{\text{sub}} \sum_i P(\gamma_i) \times \widehat{N}_A[\gamma_i] = c_A\,, \tag{3.138}$$

$$1/N_{\text{sub}} \sum_i P(\gamma_i) \times \widehat{N}_B[\gamma_i] = c_B = 1 - c_A\,, \tag{3.139}$$

where the counting operator $\widehat{N}_A[\gamma_i]$ gives the number of type A in the configuration γ_i.

3.4.5. A short-range order parameter for the MS-NL-CPA

The above tools allow to treat also systems with short-range order, but for further analysis it is useful to have some quantification of this short-range order. The Warren-Cowley SRO parameter and the pair correlation function can be still used in a modified manner. The simple example from above with the cell from table 3.1 and the configurations (3.136) will be used to demonstrate the method. The probabilities for the example will be set to be

$$P(\gamma_1) = 0,\ P(\gamma_2) = 1/2,\ P(\gamma_3) = 1/2,\ \text{and}\ P(\gamma_4) = 0\,. \tag{3.140}$$

With the Warren-Cowley SRO parameter

The definition of the Warren-Cowley SRO parameter (3.106) was originally used in a simple context. The surrounding of an atom should be clearly determined. By using the MS-NL-CPA, it is defined what is inside the cavity but the outside remains mainly undefined via the effective medium. This coherent medium (the sites marked with C in figure 3.5) due to the preserved translational invariance could be thought of a periodic lattice filled with the configurations distributed according to their probabilities. With this assumption, (3.106) can be used in several steps to derive an averaged SRO parameter:

1. The sites of the coherent medium will have a probability $P_{C,A}$ to find a type A atom, which is given by

$$P_{C,A}(j_{\text{sub}}) = \sum_{i}^{N_{\text{conf}}} P(\gamma_i)(\sigma_{j_{\text{sub}}} + 1)/2\,, \tag{3.141}$$

   and depends on the sublattice j_{sub}, the configuration γ_i, and their probabilities $P(\gamma_i)$. The last product in (3.141) $(\sigma_{j_{\text{sub}}} + 1)/2$ varies between 0 and 1, since the occupation operator σ_i in (3.103) is ± 1 for A or B, respectively.

   Example: Both sublattices have in one γ an A atom and in the other a B atom with $P(\gamma_i) = 0.5$. So, $(\sigma_{j_{\text{sub}}} + 1)/2$ is zero or one for either a B or an A atom, respectively, and the sum is for each sublattice $P_{C,A}(j_{\text{sub}}) = 0.5$.

2. Inside the cell, the probability on each sublattice p_{BA} is defined separately for each configuration γ_i and is either 0 or 1 ($(\sigma_{j_{\text{sub}}} + 1)/2$).

   Example: $(\sigma_{j_{\text{sub}}} + 1)/2$ will be calculated for $\gamma_2 \to \{1, 0\}$ and $\gamma_3 \to \{0, 1\}$.

3. The previous points are combined for every γ_i in the probability to find an A type atom around a B type atom in the different coordination spheres s, which includes C_s sites

$$p^{BA}(s) = {}^{1}/_{C_s} \sum^{C_s} \begin{cases} (\sigma_{j_{\text{sub}}} + 1)/2 & \text{inside the cell} \\ P_{C,A}(j_{\text{sub}}) & \text{outside the cell} \end{cases} \tag{3.142}$$

   Example: There are 12 sites in the first coordination sphere of a fcc lattice. For γ_3, eleven of the sites have a probability of 0.5 and one of them has 1 ($j_{\text{sub}} = 2$ inside

the cell) [8]

$$p_1^{BA}(\gamma_3, j_{\text{sub}} = 1) = {}^{(11\times 0.5+1)}/_{12} = 0.541\overline{6} \tag{3.143}$$
$$p_1^{BB}(\gamma_3, j_{\text{sub}} = 1) = {}^{(11\times 0.5)}/_{12} = 0.458\overline{3} \tag{3.144}$$
$$p_1^{AB}(\gamma_3, j_{\text{sub}} = 2) = {}^{(11\times 0.5+1)}/_{12} = 0.541\overline{6} \tag{3.145}$$
$$\alpha_1^{BA}(\gamma_3, j_{\text{sub}} = 1) = 1 - {}^{p_1^{BA}(\gamma_3,1)}/_{c_A} = -0.08\overline{3} \tag{3.146}$$
$$\alpha_1^{BB}(\gamma_3, j_{\text{sub}} = 1) = 1 - {}^{p_1^{BB}(\gamma_3,1)}/_{c_B} = 0.08\overline{3} \tag{3.147}$$
$$\alpha_1^{AB}(\gamma_3, j_{\text{sub}} = 2) = 1 - {}^{p_1^{AB}(\gamma_3,2)}/_{c_B} = -0.08\overline{3}\,. \tag{3.148}$$

4. The SRO parameter for a particular configuration and the s-th shell $\alpha_s(\gamma_i)$ is given by the arithmetic average of $\alpha_s^{BA}(\gamma_i)$ over all sublattices in the cell. Thereby, $\alpha_s^{BA}(\gamma_i)$ or $\alpha_s^{AB}(\gamma_i)$ are used depending on the type of atom sitting on the sublattice.

   Example: The SRO parameter of every shell will be averaged for the two sublattices. For $\gamma_3 = \{B, A\}$, it will be

$$\alpha_1(\gamma_3) = \left(\alpha_1^{BA}(\gamma_3, j_{\text{sub}} = 1) + \alpha_1^{AB}(\gamma_3, j_{\text{sub}} = 2)\right)/2 = -0.08\overline{3} \tag{3.149}$$

5. The SRO parameter per shell is derived by considering also the configuration probabilities

$$\alpha_s = \sum_i^{N_{\text{conf}}} P(\gamma_i) \times \alpha_s(\gamma_i)\,. \tag{3.150}$$

   Example: The probabilities and the SRO parameter for γ_2 and γ_3 are similar and the other contributions are zero. So, the sum is simple and the result is $\alpha_1 = -0.08\overline{3}$.

6. For a possible average over the shells, the coordination number C_s is used [97]

$$\overline{\alpha}_{N_{\text{shell}}} = \sum_s^{N_{\text{shell}}} C_s \times \alpha_s \Big/ \sum_s^{N_{\text{shell}}} C_s\,. \tag{3.151}$$

The latter equation appears problematic in its usage, since, the upper summation boundary is not well defined as it will be showed below. Anyway, the parameter of the nearest neighbor shell is a first measure of some additional SRO. They are given for some probabilities $P(\gamma_i)$ in table 3.2. The most of the probability choices are degenerated with respect to the γ_2 and γ_3 due to the symmetry of the cell (see table 3.1). The nearest neighbor SRO parameters are restricted to $-1/12 \leq \alpha_1 \leq 1/12$ for maximal "order" ($\gamma_2 = \gamma_3 = 0.5$) and maximal cluster sizes ($\gamma_1 = \gamma_4 = 0.5$). This results from the small cell size with N_{sub}. Taking only one configuration under the restrictions of (3.137) to (3.139) means only γ_2 or γ_3 and returns unfortunately zero – completely uncorrelated – similar with $P(\gamma_i) = 0.25$. This is an undesired result, which is as well correlated with the choice of unit cell.

[8] This is essentially the same setup described by Takano *et al.* [96]. However, their SRO parameter value could not be reproduced. The reason for this might lie in some assumptions made by the authors but not described in their work.

Table 3.2: The calculated nearest neighbor SRO parameters, α_1 and α_1^{stat}, obtained via (3.150) or (3.105) for two atomic types and $c = 0.5$. The used configurations γ_i are given in (3.136). The underlying lattice structure with $N_{\text{sub}} = 2$ is described in table 3.1. The probabilities $P(\gamma_i)$ were varied in steps of 0.05. Here only a fraction of the information is shown. The complete table is presented in the appendix as table B.1. All entries, except those marked with 1 in the first column, are symmetric in the γ_2 and γ_3 configurations.

	probability P of					
sym	γ_1	γ_2	γ_3	γ_4	α_1	α_1^{stat}
1	0	0.5	0.5	0	−0.083 333	−0.083 620
	0	0.45	0.55	0	−0.082 500	−0.082 255
	0	0.4	0.6	0	−0.08	−0.080 198
	0	0.35	0.65	0	−0.075 833	−0.075 838
	0	0.3	0.7	0	−0.07	−0.070 104
1	0.05	0.45	0.45	0.05	−0.066 667	−0.066 253
	⋮	⋮	⋮	⋮	⋮	⋮
	0.15	0.05	0.65	0.15	−0.003 333	−0.003 476
	0	0	1	0	0	0
1	0.25	0.25	0.25	0.25	0	−0.000 026
	0.05	0	0.9	0.05	0.000 833	0.000 871
	0.25	0.2	0.3	0.25	0.000 833	0.000 736
	0.25	0.15	0.35	0.25	0.003 333	0.003 662
	⋮	⋮	⋮	⋮	⋮	⋮
1	0.45	0.05	0.05	0.45	0.066 667	0.067 142
	0.45	0	0.1	0.45	0.067 500	0.067 752
1	0.5	0	0	0.5	0.083 333	0.083 534

With the pair correlation function

For the verification of the previous results, the pair correlation function is used as a statistical and more direct approach. The idea of a periodic lattice filled with the configurations distributed according to their probabilities could be applied to a large cluster built of unit cells, which are occupied by the particular configurations γ_i.

A *Mathematica* notebook was developed to build a cluster with the lattice parameters of table 3.1 and occupy the unit cells therein according to the configuration probabilities of table 3.2. The actual procedure to determine the SRO parameter for this cluster was the following:

1. generate a cluster according to the lattice vectors,
2. occupy the cells randomly with the configurations γ_i according to their $P(\gamma_i)$,
3. determine $\xi_1^{(2)}$ as an average over all sites,

4. determine α_1^{stat} with (3.105).

These four steps define a statistical process which depends on the size of the cluster. In order to have a meaningful value, the cluster generation was repeated 1000 times for clusters of 1458 sites. The resulting nearest neighbor SRO parameter α_1^{stat} agreed well with α_1 obtained from (3.150) (see table 3.2).

Determine probabilities for given SRO parameter

Until now, the SRO parameter is defined for a particular choice of probabilities $P(\gamma_i)$ but the typical problem would be vice versa. As already seen from table 3.2, the number of configurations for a unit cell and the occupying atoms is fixed. By changing continuously the probabilities under the restrictions (3.137) to (3.139), the space of possible SRO parameters for a particular N_{sub} can be sampled.

For the above example with $N_{\text{sub}} = 2$ and $c = 0.5$, the four different configurations form together with the three restrictions a system of equations

$$P(\gamma_1) + P(\gamma_2)/2 + P(\gamma_3)/2 = c_A = 1/2\,, \tag{3.152}$$

$$P(\gamma_2)/2 + P(\gamma_3)/2 + P(\gamma_4) = c_B = 1/2\,, \tag{3.153}$$

$$\sum_i P(\gamma_i) = 1\,, \tag{3.154}$$

while each probability has to be $0 \leq P(\gamma_i) \leq 1$. The solution leaves $P(\gamma_3)$ free and for $P(\gamma_4)$ a upper boundary

$$P(\gamma_1) = P(\gamma_4)\,, \tag{3.155}$$

$$P(\gamma_2) = 1 - P(\gamma_3) - 2P(\gamma_4)\,, \tag{3.156}$$

$$\text{only if } P(\gamma_4) \leq \frac{1 - P(\gamma_3)}{2}\,. \tag{3.157}$$

However, this simple consideration of probabilities on the basis of configurations, restrictions and occupation is not possible for larger cells or more atomic types than two because the number of parameters increases while the number of equations remains the same. But it is always possible to sample all the free parameters $P(\gamma_i)$ by brute force. It is shown in an explicit application to the $\text{Ag}_c\text{Pd}_{1-c}$ alloy system for a $N_{\text{sub}} = 4$ cell in section 6.4.

3.5. Numerical calculations within the GF method

The computed results of numerical calculations suffer always from the limitations of the chosen approximations. Particular calculations might depend on the calculation settings. For the GF method, one critical calculation parameter is the cut-off $l_{\max}$ for the expansion of the Green's function into spherical harmonics (3.1), since it is not possible to take an infinite number of basic functions in this expansion. On the other hand, if the Green's function is considered for a periodic lattice, a Fourier transformation with a finite number of $\boldsymbol{k}$ points in the reciprocal space for the sampling of the Brillouin zone is computed (see

(3.122)). Also the chosen approximation for the description of the scattering potentials influences the numerical results (see section 2.1.4).

However, the variation in the numerical results with the discussed calculations parameters becomes smaller, if $l_{\max}$ or the number of $\boldsymbol{k}$ points is gradually increased. This convergence behavior is always verified previous to the final choice of a calculation setting, but also varies for the different physical quantities. Nevertheless, the electronic structure and the magnetic properties are in particular less sensitive to the choice of $l_{\max}$ etc. Thus, the calculation setup throughout this thesis is given by $l_{\max} = 3$ for the angular momentum cut-off and a $\boldsymbol{k}$ point mesh by $12 \times 12 \times 12$ for the Brillouin zone integration, unless stated otherwise. The complex energy contour for, e.g., the charge density given in (3.5) was integrated over 24 Gaussian quadrature points.

On the contrary, the numerical results for the total energy to determine the elastic properties are much more sensitive to the choice of $l_{\max}$ etc. [E12]. The problem of numerical convergence for those quantities is reviewed in section 6.1 for pure Pd and Ag in the fcc structure.

Chapter 4.

Single Impurity Rare Earth Atoms

Heavy rare earth atoms R are particularly promising to show long-term stability of magnetic moments when they are distributed individually at a surface [E11]. This fact is based on the threefold symmetry of the used metallic Pt(111) surface, which forbids at very low temperatures certain electronic transitions and increases the stability of the magnetic moments of the deposited Ho atoms. Although, the low temperatures and the stability of few minutes is not applicable in nowadays technologies it shows the importance of the symmetry to the strongly localized f-states. It is possible to model this influence to the magnetic properties from *ab initio*. Hereby, relativistic effects, the strong localization of the f-orbitals (see OPW method in section 3.1) and the general anisotropy term of section 3.3.3 has to be considered.

4.1. Rare earth impurities

The experimentally observed single Holmium atoms are sitting at the Pt(111) surface either in hexagonal closed packed (hcp) or in fcc position [E11]. Both positions have threefold C_{3v} symmetry (see figure 4.1). The out-of-plane distance of Ho was obtained via a structural relaxation.[1]

The information was used as input for further electronic and magnetic structure calculations, using the fully relativistic implementation of HUTSEPOT. Since conventional LDA failed to describe the strongly localized $4f$ states of Ho, the LDA+U method and the SIC were used in the calculations. The Green's function method is particularly well suited to model a single impurity at a surface with the embedded cluster method in (3.4.1). Therewith, the Green's function of a semi- infinite Pt(111) surface was computed. Then, the Green's function of a cluster around the Ho atom was obtained via a Dyson equation (3.121) in a 2D periodic structure. The size of the cluster was varied to reach a certain convergence of the total energy and magnetic spin and orbital moments. A cluster size of 201 atoms was found to be optimal.

[1]The structural relaxations were calculated by Sergey Ostanin [E11] using a projector-augmented wave pseudo-potential approach [98] implemented within the Vienna *ab initio* simulation package (VASP) [99–101].

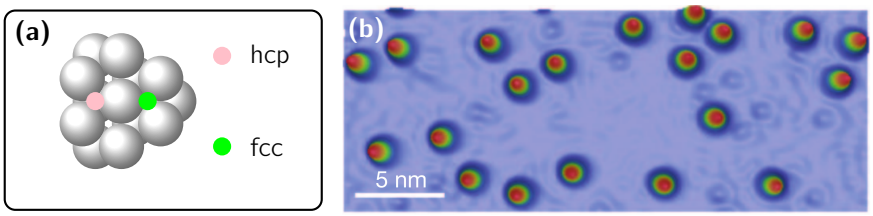

Figure 4.1: (a) Schematic picture of the surface of Pt(111). There are two possible hollow binding sites indicated (fcc or hcp) with the same threefold symmetry C_{3v}. (b) Experimental STM image of the Pt(111) surface with several holmium adatoms [E11].

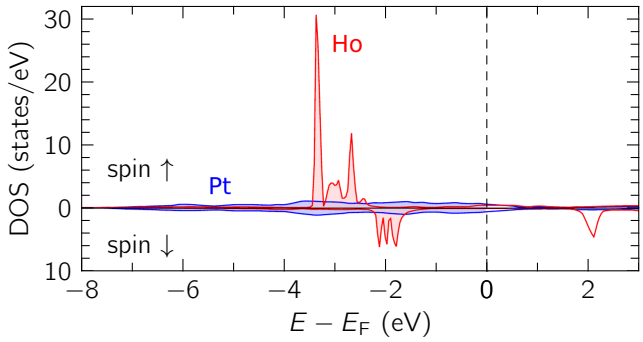

Figure 4.2: Atomic resolved density of states of the Ho atom (red) in fcc position at the Pt(111) substrate (blue).

4.2. Electronic structure

The fully relativistic calculations yield 4.1 μ_B (3.9 μ_B) and 5.6 μ_B (5.45 μ_B) for the total spin and orbital moments for a Ho atom in the fcc (hcp) hollow position. The corresponding density of states was calculated for the fcc case with 7 majority and 3 minority $4f$ electrons below the Fermi level (see figure 4.2). It indicates a total angular momentum of $J = 8$ which is in good agreement with Hund's rules. The magnetic anisotropy energy within the LDA+U approximation ($U_{\text{eff}} = 5\,\text{eV}$) was found to be 45 meV and 32 meV for the fcc and hcp hollow positions, respectively.

4.3. Crystal-field splitting of the energy spectrum

Since, the symmetry of the environment is of main importance, the crystal-field splitting of the f levels for a single Ho atom at a Pt(111) surface is discussed from the theoretical point of view [E11]. The surface is considered only in the C_{3v} symmetry.

4.3.1. Threefold crystal-field Hamiltonian

The corresponding crystal-field Hamiltonian (3.84) can be obtained by considering the symmetry of the real spherical harmonics and substituting them by the Steven's operators [102]. It reads for the threefold symmetry

$$\widehat{H}_{C_{3v}} = B_2^0\widehat{O}_2^0 + B_4^0\widehat{O}_4^0 + B_6^0\widehat{O}_6^0 + B_4^3\widehat{O}_4^3 + B_6^3\widehat{O}_6^3 + B_6^6\widehat{O}_6^6\,, \tag{4.1}$$

where the Steven's operators are

$$\widehat{O}_2^0 = 3\widehat{J}_z^2 - J(J+1)\,, \tag{4.2}$$

$$\widehat{O}_4^0 = 35\widehat{J}_z^4 - 30J(J+1)\widehat{J}_z^2 + 25\widehat{J}_z^2 - 6J(J+1) + 3J^2(J+1)^2\,, \tag{4.3}$$

$$\widehat{O}_4^3 = 1/4\Big[\widehat{J}_z(\widehat{J}_+^3 + \widehat{J}_-^3) + (\widehat{J}_+^3 + \widehat{J}_-^3)\widehat{J}_z\Big]\,, \tag{4.4}$$

$$\begin{aligned}\widehat{O}_6^0 = {} & 231\widehat{J}_z^6 - 315J(J+1)\widehat{J}_z^4 + 735\widehat{J}_z^4 + 105J^2(J+1)^2\widehat{J}_z^2 - 525J \times \\ & \times (J+1)\widehat{J}_z^2 + 294\widehat{J}_z^2 - 5J^3(J+1)^3 + 40J^2(J+1)^2 - 60J(J+1)\,,\end{aligned} \tag{4.5}$$

$$\begin{aligned}\widehat{O}_6^3 = {} & 1/4\Big[(11\widehat{J}_z^3 - 3J(J+1)\widehat{J}_z - 59\widehat{J}_z)(\widehat{J}_+^3 + \widehat{J}_-^3) + \\ & + (\widehat{J}_+^3 + \widehat{J}_-^3)(11\widehat{J}_z^3 - 3J(J+1)\widehat{J}_z - 59\widehat{J}_z)\Big]\,,\end{aligned} \tag{4.6}$$

$$\widehat{O}_6^6 = 1/2\Big[\widehat{J}_+^6 + \widehat{J}_-^6\Big]\,. \tag{4.7}$$

The anisotropy parameters in (4.1) were calculated from *ab initio* [E11]. Therefore, the charge density of the $4f$ states was determined by HUTSEPOT and plugged into (3.92) or (3.94). The different binding sites of the Ho atom, either fcc or hcp, showed only a minimal variation in the calculated anisotropy constants. Thus, the anisotropy constants are presented for the Ho atom at the fcc binding site in table 4.1. The term with B_2^0 dominated the Hamiltonian (4.1), since all other anisotropy constants, wich are relevant for (4.1), were three orders of magnitude smaller. All other anisotropy constants should be zero for symmetry reasons and were obtained accordingly in the first-principles calculation.

The anisotropy constant B_2^0 together with the Steven's operator (4.2) forms the already known uniaxial magnetic anisotropy. However, as it is shown in the following, the anisotropy constants corresponding to the operators in (4.3) to (4.7) mix the systems' eigenstates due to the ladder operators $\widehat{J}_+$ or $\widehat{J}_-$ and, thereby, have a crucial contribution to the stability of the magnetic ground states.

4.3.2. Eigenvalue problem and exact diagonalization

With the anisotropy constants B_n^m and the Steven's operators (4.2) to (4.7), the crystal-field Hamiltonian can be used in an eigenvalue problem to derive the eigenvalues E and eigenstates $|\Psi_i\rangle$

$$\widehat{H}_{C_{3v}}|\Psi_i\rangle = E|\Psi_i\rangle\,. \tag{4.8}$$

Table 4.1: Calculated anisotropy constants obtained with HUTSEPOT for a Ho atom sitting at the fcc binding site. All other anisotropy constants were zero.

CFP	value [neV]	CFP	value [neV]
B_2^0	-239×10^3	B_6^0	0.186
B_4^0	86	B_6^3	-1.967
B_4^3	293	B_6^6	0.630

In general, the eigenstates will be a linear combination of the pure states of the free atom $|JM\rangle = |M\rangle$ (for Holmium with fixed $J = 8$)

$$|\Psi_i\rangle = \sum_{M=-8}^{+8} f_M |M\rangle \,. \tag{4.9}$$

One way to solve the eigenvalue problem (4.8) is the exact diagonalization (ED). Equation (4.8) is rewritten as a matrix eigenvalue problem by using the sum (4.9). Applying $\langle M|$ from the left side yields at the left hand side the matrix elements $\langle M|\widehat{H}_{C_{3v}}|M'\rangle$ and at the right hand side the delta function

$$\sum_{M=-8}^{+8} f_M \langle M'|\widehat{H}_{C_{3v}}|M\rangle = \sum_{M=-8}^{+8} E f_M \langle M'|M\rangle \,, \tag{4.10}$$

$$= E \sum_{M=-8}^{+8} f_M \delta_{M'M} \,. \tag{4.11}$$

It leads to a linear system of equations for all states $\langle M'|$

$$\sum_{M=-8}^{+8} f_M \Big\{ \langle M'|\widehat{H}_{C_{3v}}|M\rangle - E\delta_{M'M} \Big\} = 0 \,, \tag{4.12}$$

which has only non trivial solutions if

$$\det \Big| \langle M'|\widehat{H}_{C_{3v}}|M\rangle - E\delta_{M'M} \Big| = 0 \,. \tag{4.13}$$

With the matrix $\underline{H}_{C_{3v}} = \langle M'|\widehat{H}_{C_{3v}}|M\rangle$ and the vector $\boldsymbol{f} = (f_{-8}, \ldots, f_{+8})^{\mathrm{T}}$, the equation systems is rewritten

$$\underline{H}_{C_{3v}} \boldsymbol{f} = E \boldsymbol{f} \,. \tag{4.14}$$

The matrix eigenvalue problem (4.14) was solved with *Mathematica*. Due to the only appearing powers of 3 or 6 for the operators $\widehat{J}_\pm$, all eigenstates have only non-zero f_M for $\Delta M = \pm 3$ (see tables A.1, A.2 and A.3 in the appendix showing the complete states). Therefore, three different groups of eigenstates appear starting either by $M = -8$, $M =$

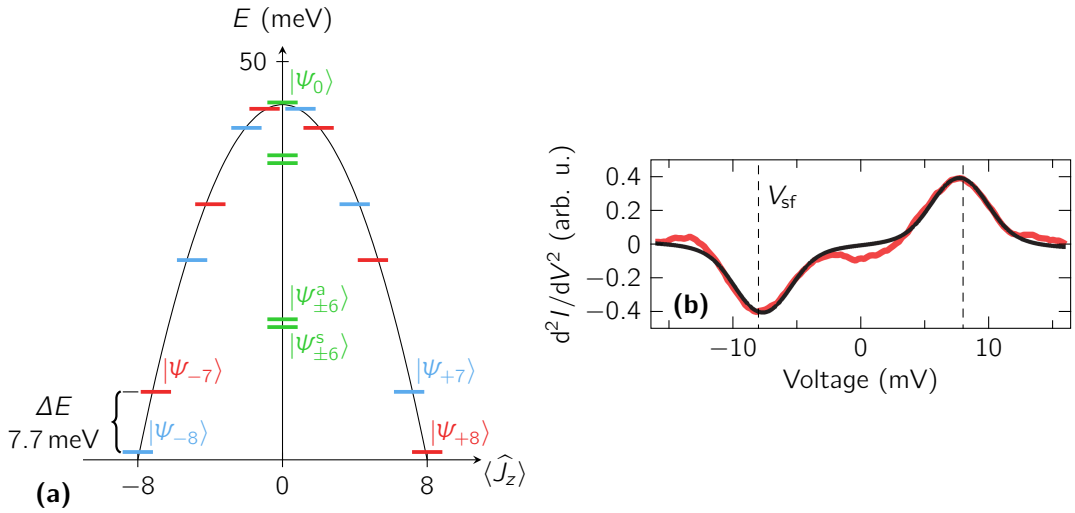

Figure 4.3: (a) Calculated energy spectrum of Ho for $\widehat{H}_{C_{3v}}$ (4.1) in dependence of the expectation value $\langle \widehat{J}_z \rangle = \langle \Psi_i | \widehat{J}_z | \Psi_i \rangle$. The energy difference from the ground states to the first excited states is shown. The three colors group the different states according to their terms, like in (4.15), (4.16), or (4.17). The black curve is only to guide the eye. (b) Experimental inelastic tunneling spectrum recorded on top of a single Ho atom in the fcc position (red) showing an inelastic excitation at $V_{sf} < 8\,\text{meV}$, as determined by a fit to the data (black). Taken from [E11].

$+8$ or having an even distribution of M values. For example,three states with nonzero f_M are

$$|\Psi_{-8}\rangle : M = -8, -5, -2, +1, +4, +7 \tag{4.15}$$
$$|\Psi_{+8}\rangle : M = -7, -4, -1, +2, +5, +8 \tag{4.16}$$
$$|\Psi_{\pm 6}\rangle : M = -6, -3, 0, +3, +6\,, \tag{4.17}$$

where the different colors correspond with the energy spectrum plotted versus the expectation value of the operator $\widehat{J}_z$ (see figure 4.3a).

As already expected from the anisotropy constants, the shape of the downwards turned parabola dominates strongly the energy spectrum (see figure 4.3a). The two ground states $|\Psi_{\pm 8}\rangle$ mainly keep the character of $|-8\rangle$ and $|+8\rangle$. The energy difference ΔE between the two ground states and the first two excited states $|\Psi_{\pm 7}\rangle$ is 7.7 meV in good agreement with the experimental observation of $\approx 8\,\text{meV}$ for a spin flip transition of a single Ho atom (see figure 4.3b). Furthermore, the two different colors of the two ground states indicate a zero overlap $\langle \Psi_{-8} | \Psi_{+8} \rangle$ and, therefore, a forbidden spin flip transition at 0 K. This relates to the long lifetime, which was observed in the low temperature STM experiments [E11].

Chapter 5.

Randomly Distributed Point Defects

This chapter is focused on the magnetic properties of oxides in respect of point defects distributed completely uncorrelated inside the samples. The final aim was the understanding of reasons for the experimentally observed strong reduction of T_t going from Sr_2FeMoO_6 (SFMO) bulk to SFMO thin films.[1] Usually, antisite disorder (ASD), oxygen vacancies (V_O) or epitaxial strain are discussed as possible reasons. The defect concentration does not exceed the low concentration limit, and it is typically in the order of several atomic percent. The CPA will be applied to model the random distribution of the point defects in the bulk materials with a concentration $c \lesssim 0.15$ (15 at. %).

The complexity of the lattice structure and the different kinds of defects was gradually raised going from a perovskite lattice structure to a double perovskite. In $SrCoO_3$ (SCO), an oxygen vacancy is the most prominent kind of defect. Their appearance alters the magnetic properties and lowers the critical temperature as measured by Balamurugan *et al.* [10]. On the contrary, the duplication of the simple cubic perovskite unit cell allows for antisite defects at the B site.

For the basic understanding of both oxide materials, the numerical calculations for each oxide were done in the corresponding experimental structure. Possible electronic correlation effects (section 3.1.4) were studied in terms of the GGA+U or SIC.

5.1. The perovskite structure

Defect-free SCO has a simple perovskite structure described by a primitive cubic cell (see figure 5.1a). Structural relaxations[2] reproduce the experimental unit cell volume of [103] (cubic phase; $a_{\text{ref}} = 3.835$ Å) with a deviation of less than 3 %. In the same order of magnitude or smaller are the differences (with respect to a_{ref}) to the single-crystal lattice constant [104] $a_{\text{sngl}} = 3.8289$ Å ($\Delta V = -0.47$ % with $V = (a_{\text{sngl}})^3$) or possible variations due to oxygen vacancies observed, e.g., $\Delta V = +2.2$ % in [10] or $\Delta V = +0.56$ % in [105] (see overview in figure 5.1b). Although the structural relaxation with GGA+U did not observe any indication of a tetragonal distortion, the a/c ratio deviated by few percent from one by applying the HSE03 exchange functional.[3] Since the experiments for stoichiometric $SrCoO_3$ did not observe a tetragonal unit cell and the electronic structure

[1] The measured films were thicker than 50 nm and, thus, are computed in a bulk structure as well. The surface effect was neglected compared to the effect of the defects.

[2] The structural relaxations were calculated by Vladislav Borisov [E4] using VASP.

[3] In the VASP calculations, the electron correlations were taken into account by GGA+U and the hybrid functional HSE03.

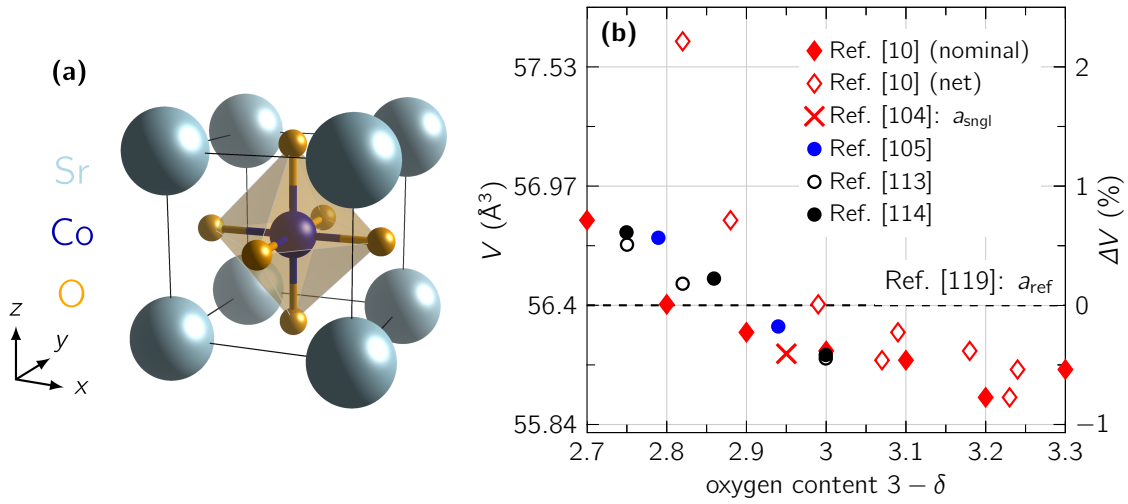

Figure 5.1: Structure of $SrCoO_3$: (a) Schematic sketch of the cubic phase [106]. (b) Experimental lattice volume as a function of oxygen concentration. The change of the volume is $\Delta V = (V - a_{ref}^3)/a_{ref}^3$ with respect to $a_{ref} = 3.835$ Å (black dashed line). The nominal and net values represent the provided and measured oxygen content [10].

did not change substantially with respect to the cubic phase, cubic SCO with the lattice constant $a_{ref} = 3.835$ Å was chosen consistently for the main study, while a hydrostatic volume variation was investigated separately in section 5.3.3 [E4].

5.2. Electronic structure of SCO

The electronic structure of the defect-free $SrCoO_3$ was investigated at first with the GF method at the experimental lattice constant. Due to the oxygen octahedron, which surrounds the Co ion, the d states of cobalt experience a crystal-field splitting of cubic symmetry, which results in three t_{2g} and two e_g degenerated states. The orbitals corresponding to the e_g states are oriented along the coordinate axes pointing to the oxygen ions and those corresponding to the t_{2g} states are pointing to the next nearest neighboring Co ions (see figure 5.1a).

The PDOS (3.23) for SCO shows an almost fully occupied majority spin channel and a pronounced peak of the Co t_{2g} spin-down states at the Fermi energy E_F (see figure 5.2). All other cobalt $3d$ states, $e_g^{\uparrow}$, $t_{2g}^{\uparrow}$ and $e_g^{\downarrow}$, are below E_F and smeared over a large energy range due to a strong hybridization with the p states of oxygen. This is in a good agreement with previous results [107] but contradicts the intermediate spin (IS state picture proposed by Potze *et al.* [108]. They state that SCO exhibits an IS state due to the competition of intra-atomic exchange and the cubic crystal-field. Thereby, some of the Co t_{2g} states would be explicitly occupied but others unoccupied with a configuration of $t_{2g}^4 e_g^1$. A more recent study identified this high spin state as d^6, but it is mixed with several other possible spin states [107].

The common way to consider the electronic correlations is to optimize the value of the repulsive U_{eff} with respect to the experimental data of structural and magnetic properties

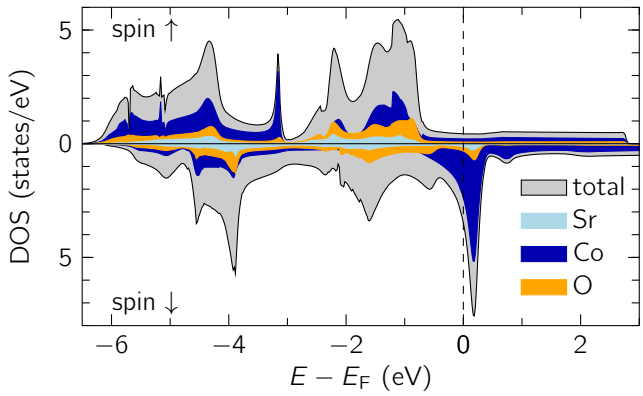

Figure 5.2: Atomic and spin-resolved density of states of $SrCoO_3$ with contributions of each species and spin-up (upper panel) and spin-down (lower panel) obtained within the GGA. The oxygen p states at all three oxygen ions in the unit cell are three fold degenerate (only one is shown).

of the system. Different values of U_{eff} were applied to the Co d state ($U_{\text{eff}}^{\text{Co}}$) in former studies ranging from 2.5 eV [109] to 8 eV [110]. The constrained random-phase approximation provided a value of $U = 10.83$ eV and $J = 0.76$ eV for the Co d states [107], which seems to be too high for a metallic system.

Since the correct value of $U_{\text{eff}}^{\text{Co}}$ is hardly to estimate from first-principles and the above reference values scatter quite a bit, the electronic structure and the occupation of the Co d states were investigated in the whole range of $U_{\text{eff}}^{\text{Co}}$ from 0 eV to 9 eV (see figure 5.3). Interestingly, for the first few steps of the calculations ($U_{\text{eff}}^{\text{Co}} \leq 1.5$ eV) the d states preserve their degeneracy in t_{2g} and e_g states. At E_F, the large peak of the Co t_{2g} states does not move due to an interplay of the Coulomb exchange and the crystal-field energy. Only for a larger $U_{\text{eff}}^{\text{Co}}$, the degeneracy is lifted. A singlet state ($d_{xy}^{\downarrow}$) becomes occupied while the doublet ($d_{zx}^{\downarrow}$ and $d_{yz}^{\downarrow}$) is pushed above E_F. On the other hand, in the spin-up channel the orbitals remain degenerated for the whole range of $U_{\text{eff}}^{\text{Co}}$ and become strongly localized (see much higher contrast for $d_{xy}^{\uparrow}$ in figure 5.3). It matches well with $t_{2g}^4 e_g^1$ and the IS state model.

A similar loss of degeneracy in the $3d$ states was also observed in calculations[2] for GGA+U and HSE03 in VASP [E4]. It has to be noted that due to the symmetric cubic structure, the particular localization of $d_{xy}^{\downarrow}$ is arbitrary and depends on the starting point of the self-consistent calculation. Another localized Co $d^{\downarrow}$ state is also possible and was observed during the calculations. However, one particular configuration (the singlet $d_{xy}^{\downarrow}$ state) is chosen for a consistent description throughout this work.

The oxygen vacancies were modeled by empty spheres which were introduces with a certain concentration at the oxygen sites within the CPA. That means that the position of the oxygen vacancies were assumed to be totally uncorrelated. Since there is no experimental evidence for an ordering of V_O for a low oxygen deficiency in $SrCoO_{3-\delta}$ up to 5 at. %, the random distribution of V_O represented a realistic model.

The electronic structure of the oxygen ions is mainly dominated by the strong hybridization with the Co d states (see figure 5.2). By including of few atomic percent of

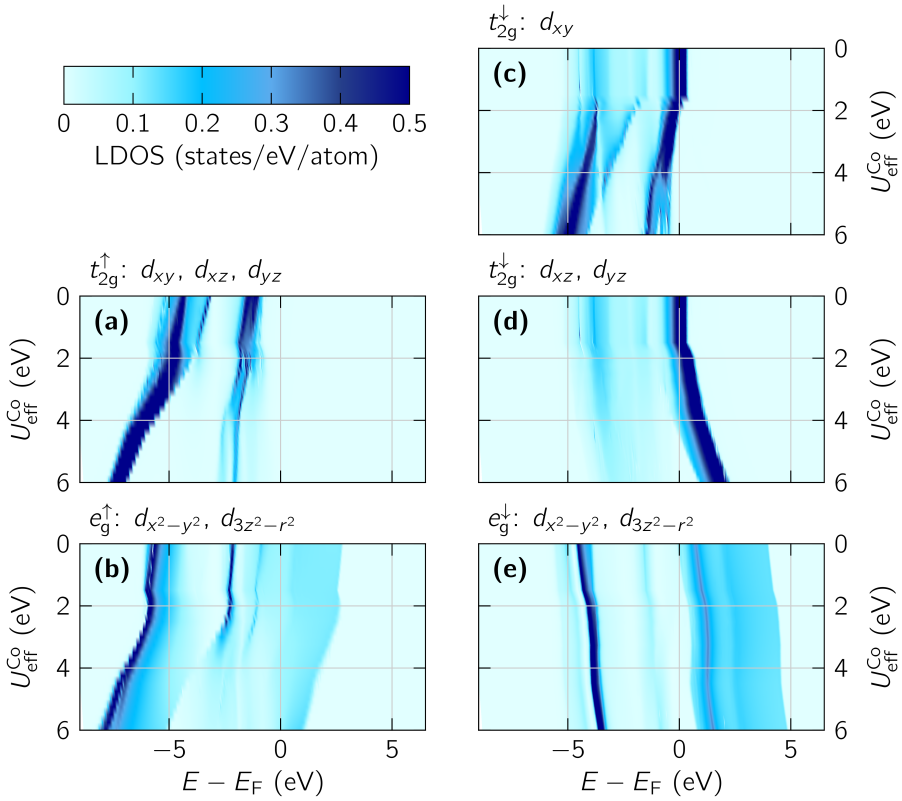

Figure 5.3: Contour plots of the LDOS in the ground state for the Co d states in dependence of the correlation parameter $U_{\mathrm{eff}}^{\mathrm{Co}}$ (ordinate). They are spin resolved (left: up, right: down) and collected according to their initial degeneracy. For higher $U_{\mathrm{eff}}^{\mathrm{Co}}$ (not shown), the energy shift continues and there are no significant changes to observe.

oxygen vacancies (5 at. %) in SCO, the unoccupied peak above E_{F} is shifted to higher energies (see figure 5.4), a similar effect as increasing $U_{\mathrm{eff}}^{\mathrm{Co}}$. Both lead to an enhancing orbital localization – either removing effectively oxygen from the lattice or reducing the electron hopping between the Co ions.

Anyway, these unoccupied oxygen states can be interpreted as the ligand hole of e_{g} symmetry, which is expected for the IS state $t_{2\mathrm{g}}^4 e_{\mathrm{g}}^1$ [108]. It is stabilized by the ligand hole state $d^6 \underline{L}_{e_{\mathrm{g}}}$ (notation from [108]), where the hole couples antiferromagnetically to another $e_{\mathrm{g}}^{\uparrow}$ in d^6: $t_{2\mathrm{g}}^4 e_{\mathrm{g}}^2$. Such a configuration was also found in our PDOS calculation with almost fully occupied orbitals for $d^{\uparrow}$ and $t_{2\mathrm{g}}^{\downarrow}$ (see figure 5.3). Although, the method is not directly comparable with the dynamic mean-field theory (DMFT) method of Kuneš *et al.* [107], the same spin configuration appeared also in their calculation with the highest multiplet weight.

5.3. Magnetic properties of SCO

The total moment of the IS state model would be theoretically $3\,\mu_{\mathrm{B}}$ ($s = 3/2$). Although the total magnetic moment of $\mu = 2.281\,\mu_{\mathrm{B}}$ calculated with the GGA functional was

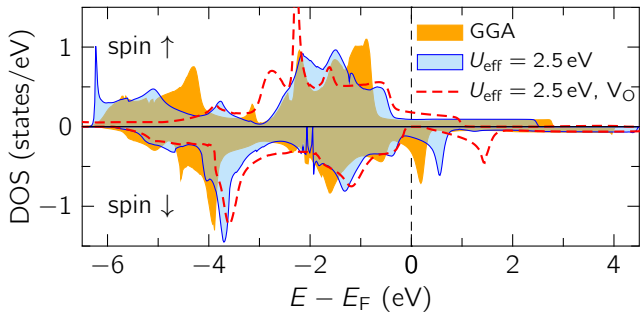

Figure 5.4: LDOS of the oxygen along the z direction (O_z) with GGA, $U_{eff}^{Co} = 2.5$ eV and 5 at. % oxygen vacancies.

smaller than in the IS state model, it agreed well with the range of the experimentally observed magnetic moments ($\mu \approx 2\,\mu_B$ to $2.5\,\mu_B$ [103, 104, 111]). The main contribution to the total moment originated correctly from the Co ions with only small induced moments of $0.15\,\mu_B$ and $0.04\,\mu_B$ at the oxygen and strontium ions, respectively. The discrepancy between the IS state model and the experiments was always attributed to possible defects. However, when the IS state model is valid, theoretical calculations of a defect-free SCO should reproduce the total magnetic moment.

Possible shortcomings might originate from the GGA electron correlation functional, which often lacks a sufficient description of localized transition metal d states. For comparison, the obtained total magnetic moment of $2.9\,\mu_B$ within VASP and the HSE03 functional agreed well with the IS state model [E4]. On the other hand, the total magnetic moment in the GF method increases monotonously with increasing U_{eff}^{Co} showing different linear slopes (see figure 5.6e). Only after the degeneracy in the Co d states for $U_{eff}^{Co} > 1.5$ eV, the total moment decreases slightly due to a reduction of the induced moments to $0.11\,\mu_B$ for the two oxygen ions (O_x and O_y), which lie in the same x-y-plane as the Co ions. In the following, the linear slope changed around $U_{eff}^{Co} \approx 2.5$ eV and $U_{eff}^{Co} \approx 4.5$ eV, which correspond to disappearing peaks in the LDOS (see figure 5.3). At the latter U_{eff}^{Co}, the total moment is $3\,\mu_B$ and matches well on the one hand side with the IS state model and on the other hand with the HSE03 calculation[2] in VASP.

5.3.1. Taking into account electronic correlation effects

In order to calculate T_t at first with the GGA functional, the magnetic exchange interactions for the nearest neighbor atoms were calculated. For RS_{FM} the magnetic interaction parameters show mainly a ferromagnetic (positive) coupling: strong between two adjacent Co ions and much weaker between the Co ions and the induced magnetic moments of the surrounding oxygen ions (see figure 5.5b). The coupling to the Sr ions was one order of magnitude smaller and was ignored in the following discussions. After the 8th shell ($d = 7.7$ Å), most of the coupling constants decay fast while other long-range interactions reflect the metallic character of $SrCoO_3$. Along the straight exchange paths (along a particular coordination axis, also marked with an asterisk in figures 5.5b and 5.5c) the coupling via the oxygen ions remains stronger. The same tendency can be observed for the coupling between the Co ions in the DLM model (J_{ij} calculated in RS_{PM}). Only the

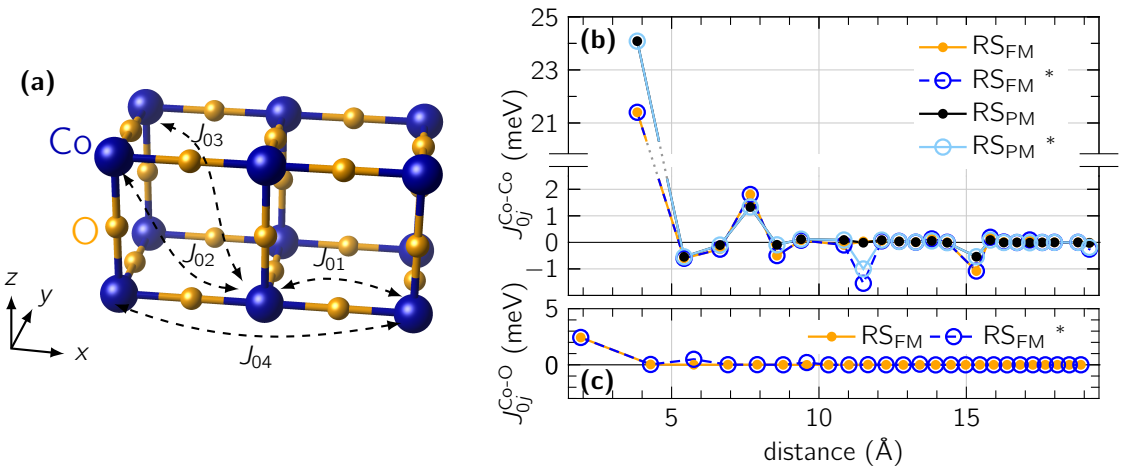

Figure 5.5: Magnetic exchange interactions J_{ij} of SCO: (a) Schematic view of the orientation of J_{ij} between Co ions only. The non magnetic Sr ions are not shown. The notation J_{01}, J_{02}, ... means nearest neighbors (NN), next NN, etc. The values for the magnetic coupling constants between Co-Co and Co-O are given in (b) and (c). Both calculated with the GGA for a FM or PM (DLM model) reference state RS$_{FM}$ and RS$_{PM}$, respectively. The asterisk marks those coupling constants which strictly follow only one direction in space, e.g., along the edge of a cube edge in (a). The abscissa in (b) is non-continuous, due to the large differences in the values.

nearest neighbor interactions became larger while the other coupling constants were reduced. At the oxygen ions, the induced magnetic moments vanished in the DLM model and no exchange interactions were found between them. In any case, all magnetic coupling constants up to a distance of 15.34 Å were taken into account for the Monte Carlo simulation. The resulting Curie temperature did not agree with the experimental results (within the DLM model $T_C^{MC} = 771$ K compared to $T_C^{exp} \approx 280$ K). The reason for this high T_C^{MC} might be an overestimation of the magnetic coupling between the Co atoms. The increase in the localization of $3d$ states by using electron correlation corrections or more advanced functionals should decrease as well the orbital overlap and thereby reduce the exchange coupling.

Such a overall reduction in the magnetic coupling parameters J_{ij} is indeed observed within the GGA+U (see figures 5.6a to 5.6d). In both reference states (RS$_{FM}$ and RS$_{PM}$), the most dominant coupling constants, $J_{01}^{Co\text{-}Co}$ and $J_{04}^{Co\text{-}Co}$, are strongly ferromagnetic. Both interactions are mediated by oxygen ions between Co ions forming either a Co-O-Co or a Co-O-Co-O-Co chain (see figure 5.5a). Those bonds connect mostly the O p states with the Co e_g states (σ bonds). This typically antiferromagnetic (AFM) superexchange is suppressed by the metallic character of $SrCoO_3$ and for small U_{eff}^{Co} an increasing band magnetism is observed in the region of degenerated Co d states. There, the coupling becomes stronger with U_{eff}^{Co} until 1.5 eV because the Co $e_g^{\uparrow}$ and $e_g^{\downarrow}$ states are either pushed below or above E_F, respectively. This increases the exchange splitting and, therefore, the magnetic coupling. In contrast, the coupling between two Co ions enclosing a 90° angle ($J_{02}^{Co\text{-}Co}$) is small and AFM, while the next coupling ($J_{03}^{Co\text{-}Co}$) is very weak compared to the other interactions.

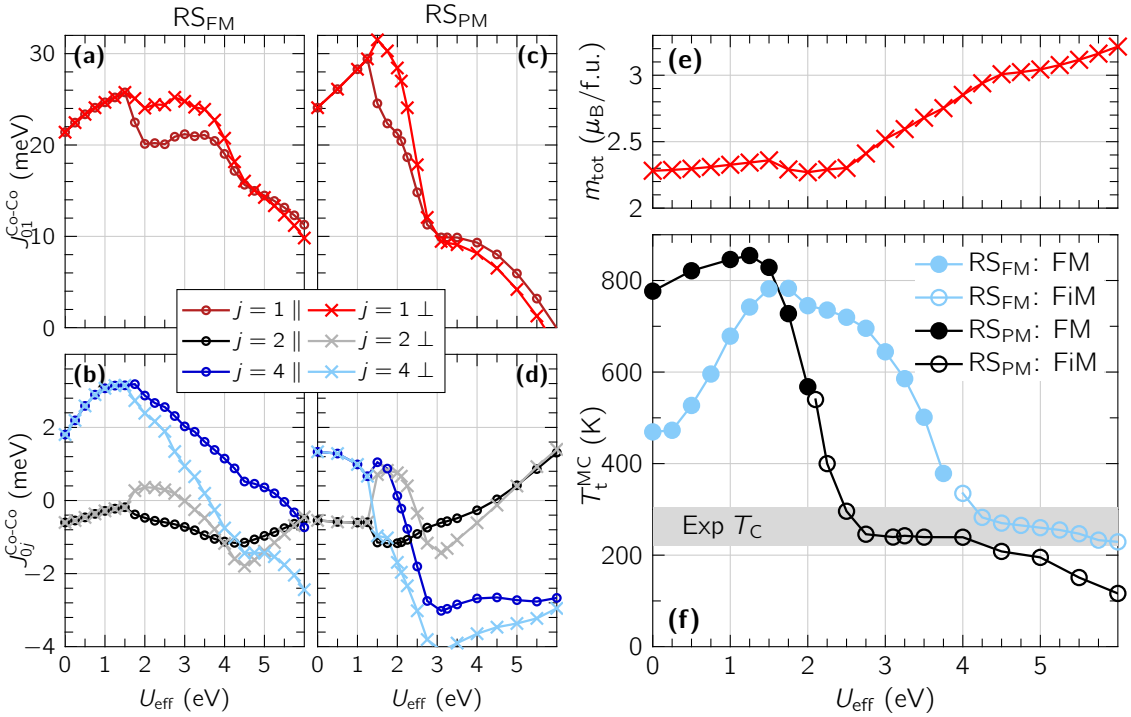

Figure 5.6: Magnetic properties of SCO as a function of $U_{\text{eff}}^{\text{Co}}$: The magnetic exchange interactions $J_{0j}^{\text{Co-Co}}$ for a ferromagnetic (a)-(b) or paramagnetic (c)-(d) reference system. They are subdivided into two groups, $\parallel$ and $\perp$, for $J_{0j}^{\text{Co-Co}}$ only in the x-y-plane and those with contributions also in x direction (directions given in figure 5.5a). The $J_{03}^{\text{Co-Co}}$ (not shown) does not split due to $U_{\text{eff}}^{\text{Co}}$ and are always small (< 0.3 meV). (e) Total magnetic moment per functional unit at the ground state. (f) Critical temperatures for the magnetic transition. The Monte Carlo calculations show a change in the magnetic ground state from clear ferromagnetic behavior to a FiM situation at $U_{\text{eff}}^{\text{Co}} \approx 2.1$ eV and 4 eV for the RS_{PM} and RS_{FM} calculations, respectively (see text). The gray shaded area indicates the experimental T_C range varying between the results for a single-crystalline sample [104] and a polycrystalline sample [10].

After that, in the symmetry broken regime, the J_{ij} reflect the change in the degeneracy of the Co d state in the LDOS. Due to the splitting of the $t_{2g}^{\downarrow}$ states into the degenerated doublet ($d_{xz}^{\downarrow}$ and $d_{yz}^{\downarrow}$) and a singlet ($d_{xy}^{\downarrow}$), the J_{ij} with either ($\parallel$) in x and y direction or ($\perp$) in z direction were different for $U_{\text{eff}}^{\text{Co}} > 1.5$ eV. The competing superexchange overcomes the band magnetism while the localization of the d states is increasing (see stronger contrast in figure 5.3). This reduces, in general, the overlap of the orbitals and the magnetic exchange interactions. It is visible e.g. for J_{01} and J_{04} in figures 5.6a to 5.6d but also for other J_{0j} (not shown). On the other hand, the modifications in the coupling constants are much more complex due to the changing LDOS. However, some simple tendencies can be observed, e.g. due to the localization of the Co d_{xy} states, the magnetic coupling for $U_{\text{eff}}^{\text{Co}} < 4$ eV in the x-y-plane ($\parallel$ contributions in J_{01}) becomes smaller than the out-of-plane ($\perp$) contributions. The $\perp$ parts of $J_{02}^{\text{Co-Co}}$ even change their character from AFM to FM.

Another significant change for all coupling constants is visible at $U_{\text{eff}}^{\text{Co}} = 4.5\,\text{eV}$ and might be correlated with vanished states in the d_{xy} LDOS indicated by a loss of contrast (see figure 5.3). At the end of the shown range, the strength of the nearest neighbor magnetic exchange coupling was only half of its starting value. It reduces further, for even higher $U_{\text{eff}}^{\text{Co}}$ (not shown) and leads to an undesired antiferromagnetic ground state.

The overall tendencies for the RS_{FM} calculations were in general also observed in the DLM picture (RS_{PM}), although the changes were much stronger, e.g. at $U_{\text{eff}}^{\text{Co}} = 6\,\text{eV}$ the J_{01} were reduced to zero and J_{04} is strongly AFM. Furthermore, the loss of degeneracy was visible already for smaller $U_{\text{eff}}^{\text{Co}}$ (see figure 5.6c). Both changes are explained by the larger extent of the Co d orbitals due to the random distribution of the magnetic moments in the DLM theory as already stated in section 3.4.3. The increasing orbital overlap enhances, on the one hand the AFM superexchange and on the other hand, alters the competition between the crystal-field and Coulomb energy, which restored the degeneracy for small $U_{\text{eff}}^{\text{Co}}$.

These magnetic exchange parameters were applied to the Monte Carlo simulation, where the resulting critical temperatures in general follow a similar tendency as the nearest neighbor coupling constant $J_{01}^{\text{Co-Co}}$ (see figure 5.6f). They show for both sets of magnetic coupling parameters a linear increase up to $U_{\text{eff}}^{\text{Co}} = 1.5\,\text{eV}$. The critical temperatures obtained with the $J_{0j}(\text{RS}_{\text{FM}})$ remained around 750 K with increasing $U_{\text{eff}}^{\text{Co}}$ up to $\approx 3\,\text{eV}$, and drop down sharply in the following while the DLM results decrease linearly immediately above 1.5 eV. So, $T_{\text{t}}^{\text{MC}}(U_{\text{eff}}^{\text{Co}})$ calculated for RS_{PM} reaches the experimentally relevant range already for a smaller $U_{\text{eff}}^{\text{Co}} = 2.5\,\text{eV}$ than for RS_{FM} (4.5 eV). A reason for the smaller $U_{\text{eff}}^{\text{Co}}$ was already discussed above for the J_{ij} – the larger overlap of the orbitals in the more realistic DLM model. Additionally, the RS_{PM} calculation showed after the kink an almost constant $T_{\text{t}}^{\text{MC}}(U_{\text{eff}}^{\text{Co}}) = 240\,\text{K}$ for a larger range of $U_{\text{eff}}^{\text{Co}}$ parameters (2.75 eV to 4 eV). On the other side, the ground state calculation at RS_{FM} with the GF method (GGA+U) returns for $U_{\text{eff}}^{\text{Co}} \approx 5\,\text{eV}$ a T_{t}^{MC} inside the experimental range. This observation matches well with the comparison of the electronic structure and the magnetic moments between the GF method (GGA+U) and VASP (HSE03) calculations at $U_{\text{eff}}^{\text{Co}} \approx 5\,\text{eV}$ [E4].

Furthermore, figure 5.6f accounts for the magnetic ground state observed in the Monte Carlo study with different symbols, having either a FM or FiM ground state. The DLM theory predicted only a FiM ordered ground state for the range of T_{t}^{MC} ($U_{\text{eff}}^{\text{Co}} \approx 2.5\,\text{eV}$) equivalent to experimental results. This is, however, still physically reasonable. While at the critical temperature the induced moments at oxygen might be zero, they will appear at lower temperatures. This leads to a ferromagnetic ground state obtained with the $J_{ij}(\text{RS}_{\text{FM}})$ for even larger $U_{\text{eff}}^{\text{Co}}$ (see blue curve in figure 5.6f).

5.3.2. Effects of oxygen vacancies

The variation of the magnetic transition temperature of $\text{SrCoO}_{3-\delta}$ was reconsidered regarding the oxygen content, $T_{\text{t}} = T_{\text{t}}(\delta)$. In the experimental study [10], the oxygen content in the samples varied with respect to the stoichiometric SCO between ± 6 at. %, having either oxygen deficiency or excess oxygen. This increase in the oxygen content enhanced T_{C} (see figure 5.7a) [10]. However, the following theoretical study was restricted to the regime of oxygen deficiency. The inclusion of excess oxygen was beyond the scope

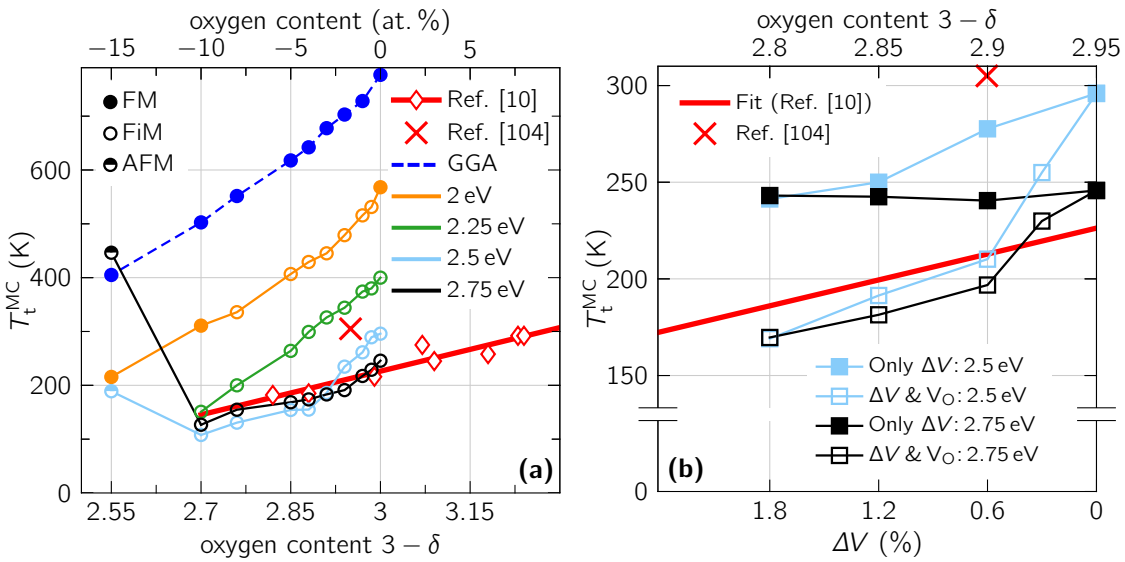

Figure 5.7: Critical temperature of $SrCoO_{3-\delta}$ obtained in the DLM model as a function of the oxygen content δ and compared with experimental references: (a) The GGA calculations shown as blue dashed line and GGA+U calculations shown as differently solid colored lines. The open and full circles in the corresponding colors indicate the calculated data points and the magnetic ground state as shown in figure 5.6f. An additional antiferromagnetic state (AFM) is marked with a half filled circle (see text). (b) The varying oxygen content δ corresponds as well to a volume change ΔV (see figure 5.1b). It is considered separately in filled squares (lower axis; reversed to match (a)) or together with δ in open squares (upper axis). $U_{\text{eff}}^{\text{Co}}$ is 2.5 eV (blue) or 2.75 eV (black), respectively. The magnetic ground state is always FiM.

of this thesis, since the additional oxygen atoms might, e.g., occupy unknown interstitial sites, whereas the oxygen vacancies occupy very likely the lattice sites in the perovskite structure and could be included within the CPA.

Also from the theoretical point of view, a reduction of $T_t^{\text{MC}}(\delta)$ with increasing δ (reduction in the amount of oxygen), since the localization of the orbitals through oxygen vacancies was alike applying an $U_{\text{eff}}^{\text{Co}}$ parameter. Therefore, the magnetic interactions in the Co-O-Co bonds were weakened as well. This expectation was generally fulfilled for the calculated $T_t^{\text{MC}}(\delta)$ at different $U_{\text{eff}}^{\text{Co}}$: the GGA exchange functional alone, $U_{\text{eff}}^{\text{Co}} = 2$ eV, 2.25 eV, 2.5 eV or 2.75 eV (see figure 5.7a). They all show an increase of the critical temperatures by increasing the oxygen content from $\delta = 0.3$ (10 at. %) towards stoichiometric SCO while their slopes vary qualitatively between $U_{\text{eff}}^{\text{Co}} = 2.25$ eV and 2.5 eV. The slope of $T_t^{\text{MC}}(\delta)$ remained equal until $U_{\text{eff}}^{\text{Co}} = 2.25$ eV and even partially for 2.5 eV but became reduced for larger $U_{\text{eff}}^{\text{Co}}$ and matched the tendency of the experimental results. For $U_{\text{eff}}^{\text{Co}} = 2.5$ eV, only the combined effect of $U_{\text{eff}}^{\text{Co}}$ and a larger amount of V_O was enough to obtain the experimental tendency, whereas the value $U_{\text{eff}}^{\text{Co}} = 2.75$ eV lays in the region of constant $T_t^{\text{MC}}(U_{\text{eff}}^{\text{Co}})$ (see figure 5.6b). For the latter, alone the influence of the oxygen vacancies on $T_t^{\text{MC}}(\delta)$ was visible and it agreed well with the measurements.

However, these findings were just valid in a small range of oxygen deficiency, otherwise $SrCoO_{3-\delta}$ became unstable and forms different structures [20, 112, 113]. At 15 at. % oxygen deficiency and $U_{\text{eff}}^{\text{Co}} \geq 2.5\,\text{eV}$, the resulting magnetic ground state was antiferromagnetic. This chemical composition is already close to the ordered brownmillerite structure $SrCoO_{2.5}$, which is antiferromagnetic with a high Néel temperature of $T_{\text{N}} = 570\,\text{K}$ [111]. Although the cubic structure is not the appropriate equilibrium structure at this oxygen concentration, the difference in chemical composition might lead already to an AFM order with a higher critical temperature. The transition from the FM to an AFM ground state was already visible in the dependence of $U_{\text{eff}}^{\text{Co}}$ (see figure 5.6), where large values of $U_{\text{eff}}^{\text{Co}}$ result in AFM magnetic coupling constants. Interestingly, Lee and Rabe applied theoretically strain to SCO by varying the unit cell volume and found as well a transition from FM to AFM [109]. Thus, strain or hydrostatic pressure might modify the magnetic coupling as well.

5.3.3. Hydrostatic volume changes

Up to now all calculations were performed with the fixed lattice constant a_{ref}, but measured lattice constants indicate a volume expansion in consequence of oxygen deficiency (see examples in figure 5.1b). To estimate the influence of this volume enhancement to the critical temperature $T_{\text{t}}^{\text{MC}}(\Delta V)$, the largest volume expansion in figure 5.1b was chosen as reference [10]. Therefore, the lattice parameters of the cubic unit cell for defect-free SCO was scaled up to 1.8 %. T_{t}^{MC} was calculated at RS_{PM} (see filled squares and the lower axis in figure 5.7b). For $U_{\text{eff}}^{\text{Co}} = 2.5\,\text{eV}$, the increasing distance between the Co atoms reduces their magnetic interaction and the critical temperature, again similar as $U_{\text{eff}}^{\text{Co}}$ or V_{O}. Hence, $T_{\text{t}}^{\text{MC}}(\Delta V)$ remains for $U_{\text{eff}}^{\text{Co}} = 2.75\,\text{eV}$ almost constant.

On the other hand, the volume expansion is correlated to a particular oxygen content. For simplicity, it is linearly interpolated from [10] to derive in figure 5.7b the upper axis (open squares). The combination of volume expansion and oxygen deficiency leads for $U_{\text{eff}}^{\text{Co}} = 2.5\,\text{eV}$ to a similar quantitative curve as for $T_{\text{t}}^{\text{MC}}(\delta)$ but the observed kink appears already for $\delta = 0.05$ or $\Delta V = 0.6\,\%$, respectively. In contrast, the qualitative and quantitative agreement of the variation of T_{t}^{MC} for $U_{\text{eff}}^{\text{Co}} = 2.75\,\text{eV}$ is still in place.

Although the good agreement with [10] of the theoretically obtained T_{t}^{MC}, it has to be remarked that the volume variation ΔV was the upper boundary in figure 5.1b. For example, in [113] the oxygen deficiency of $\delta = 0.16$ with respect to their value at $\delta = 0$ is correlated to a much smaller volume expansion of $\Delta V = 0.6\,\%$. As a result the slope of $T_{\text{t}}^{\text{MC}}(\delta)$ changes drastically as well.

Conclusions The PM model (DLM theory) could be successfully applied to the Co ions in SCO and yielded for small correlation parameters in the range of $U_{\text{eff}}^{\text{Co}} = 2.50\,\text{eV}$ to 2.75 eV for the critical temperature a good qualitative agreement [E4] with the single-crystal measurements [104]. When compared to lower polycrystalline experimental values [10], T_{t} is independent of $U_{\text{eff}}^{\text{Co}}$ up to 4 eV. In this range, the inclusion of oxygen defects with the effective picture of the CPA explains very well the experimental reduction of $T_{\text{t}}(\delta)$ in polycrystalline $SrCoO_{3-\delta}$.

5.4. Lattice Structure of the double perovskite SFMO

Considering the excellent agreement of the calculations with the GF method compared with the experimental findings for the simple perovskite structure in SCO, another level of disorder was reached by redoubling the perovskite cell. The resulting double perovskite $Sr_2BB'O_6$ exhibits an additional degree of freedom for the occupation of the B site. A variation at B site allows for the so-called antisite disorder (ASD).

Again the experimentally found lattice structure was adopted for the calculations on SFMO. The oxygen atoms provide an octahedral environment around the Fe and Mo sites. The FeO_6 and MoO_6 octahedra alternate along the three cubic axes, while the Sr atoms occupy the hollow sites formed in between the FeO_6 and MoO_6 octahedra at the body-centered positions (see figure 5.8).

SFMO was found to be cubic ($Fm\bar{3}m$) in the paramagnetic phase, but changes into a tetragonal-type structure below a critical temperature [115, 116]. A representative choice of experimentally observed lattice constants is collected in table 5.1. Their variation between the smallest and largest value is quite small (0.25 % and 0.17 % for a and c, respectively) and the cubic symmetry would be represented by a c/a ratio of $\sqrt{2}$. So, the deviation from the cubic symmetry is small as well.

In general, the Sr atoms occupy the $4d$ Wyckoff positions $(0, 1/2, 1/4)$. Depending on the reference, the Fe atoms occupy the $2a$ Wyckoff pos. $(0, 0, 0)$ and Mo the $4d$ Wyckoff pos. $(0, 0, 1/2)$, or vice versa. The positions of the oxygen atoms are not definite. These vary between different studies (see table 5.1), either exactly between Mo and Fe, which gives the body centered tetragonal structure type ($I4/mmm$; No. 139) [117, 119] or the

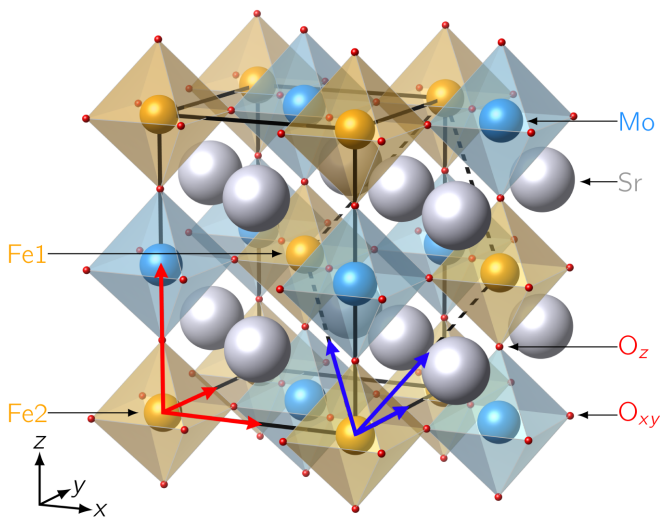

Figure 5.8: The double perovskite structure of SFMO. The colored polyhedra [106] visualize the octahedral surroundings of the Fe and Mo atoms (orange and blue). Following from the tetragonal symmetry, two different oxygen positions appear (marked with O_{xy} and O_z). The black dashed lines and the blue arrows indicate the primitive unit cell used in this thesis. For comparison, the tetragonal cell is shown by the black solid lines and the red arrows. It contains two functional units with two Fe sites (Fe1, Fe2).

Table 5.1: Variation of the experimental lattice constants and oxygen positions of SFMO from several references. Fe occupies consistently (0, 0, 0). The Wyckoff positions of the oxygen atoms are (0, 0, z) and (x, y, 0). The positions of the other atoms are described in the text.

a (Å)	c (Å)	$c/a/\sqrt{2}$	x	y	z	Ref.
5.5729	7.9077	1.003 353	0.248	$= x$	0.235	[117, 118]
5.573	7.902	1.002 612	0.2464	$= x$	$= x$	[119]
5.5752	7.892 51	1.001 009	0.2610	0.2333	0.2474	[120]
5.587	7.894	0.999 087	0.248	$= x$	0.235	[121]

oxygen octahedra are slightly distorted ($I4/m$, No. 87) [120, 122]. In any case there are two types of oxygen atoms with O_z at the 4e Wyckoff pos. (0, 0, z) and O_{xy} at the 8h Wyckoff pos. (x, y, 0) while the Fe atom position is (0, 0, 0) (see figure 5.8).

Since the changes of the lattice constants are small, the more symmetric body centered tetragonal structure type and the lattice constant from [119] were used for simplicity as input for the calculations. The primitive unit cell with one functional unit of SFMO was considered throughout the following sections (see blue arrows in figure 5.8).

The lattice structure was kept static in order to deal with chemical disorder within the CPA. The ASD was modeled by interchanging randomly Fe and Mo [E2], although some experimental studies report no random distribution but segregation into small clusters and formation of antiphase boundaries [123]. However, at the low concentration limit the CPA is appropriate to reproduce well the electronic structure of both randomly distributed and clustered disorder. Advanced schemes, which go beyond the single-site approximation of the CPA need still high computational resources for larger unit cells and are beyond the scope of this investigation. For the oxygen vacancies, a certain percentage of empty spheres were introduced at the lattice sites of the oxygen ions. The typical oxygen deficiency δ ranges between 0.006 to 0.36 [124–126]. This represents 0.1 at. % to 6 at. % of the total oxygen amount in stoichiometric SFMO.

5.5. Half-metallic SFMO

By using at first the experimental structure of SFMO [119] in the self-consistent calculations, the electronic structure was investigated. SFMO exhibits a half-metallic character, so all electronic states at the Fermi energy have only one spin orientation while the spin channel exhibited a band gap [E2]. Although the half-metallic solution was obtained previously with different calculation techniques [127, 128], the Green's function method ran into a metallic solution with a nonzero density of states in both spin channels at E_F (see figures 5.9a and 5.9c). Only the relevant states lying close to the Fermi energy, namely the Fe and Mo staes, are plotted. Due to a slight tetragonal distortion in SFMO, the t_{2g} and e_g splitting of the transition metal d states in the cubic crystal-field observed for SCO before changed with respect to the new D_{4d} point symmetry. The crystal-field splits the Fe (Mo) 3d (4d) orbitals into three singlets A_{1g} ($d_{3z^2-r^2}$), B_{1g} ($d_{x^2-y^2}$), and B_{2g} (d_{xy}) and a doublet e_g (d_{yz} and d_{xz}). However, the states d_{xy} and $d_{3z^2-r^2}$, as well as the states $d_{x^2-y^2}$, d_{yz} and d_{xz},

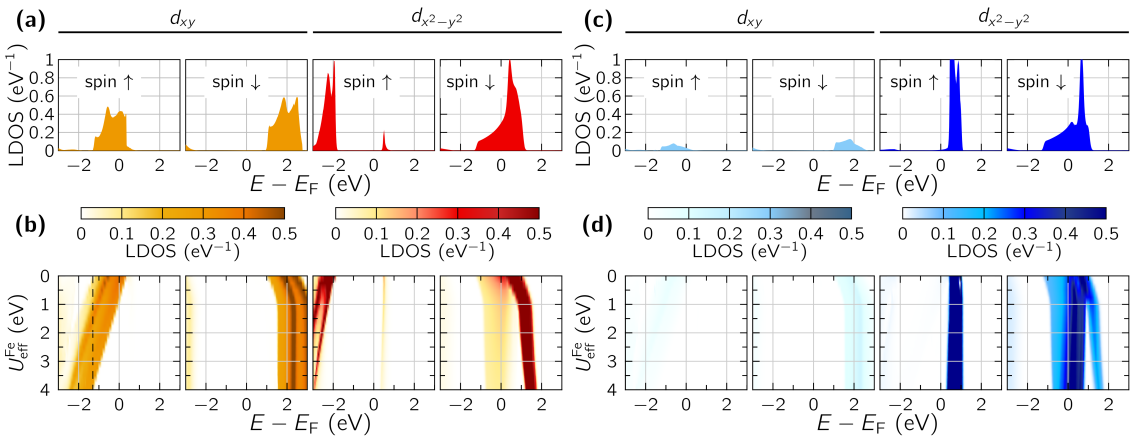

Figure 5.9: LDOS of the transition metal ions in SFMO close to the Fermi energy: (a) GGA calculation for Fe. (b) Color-coded contour plot for Fe in dependence on the correlation correction parameter applied on the Fe d states ($U_{\text{eff}}^{\text{Fe}}$). (c)-(d) correspond to (a)-(b) but for Mo (still with $U_{\text{eff}}^{\text{Fe}}$). The lighter and darker shades (redish–Fe and bluish–Mo) represent similar groups of the symmetry split states d_{xy} and $d_{x^2-y^2}$, respectively (see text). The dashed line in (c) indicates the peak position in the experimental PES [129].

form two groups of states, which showed each a quite similar DOS, because the deviation from the ideal c/a ratio was only very low. In the following, only one representative state for each of them (d_{xy} and $d_{x^2-y^2}$, respectively) was discussed.

As already discussed in previous publications, the band gap in the majority spin channel may open when correlation corrections are applied (GGA+U or SIC) [17, 55] The experimental values for this band gap range from 0.5 eV [129] to 1.3 eV [13]. Both values are much smaller than the theoretical band gap in the majority spin channel obtained with SIC [129]. A continuously increasing electron correlation parameter applied to Fe d states $U_{\text{eff}}^{\text{Fe}}$ allowed to trace the development and the variation of the band gap (see figures 5.9b and 5.9d). The main changes at the Fermi energy appear in the spin up channel of the Fe d_{xy} states and those of similar symmetry ($d_{3z^2-r^2}$, not shown). They are pushed towards lower energies while all other states in the spin up channel are not crossing E_F. This behavior results in a band gap in the majority spin channel at $U_{\text{eff}}^{\text{Fe}} \gtrapprox 1$ eV. On the contrary, the minority spin channel at E_F remains always occupied by the $d_{x^2-y^2}$ states of Fe and Mo and those of similar symmetry (d_{yz} and d_{xz}, not shown), leading to the half-metallic character of SFMO.

The LDOS reveals in addition the formal valence states of Fe^{3+} and Mo^{5+}. Iron provides two 4s electrons and one from the $3d^{\downarrow}$ states, since all $d^{\downarrow}$ states of Fe become unoccupied (see figure 5.9b). For Mo, almost all states are unoccupied, except the delocalized d states. This situation was found in all self-consistent solutions with GGA+U.

In order to determine an appropriate $U_{\text{eff}}^{\text{Fe}}$ value, the experimental and theoretical band gap in the majority spin channel should match. The measurement of the valence PES by Saitoh *et al.* [129] allowed the comparison with the calculated DOS (see figure 5.10). The size of the band gap is determined from the different positions of the states involved in the electron transition with the lowest energy. Those states were assumed to be the $d_{xy}^{\uparrow}$

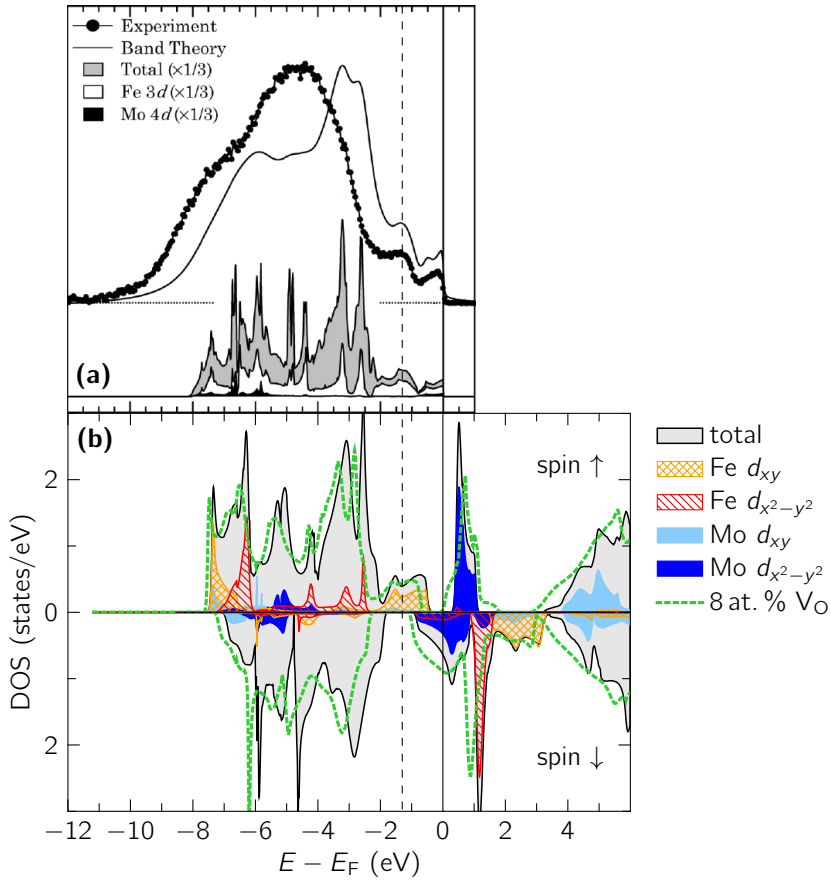

Figure 5.10: Valence spectra (DOS) of SFMO: (a) Experimental and simulated PES from the study of Saitoh *et al.* [129] (copied from Fig. 5(a) in [129], non-relevant labels were removed). (b) Calculated DOS for SFMO with $U_{\text{eff}}^{\text{Fe}} = 2\,\text{eV}$. For defect-free SFMO, the total DOS is gray and the LDOS for the d states of Fe (reddish) and Mo (bluish). The green dotted DOS includes 8 at. % of randomly distributed oxygen vacancies. Both plots (a) and (b) are scaled with respect to the same energy scale and the Fermi energy at zero (black vertical line). The dashed line indicates the position of the Fe $d_{xy}^{\uparrow}$ and $d_{3z^2-1}^{\uparrow}$ in the experimental PES.

and $d_{3z^2-1}^{\uparrow}$. The energy difference was roughly 1.3 eV (see dashed lines in figures 5.9b or 5.10). On the other hand, the measurement of Tomioka *et al.* [13] showed only a small optical gap of 0.5 eV, which was attributed to a transition from the Fe $d_{xy}^{\uparrow}$ and $d_{3z^2-1}^{\uparrow}$ to the Mo $d_{x^2-y^2}$, d_{yz} and d_{xz} states. Such a small experimental gap restricts $U_{\text{eff}}^{\text{Fe}}$ to a range of 1 eV to 2 eV (see figure 5.9b). On top of that, the peaks in the measured spectra extent over more than 1 eV and might be altered as well by additional defects, which could be only scarcely considered in the experimental comparisons. Saitoh *et al.* [129] noticed e.g. in their measured samples the occurrence of up to 10 at. % ASD, but did not account for any kind of defects in their theoretical interpretation.

Therefore, the antisite disorder was considered in the DOS calculations as well using the CPA. Few atomic percent of Mo ions at the Fe site led to Mo $d^{\uparrow}$ states at the Fermi energy (not shown). The portion of these states increases with increasing the ASD and

the spin polarization of half-metallic SFMO is reduced [130]. On the other hand, oxygen vacancies are also very likely in this system. The direct influence of oxygen vacancies to the DOS was already discussed in a supercell approach by Muñoz-García *et al.* [17]. For a single oxygen vacancy, the Fe d states showed an increase in the spin down channel below the Fermi energy, which indicated a higher occupation of the Fe ion and the valency change. By including exemplarily 8 at. % oxygen vacancies within the CPA ($U_{\text{eff}}^{\text{Fe}} = 2\,\text{eV}$), the contribution in the spin down channel right below the Fermi energy is increased similar to [17] (green dashed line in figure 5.10). This might also indicate the valency change as discussed above. The $d^{\uparrow}$ states are shifted to lower energies and the vacancies show a similar effect as the correlation corrections $U_{\text{eff}}^{\text{Fe}}$ (see figure 5.9b). The missing oxygen orbitals increase the localization of the transition metal ions. On the other hand, the averaging of the CPA leads to a general broadening of the states. Both effects compete with each other for the band gap opening, while $U_{\text{eff}}^{\text{Fe}}$ or the oxygen deficiency δ vary, respectively. If the band gap due to $U_{\text{eff}}^{\text{Fe}}$ is not large enough, the broadening closes the gap again and the spin polarization of the system is reduced as well.

Taken as a whole, a direct comparison between the theoretical and the experimental band gap is complicated when considering all the various influences of electron correlations or possible defects. In order to have a point of reference for later discussions, $U_{\text{eff}}^{\text{Fe}} = 2\,\text{eV}$ might be a suitable compromise (see figure 5.10). This $U_{\text{eff}}^{\text{Fe}}$ in consistently used in the following discussions.

5.6. Magnetic properties of SFMO

The observed transition from a metallic to a half-metallic state influences as well the magnetic properties, looking in particular on the magnetic moments, the magnetic exchange coupling, and the Curie temperature of SFMO in dependence of the electron correlations and defect concentration [E2].

5.6.1. Magnetic moments

At first, the local magnetic moments of Fe and Mo were calculated. Their antiparallel alignment (ferrimagnetism) was found as expected as the ground state in all calculations (see table 5.2). The metallic solution (weak electron correlation regime – GGA only) provided for Fe a lower magnetic moment than earlier calculations, while the calculated moment of the Mo ion was larger [127, 131–134]. As soon as SFMO turned half-metallic ($U_{\text{eff}}^{\text{Fe}} > 1\,\text{eV}$), the Fe moment became $\approx 4\,\mu_{\text{B}}$. It remained afterwards quite stable and insensitive to the strength of the electron correlations (see figure 5.11 at $x = \delta = 0$).

The Fe moment of $4\,\mu_{\text{B}}$ corresponds to the theoretical ideal value for the Fe^{3+}/Mo^{5+} or Fe^{2+}/Mo^{6+} valency configuration and is in a good agreement with the experimental neutron diffraction measurements [137], although this result is quite exceptional compared to other measurements (see table 5.2). There, the reduction in the moments with respect to $4\,\mu_{\text{B}}$ was attributed to antisite disorder [124, 135, 138]. Within the CPA, the introduced Fe ions at the Mo sites became strongly antiferromagnetically coupled to the intrinsic Fe ions and oriented their moments antiparallel. Independent of the strength of the electron correlations, the total magnetic moment of SFMO is indeed reduced linearly for ASD up

Table 5.2: The calculated magnetic moments (in μ_B) of the Fe or Mo ions in defect-free SFMO compared with reference values.

method	magnetic moment Fe	magnetic moment Mo
GGA[a]	3.090	−0.555
GGA+U[a]	3.921	−0.525
FPLMTO [134][b]	3.72	−0.29
Plane-wave method [132][b]	3.97	−0.39
XMCD [135][c]	3.05 ± 0.20	−0.32 ± 0.05
XMCD [136][c]	2.80 ± 0.30	−0.36 ± 0.03
Neutron diffraction [137][c]	4.1 ± 0.1	0.0 ± 0.1

[a]This work.
[b]Theory.
[c]Experiment with measuring uncertainty.

to 15 at. % (see figure 5.11a). The slope of this reduction is in good agreement with the estimations by previous Monte Carlo simulations [138] and experiments [139].

On the other hand, oxygen vacancies reduce also the total magnetic moment as seen in the measurements by Kircheisen *et al.* [124]. The theoretical results within the CPA, depending on the strength of the electron correlations, show as well a reduction of the total magnetic moments when the oxygen content is decreased (see figure 5.11b). Above $U_{\text{eff}}^{\text{Fe}} = 1\,\text{eV}$, the slope of the reduction is linear and remains independent of the strength of $U_{\text{eff}}^{\text{Fe}}$. We note the change of the slope for $U_{\text{eff}}^{\text{Fe}} = 0.75\,\text{eV}$. As observed for the DOS, the randomly distributed oxygen vacancies act similar as the correlation parameter $U_{\text{eff}}^{\text{Fe}}$, since they both reduce the screening of the Coulomb interaction. After few atomic percent of oxygen vacancies the slope of the magnetic moment changes is similar as for higher $U_{\text{eff}}^{\text{Fe}}$. This slope agrees qualitatively very well with the experimental results but the absolute magnetic moments are higher. The overall reduction might result from additional ASD.

5.6.2. Magnetic exchange interactions and Curie temperatures

In contrast to the magnetic moment, the calculated magnetic exchange parameters between the magnetic atoms and the critical temperatures are more sensitive to changes in the DOS. The most prominent coupling constants of the order of several meV have only a very restricted range up to 7.9 Å, which include only the interactions up to the next nearest neighbor Fe ions $J_{02}^{\text{Fe-Fe}}$ (sketched in figure 5.12c). As it is shown below, only these magnetic couplings dominate the magnetic behavior with respect to the electron correlations. The more distant exchange constants (up to 12.49 Å) were one order of magnitude smaller and became even more reduced with increasing $U_{\text{eff}}^{\text{Fe}}$. All the others could be considered to be zero. Due to the tetragonal structure, all magnetic exchange interactions

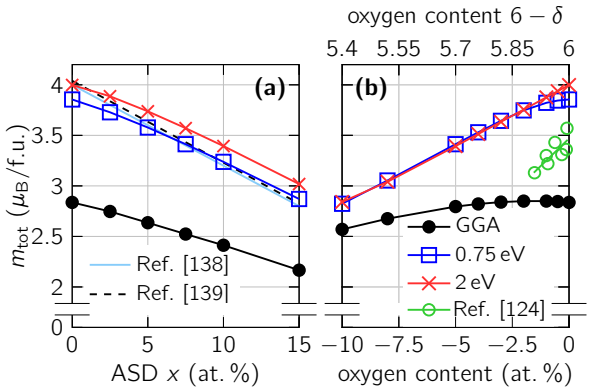

Figure 5.11: Total magnetic moment m_{tot} obtained for GGA and varying U_{eff}^{Fe} in dependence on the defect concentration: (a) ASD. (b) Oxygen deficiency δ. The oxygen amount is also given in absolute values (scale above). The theoretical results are compared to previous references. The experimental results [124] (green circles) are plotted together with a linear regression (green solid line).

show a small asymmetry with respect to those with a component in z direction. For clarity, only the coupling constants in the x-y-plane are shown.

As before for SCO, two different calculation schemes were considered:

(i) On the one hand side, the calculations of J_{ij} are performed at the ferromagnetic ground state (RS_{FM}, red and blue in figure 5.12a). There appears a strong antiferromagnetic coupling between the Fe and Mo ions, whose size becomes only slightly reduced around $U_{eff}^{Fe} \approx 1$ eV. The AFM behavior was also expected from former studies [17]. The closest Fe–Fe magnetic coupling parameter $J_{01}^{Fe\text{-}Fe}$ decreased linearly with increasing U_{eff}^{Fe} from 4 meV to 1 meV. This reduction might be correlated to the linear changes in the $d_{xy}^{\uparrow}$ and $d_{x^2-y^2}^{\uparrow}$ states. It is typical behavior within the application of an U parameter: The localization of an orbital leads to a decrease of orbital overlap and, thereby, to a decrease in the magnetic coupling strength. In contrast, the behavior of the next nearest Fe–Fe coupling $J_{02}^{Fe\text{-}Fe}$ was more complicated (see figure 5.12a). There was a strong linear reduction until the coupling switches even to a negative value (AFM). At $U_{eff}^{Fe} \approx 1$ eV, the slope was reversed but the $J_{02}^{Fe\text{-}Fe}$ coupling constants remained negative. Only the absolute values are decreased.

(ii) On the other hand, the magnetic exchange constants were obtained at the paramagnetic reference state (DLM approach, RS_{PM}). Again, the induced moments vanish. The remaining magnetic coupling constants (without $J^{Fe\text{-}Mo}$) were shown in figure 5.12a. In principle, they have a similar tendency as the magnetic exchange interactions in RS_{FM}.

From all these J_{ij}, only those between Fe–Fe and Fe–Mo up to the distance of 12.49 Å were considered in the calculation of T_t. The MFA was used besides the MC method for comparison. Both methods show qualitatively a similar non-linear variation with increasing electron correlation (see figure 5.12b), but the MFA overestimated T_t again. Therefore, only the results from the Monte Carlo simulations are discussed in the following.

A pure GGA calculation, including the induced Mo moments at 0 K (RS_{FM}), yields $T_t \approx$ 604 K, i.e. 200 K above the measured values. With an increasing U_{eff}^{Fe} and the metallic DOS,

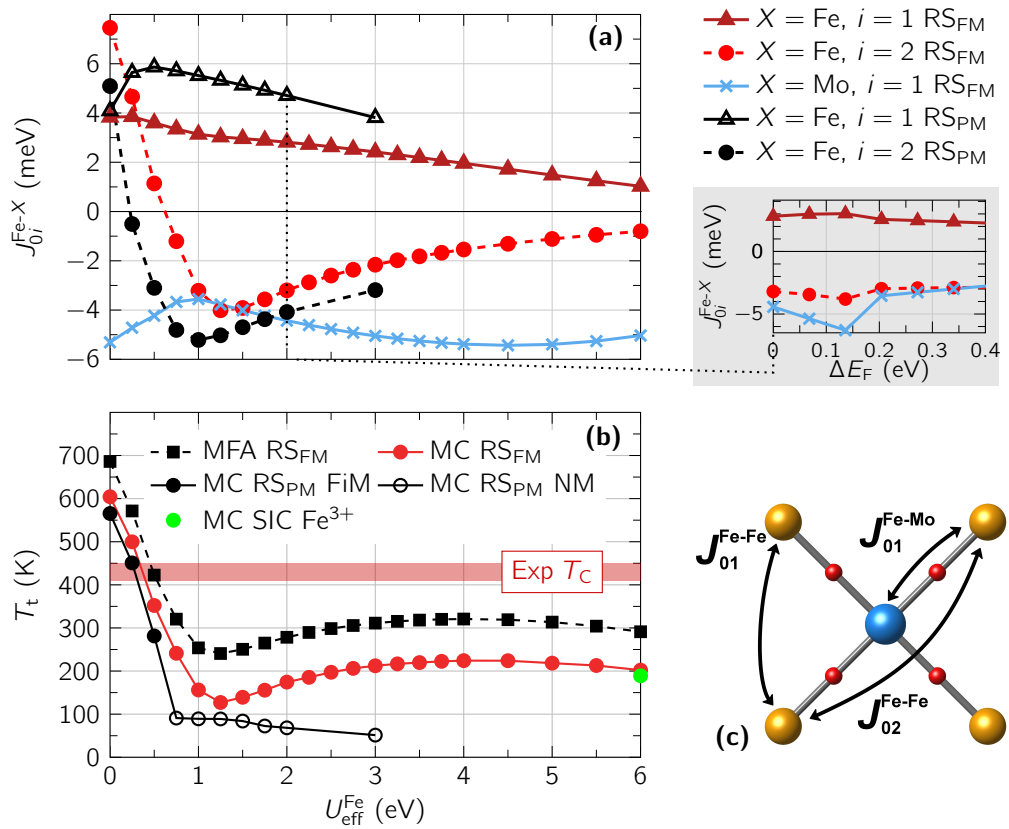

Figure 5.12: Magnetic properties of SFMO as a function of $U_{\text{eff}}^{\text{Fe}}$: (a) Magnetic exchange interactions J_{ij} obtained in RS$_{\text{FM}}$ and RS$_{\text{PM}}$. The gray shaded inset shows the J_{ij} at $U_{\text{Fe}} = 2\,\text{eV}$ (connected by the dotted line) for varying Fermi energy. (b) Curie temperature calculated from the corresponding J_{ij} with MFA or MC method. Comparison with the experimental range. The observed ground state change in the DLM model is marked with full and open circles (see text). (c) Sketch of the orientation of the magnetic exchange interactions J_{ij} between the Fe sites with their nearest and next nearest neighbors and with the nearest neighbor Mo sites.

the Curie temperature decreases linearly until $U_{\text{eff}}^{\text{Fe}} = 1\,\text{eV}$. This corresponds with the sign change of $J_{02}^{\text{Fe-Fe}}$ and the decrease of $J_{01}^{\text{Fe-Mo}}$. For half-metallic SFMO, the theoretical critical temperatures stayed always 200 K below the experimental T_t (compare shaded area in figure 5.12b) but increased slightly up to 250 K at $U_{\text{eff}}^{\text{Fe}} \approx 4\,\text{eV}$. This is observed despite the decrease of $J_{01}^{\text{Fe-Fe}}$. So, the stronger antiferromagnetic coupling between Fe and Mo sites mediates an additional FM coupling and increased T_t. For the sake of completeness, the T_t for a SIC calculation (see section 3.1.4) is plotted in green and matches with those of the GGA+U method in the limit of large $U_{\text{eff}}^{\text{Fe}}$. The slight reduction follows the tendency of $J_{01}^{\text{Fe-Mo}}$. Besided, the magnetic ground state in these Monte Carlo simulations was always an ordered ferrimagnetic (FiM) ground state with a nonzero saturation magnetization (see filled symbols in figure 5.12b).

The importance of the magnetic moments of Mo became even more obvious when considering as well RS$_{\text{PM}}$. The RS$_{\text{PM}}$ led to an increase in the magnitude of the nearest

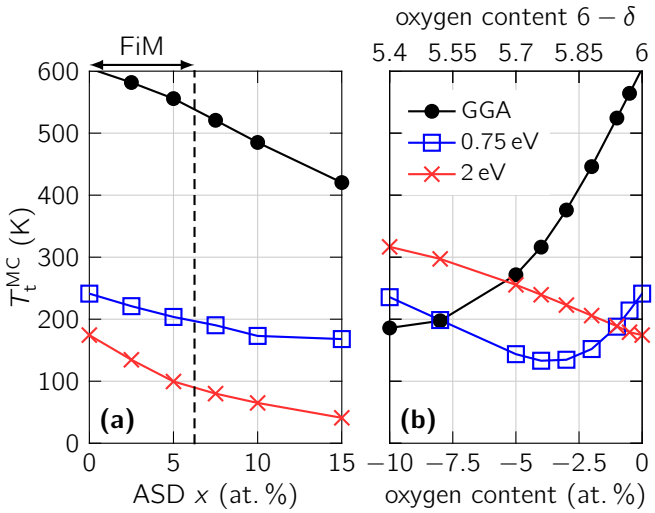

Figure 5.13: Critical temperatures of SFMO calculated with GGA or varying $U_{\text{eff}}^{\text{Fe}}$: (a) Including ASD. Up to 5 at. % the magnetic ground state was FiM, but becomes more complicated for more disorder. (b) Oxygen deficiency δ. The oxygen amount is also given in absolute values (scale above).

neighbor Fe coupling but with the similar tendency of the coupling constants in RS_{FM}. Above $U_{\text{eff}}^{\text{Fe}} = 1$ eV, the first and second neighbor interactions became equal in magnitude but got an opposite sign. Such a behavior and the missing AFM between the Mo and Fe ions altered the critical temperature dramatically. Only a low ordering temperature and a ground state with vanishing averaged saturation magnetization was observed (open circles in figure 5.12b). Although, the DLM is expected to give a better description of the magnetic phase transition, its possible shortcomings are not completely new. The induced moments of Mo might remain also above the transition temperature and the current single-site approximation of the local moments might not cover those correctly. An example of this issue was found during the investigation of the magnetic properties of Ni where only a non-local DLM approach could describe the moments sufficiently [92, 93].

In summary, the theoretical description underestimates the Curie temperature of half-metallic SFMO with respect to the experimental results. However, there might be various reasons for this discrepancy – defects like ASD or oxygen vacancies, additional electron doping or shortcomings in the description of the electronic structure. Their effect was estimated in the following sections.

5.6.3. The Curie temperature and defects

Unfortunately, experimental results of the influence of lattice defects on T_t could not be found in literature. So, using the CPA and simulating the effect of ASD and oxygen vacancies up to 15 at. % and 10 at. %, respectively, acts as a prediction for future experiments.

The inclusion of ASD reduces in general T_t, independent of GGA or GGA+U (see figure 5.13a). It follows from a stable large negative coupling constants (≈ -19 meV)

between the intrinsic Fe ions and Fe_{Mo} and the very weak coupling with the Mo ions at a Fe site (Mo_{Fe}), which were both almost independent of U_{eff}^{Fe}. The more site interchanges were made the less stable became the FiM ground state of SFMO, while at the same time the AFM coupling between Fe and Fe_{Mo} became stronger. The FiM ground state collapses finally for more than 5 at. % ASD to an non-magnetic ordered ground state. This new magnetic order is based on the stronger magnetic coupling and gets stabilized with more ASD, which explains the decreasing slope of the critical temperature variation in figure 5.13a. It is very likely that the large magnetic coupling even increases the critical temperature for higher amounts of ASD.

In contrast, the variation of T_t^{MC} with oxygen vacancies depends strongly on the electron correlations (see figure 5.13b). Already for the GGA, a strong reduction of T_t^{MC} in dependence on the oxygen amount follows a similar nonlinear tendency as $T_t^{MC}(U_{eff}^{Fe})$ (compare also figure 5.12). A turning point appeared for $U_{eff}^{Fe} = 0.75\,\text{eV}$, close to half-metallic SFMO. Here, the oxygen vacancies open finally the gap in the majority spin channel as it was seen for the DOS (see figure 5.10b). After that turning point, T_t^{MC} increases linearly with a similar slope as for the fully half-metallic SFMO ($U_{eff}^{Fe} = 2\,\text{eV}$). This increase is in the order of 80 K per 5 at. % oxygen vacancies. So, it is possible that the appearance of oxygen vacancies solve the above described discrepancy between the theoretical results for defect-free SFMO and the experimental observations.

5.6.4. The Curie temperature and electron doping

More generally, the oxygen vacancies dope the material system with additional free electrons. This n doping might also result from other defects, e.g. Navarro *et al.* [140] observed in their experiments an increase of T_t by substituting in SFMO Sr with La. This was related with an increase of the density of states at the Fermi energy $D(E_F)$. Such doping can be achieved in theoretical calculations by a shift of the Fermi energy E_F. For $U_{Fe} = 2\,\text{eV}$ within RS_{FM}, a small variation $\Delta E_F = 68\,\text{meV}$ (see dashed line in figure 5.14a) represents an n doping with additionally 0.15 electrons. It is related with an increase of $D(E_F)$ and T_t at about 10 K. This results from a stronger magnetic coupling (see inset in figure 5.12a). Unfortunately, there were stronger variations in the magnetic coupling constants beyond the next nearest neighbors (not shown) and additional influences to the magnetic coupling, e.g. the positions of unoccupied Mo $d^{\uparrow}_{x^2-y^2}$ states (and of similar symmetry) from the Fermi energy, which affects also the hybridization with the occupied states. So, the T_t could not be increased more strongly by more electron doping.

However, also the exchange splitting for the Mo d states might be a source of error. The Mo d electrons of the majority spin channel were in the first place sharp and above the Fermi level, while in the minority spin channel the d electrons are located at the Fermi level forming a relatively broad band (see figure 5.14). Their position was altered exemplarily through application of an additional Hubbard U parameter for Mo (U_{Mo}) in a range of 0.5 eV to 4 eV. It turns out that a small shift of spin up electrons could substantially increase the Curie temperature, e.g. using the same setup as before, T_t becomes 250 K for $U_{eff}^{Mo} = 2\,\text{eV}$ (see figure 5.14b). The main peak of the Mo $d^{\downarrow}_{x^2-y^2}$ states (and of similar symmetry) retained its position above E_F but the unoccupied Mo states of the majority spin channel were shifted substantially to higher energies. However, the

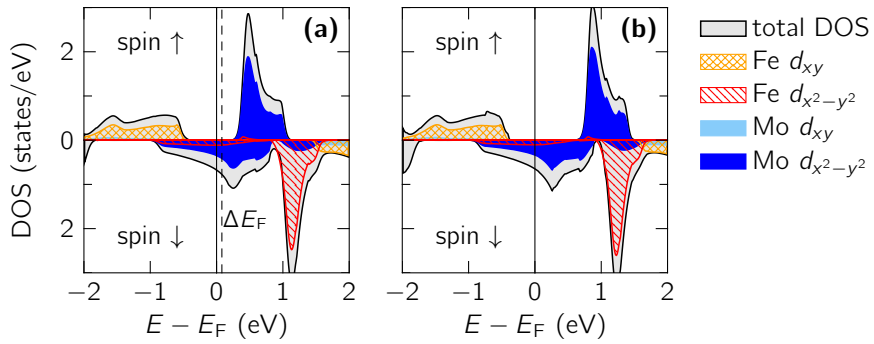

Figure 5.14: LDOS of Fe and Mo around the Fermi energy calculated with $U_{\mathrm{Fe}} = 2\,\mathrm{eV}$: (a) Simulated electron doping. (b) Exemplarily $U_{\mathrm{Mo}} = 2\,\mathrm{eV}$.

positions of the d electrons of the majority spin channel could also be not correct, since the DFT approach can usually not describe adequately unoccupied states and experimental investigations are missing.

Conclusions In order to describe the half metallic behavior of the SFMO, the GGA+U was applied on the d states of Fe. The band gap in the upper spin channel opens already at a small value of $U_{\mathrm{eff}}^{\mathrm{Fe}} = 2\,\mathrm{eV}$. Otherwise, the system remains metallic. The total magnetic moment is linearly reduced by both kinds of lattice defects, which is in good agreement with the experimental studies. On the other hand, the critical temperature T_{t} might be affected by several mechanisms. When the measured sample is doped with additional electrons due to some unknown defects or under consideration of electron correlation effects for the Mo ions, T_{t} would be higher than the theoretical prediction for bulk SFMO. The inclusion of oxygen vacancies might also raise the critical temperature. Antisite disorder might have the opposite effect and reduces T_{t} [E2].

Chapter 6.

Different Ordering Regimes in Metallic Non-magnetic Solid Solutions

Up to this point, the positions of possible lattice defects were only approximated as uncorrelated and randomly distributed. For the investigation of a more complex disorder regime, a simpler material has to be used. In particular, alloys that form solid solutions are suitable for this study, since these exhibit the possibility of substitutional disorder within the same lattice structure.

The $4d$ transition metals, silver and palladium, constitute the solid solution Ag_cPd_{1-c} where the concentration $c = c_{Ag}$ may vary in the whole range between 0 and 1. It is usually found to be in the face-centered cubic (fcc) lattice structure [141]. The wide concentration range allowed also for the investigation of disorder beyond the low concentration limit.

At first, the electronic and equilibrium properties of Ag_cPd_{1-c} alloys were calculated at the level of uncorrelated disorder (short-range order parameter $\alpha = 0$), to compare them with the results obtained in previous studies [22, 23, 27, 28]. Then, a certain degree of long-range order (LRO) was considered by interpolating between the concentrations $c = 0.25$, 0.5 and 0.75 with the MS-CPA or MS-NL-CPA (see section 3.4.4). At these concentrations, Müller and Zunger showed in their theoretical ground state search that there are possible ordered structures [24]. The variation of the equilibrium properties in the LRO regime was compared with the results obtained at $\alpha = 0$. Finally, the SRO parameter α was varied to investigate its influence on the electronic structure at the concentrations $c = 0.25$, 0.5 and 0.75.

6.1. Convergence study of the equilibrium properties

For the convergence test calculations, the local density approximation was used and l_{max} was restricted to $l_{max} = 2, 3, 4, 6$. The $\boldsymbol{k}$ points were used in a regular cubic grid with $k_{mesh} = 20, 40, 60, 80, 100, 120$ points along every edge of the cube. These input parameters provided a sufficient parameter space to obtain reasonable observables and to study the convergence of results (see figures 6.1 and 6.2).

With respect to the numerical calculations, the use of an alternative EOS, like the Morse EOS (3.57), Murnaghan EOS (3.44) or the third-order Birch-Murnaghan EOS (3.44), do not alter the qualitative tendency of the results [E12]. Their absolute values are less important, since the focus is set to the deviation of the equilibrium properties from their linear dependence on the chemical composition. Hence, the main discussion is restricted

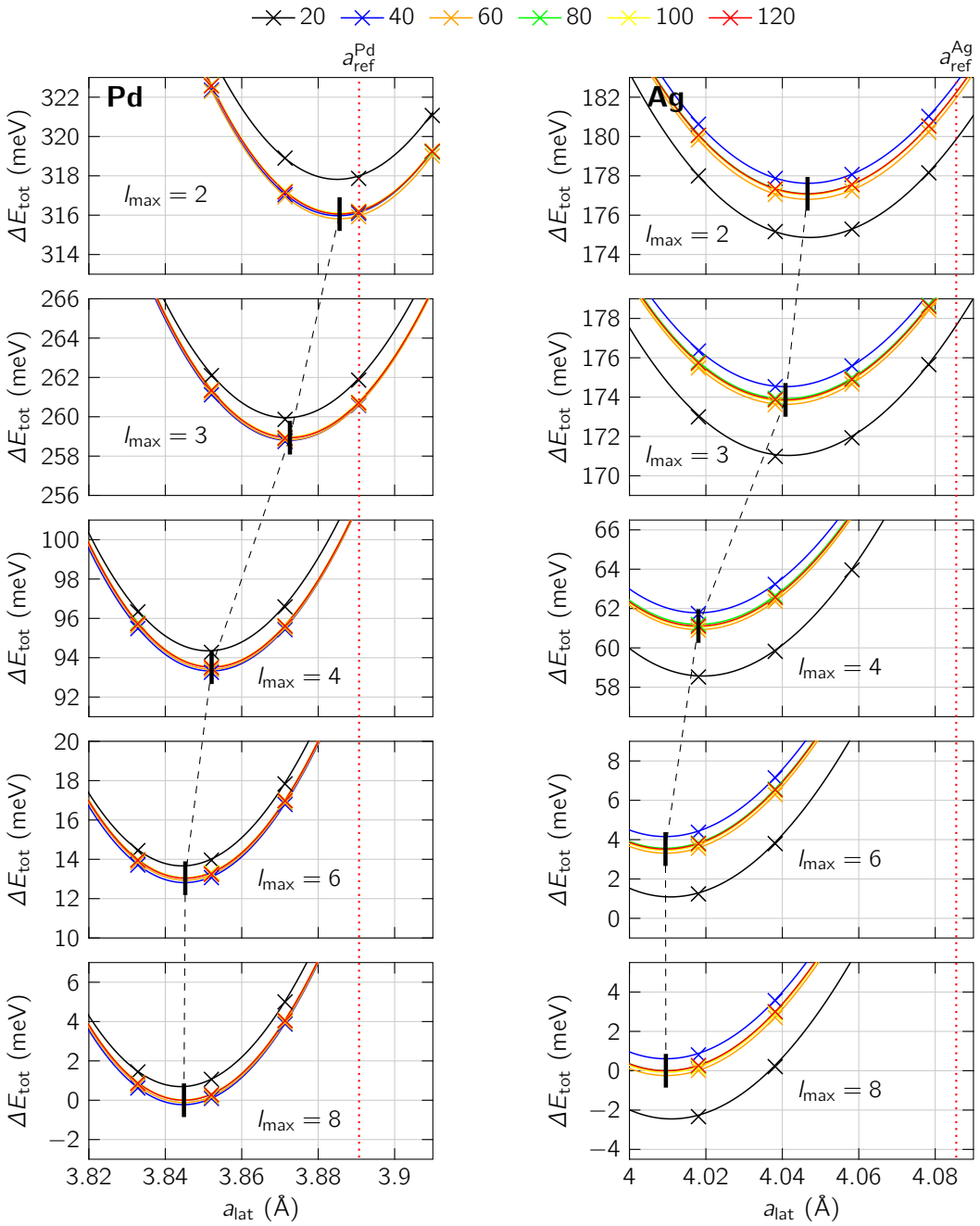

Figure 6.1: The calculated total energies with respect to the lattice constant for pure Pd (left) and Ag (right) in fcc structure. The different plots show the variation of k_{mesh} (legend at the top) for a particular l_{max} and are normalized to $E_{tot}(l_{max} = 6, k_{mesh} = 120)$. The solid lines show the fit with (3.56). Note the different energy scales. The equilibrium lattice constant values for $k_{mesh} = 120$ are shown with vertical black bars. To guide the eye, those values are connected by a dashed line. The red dotted lines show the experimental lattice constants [141].

Table 6.1: Numerical results of a_{eq} (in Å) and B_0 (in GPa) for $\mathrm{Ag}_c\mathrm{Pd}_{1-c}$ with $k_{\mathrm{mesh}} = 120$ and as a function of l_{max}. Last row shows the variation $\Delta_{l-l'} = 100|A(l) - A(l')|/A(l)$ (in %) for a quantity $A(l_{\mathrm{max}})$ between $l_{\mathrm{max}} = 4$ and $l_{\mathrm{max}} = 6$.

	Pd: $c = 0$		Ag: $c = 1$		$c = 0.1$		$c = 0.5$	
l_{max}	a_{eq}	B_0	a_{eq}	B_0	a_{eq}	B_0	a_{eq}	B_0
2	3.849	221.22	4.008	135.46	3.864	211.25	3.924	174.91
3	3.806	237.89	3.968	145.04	3.821	227.41	3.882	187.86
4	3.799	241.13	3.961	147.05	3.813	230.54	3.875	190.46
6	3.797	241.91	3.959	147.60	3.810	230.22	3.871	190.73
Δ_{6-4}	0.045	0.324	0.094	0.136	0.100	0.141	0.048	0.374

to the results obtained by fitting the numerical total energy calculations with the Birch-Murnaghan EOS (3.44).

The total energy $E_{\mathrm{tot}}(V)$ was evaluated for 17 different atomic volumes chosen around $\left(\bar{a}^{\mathrm{ref}}(c)\right)^3$. Thereby, $\bar{a}^{\mathrm{ref}}(c)$ was the average lattice constant linearly interpolated between the experimental lattice constants $a_{\mathrm{ref}}^{\mathrm{Pd}} = 3.8907$ Å and $a_{\mathrm{ref}}^{\mathrm{Ag}} = 4.0855$ Å. The lattice constant was varied by steps of ± 0.5 %. The resulting data points and their fits are plotted in figure 6.1 in dependence of k_{mesh} and l_{max}. It is obvious that the usual value of $l_{\mathrm{max}} = 3$ is not sufficient to describe properly the equilibrium properties, since the later variations are still significant. Thus, with respect to the value for $l_{\mathrm{max}} = 8$, the total energy decreases strongly for larger l_{max} values by 363 meV and 215 meV for Pd and Ag, respectively. The minimum of the EOS determines the equilibrium volume and the lattice constant, respectively. The latter varies by about 0.04 Å (≈ 1 %), (see dashed vertical lines in figure 6.1). Both theoretical lattice parameters are smaller than the experimental values [141] while the agreement is worst for Ag. However, this underestimation is expected for LDA calculations. The lattice parameter in dependence of the exchange-correlation functionals is discussed below in the context of the whole concentration range of the $\mathrm{Ag}_c\mathrm{Pd}_{1-c}$ alloys.

On the other hand, the curvature of the EOS (3.56) determines the bulk modulus. The stronger curvature for Pd indicates a higher stiffness in pure Pd than in pure Ag. The resulting equilibrium properties of the fitting with the EOS are visualized in figures 6.2a, 6.2b, 6.2e, and 6.2f with respect to the values calculated with $k_{\mathrm{mesh}} = 120$. Their variations showed in practice the same characteristics independent of l_{max}. In particular, the lattice parameter of the pure metals varied in a narrow range below 0.0001 Å when $k_{\mathrm{mesh}} \geq 60$ (see figures 6.2a and 6.2b). It is practically nothing in comparison to the variation for different l_{max} (see figure 6.1). In contrast, the bulk modulus converges much slower. Its variation shows in particular for Ag strong fluctuation in the sign but remains at least for $k_{\mathrm{mesh}} > 80$ in the range of ± 0.1 GPa (see figures 6.2e and 6.2f). However, the changes with k_{mesh} are still smaller than those for l_{max}, where the bulk modulus varies by about 21 GPa and 12 GPa for Pd and Ag, respectively (see table 6.1).

Since the investigation was also extended for arbitrary alloy concentrations of $\mathrm{Ag}_c\mathrm{Pd}_{1-c}$ with the CPA, the convergence behavior of same equilibrium quantities was studied as well. Here the effective medium of the CPA smooths e.g. the sharper band structures of the pure elements and causes a better convergence. This is indeed visible in the conver-

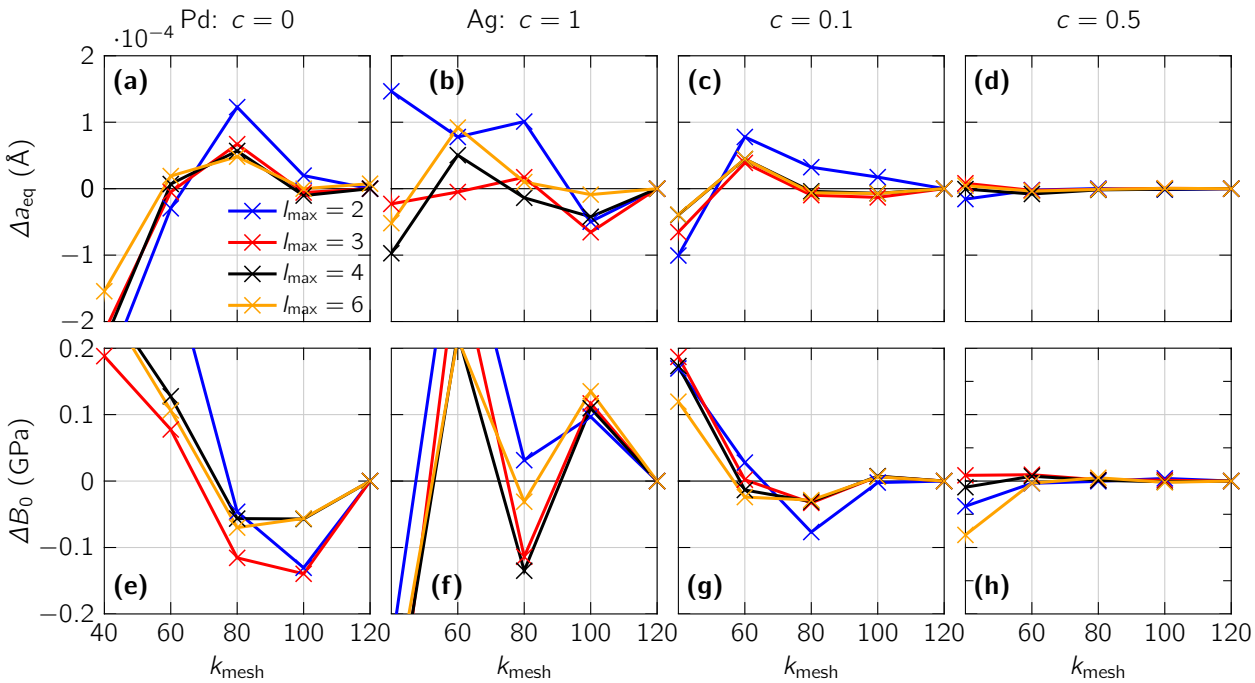

Figure 6.2: Absolute changes of the equilibrium properties with respect to the number of $\boldsymbol{k}$ points and l_{max} in Ag_cPd_{1-c}: (a)-(d) Equilibrium lattice constant. (e)-(h) Bulk modulus. The composition changes from left to right from Pd ($c = 0$), Ag ($c = 1$) to $c = 0.1$ and 0.5. The LDA functional was used in all calculations. Zero always corresponds to the value for 120 $\boldsymbol{k}$ points, which were assumed to be best converged. Note the scaling factor for the ordinate.

gence behavior with respect to k_{mesh} and l_{max} as well exemplarily shown for $c = 0.1$ and 0.5 in figures 6.2c, 6.2d, 6.2h, and 6.2g and in table 6.1.

For the purpose of numerical convergence, the variation of the results between two following data sets becomes crucial. When it is small enough, the results are considered as converged. As a compromise between numerical accuracy and computational effort, and the different convergence behavior of the calculations of equilibrium properties in pure metals or with the CPA, the following results were obtained with $l_{max} = 4$ and a full Brillouin zone sampling with a $\boldsymbol{k}$-points mesh of $k_{mesh} = 80$ ($\approx$ 11000 evaluations over the irreducible wedge).

6.2. Equilibrium properties of the AgPd alloy

6.2.1. Substitutional disorder in the solid solution

At first, the influence of the substitutional disorder in Ag_cPd_{1-c} on the equilibrium properties was studied under varying chemical composition c for the simple CPA model described in section 3.4.2. The totally random distribution in the solid solution corresponds to the SRO parameter $\alpha = 0$.

The total energy as a function of the volume was calculated in the whole concentration

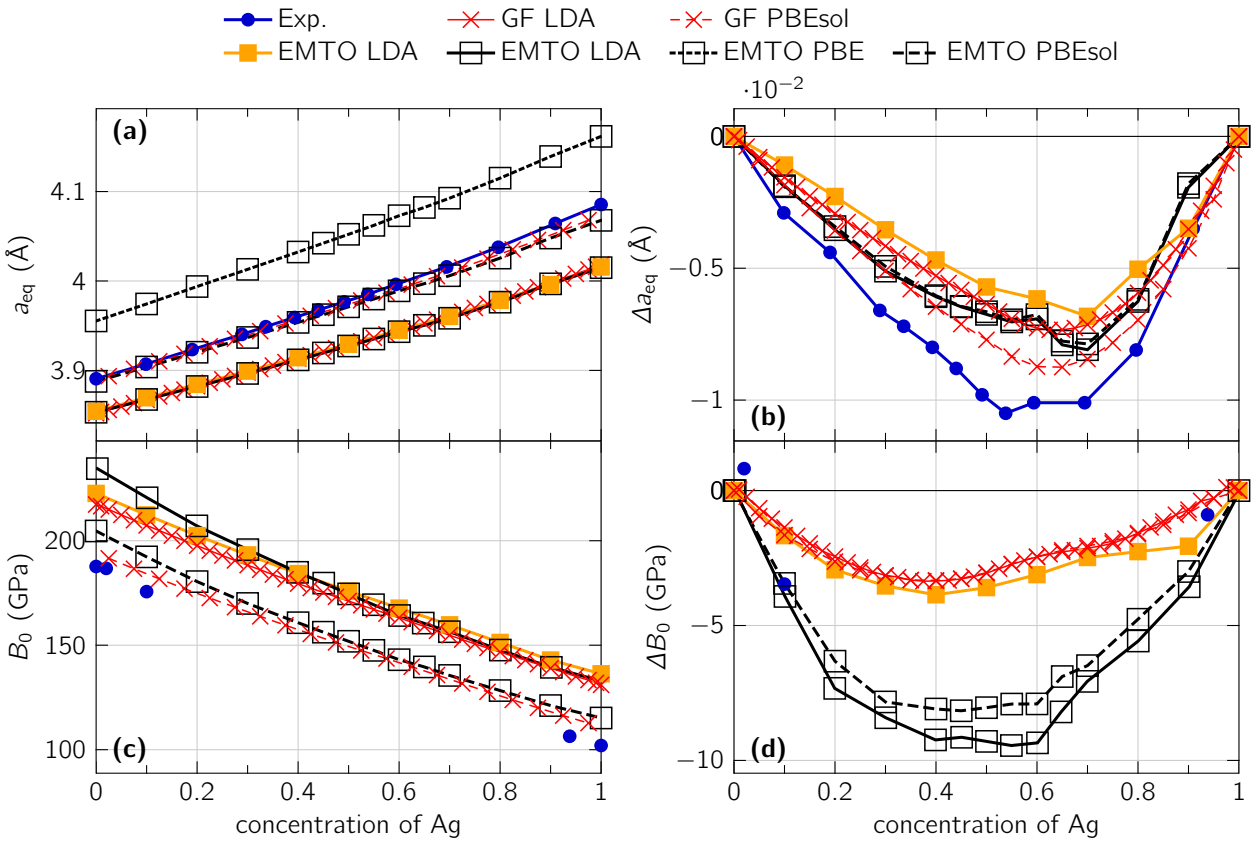

Figure 6.3: Equilibrium properties of Ag_cPd_{1-c} in the concentration range $c \in [0,1]$: (a) Absolute values of a_{eq}. (b) Deviation from the linearity (3.59) of a_{eq}. The scaling factor is given above the plot. (c) Absolute values of B_0. (d) Deviation from the linearity (3.59) of B_0. Different xc-functionals used in the GF method (red lines) are compared to calculations within the EMTO method (orange line [E12], black lines [22]). The experimental results for a_{eq} and B_0 are found in [141] or [142].

range in steps of $c = 0.1$ with the above discussed calculation setting and LDA. As observed already before for pure Pd or Ag, the equilibrium lattice constant is with respect to experimental measurements [141] underestimated in the LDA functional (see figure 6.3a). Simultaneously, the bulk modulus is overestimated (see figure 6.3c).

The results were compared with previous *ab initio* calculations done by Délczeg-Czirjak *et al.* [22] and calculated within the exact muffin-tin orbital method (EMTO) [60, 143–145]. In their paper, the authors discuss in detail the influence of the different exchange-correlation functionals to the equilibrium properties. Applying the same exchange correlation functional in the GF method lead to excellent agreement in particular for the lattice parameter (see figure 6.3a). However, discrepancies in the bulk modulus for c close to Pd appeared but proofed less important [E12], since higher accuracy in the EMTO calculations[1] varied slightly with respect to the previous results (see figure 6.3c). The good agreement of the GF with the EMTO method is not unexpected, since both are based numerically on the linear muffin-tin orbital method. The EMTO method proofed already a

[1] The recalculations with the EMTO code were done by Eero Nurmi [E12].

high reliability and accuracy for bulk modulus and single-crystal calculations for a large variety of material systems.

Although the best agreement of the absolute values of the equilibrium properties with experimental measurements was obtained with the PBEsol functional, the LDA functional was used in the following discussion [E12], since the relative changes in both curves showed the same significant features (see figures 6.3b and 6.3d), recalculated EMTO results match well with the GF method). The comparison of these deviations from the simple linear assumption of Vegard's law (3.59) with the electronic structure was the main focus of this part of the thesis, which motivated the choice of the LDA functional. Additionally, the LDA was also a compromise taking into account the larger computation times and numerical effort of the MS-NL-CPA for the inclusion of the short-range order.

Comparing Δa_{eq} with the experimentally observed deviation from Vegard's law showed again a good agreement with the main convex behavior and a minimum around $c = 0.6$ (see figure 6.3b). On the contrary, the scarce experimental data for the bulk modulus did not allow a reasonable comparison with the theoretical calculations but at least their order of magnitude of few GPa is similar (see figure 6.3d). The curve of ΔB_0 shows a smooth trend with an minimum at about $c = 0.4$ and a inflection point around $c = 0.6$.

6.2.2. Approximation of long-range order with the MS-CPA

Besides $\alpha = 0$ for the random distribution, the SRO parameter becomes minimal for long-range order (LRO). The ideal LRO is represented by a periodically ordered system and is simpler to calculate by first-principles methods than the disordered systems. However, there exist no experimental reports of known ordered structure in $\mathrm{Ag}_c\mathrm{Pd}_{1-c}$. Only by means of a theoretical structure search, Müller and Zunger [24] predicted three ordered structures for $\mathrm{Ag}_c\mathrm{Pd}_{1-c}$, at $c = 0.25$, 0.5 and 0.75. Their lattice structures are $\mathrm{L1}_1^+$, $\mathrm{L1}_1$ and $\mathrm{L1}_2$ in the nomenclature of the *Strukturbericht*. The two latter structures are very well known from other metallic systems but the first one is a new variation of $\mathrm{L1}_1$, described at first in [24].

The three ordered structures are constructed all from the same underlying fcc lattice and differ only in assigning specific elements to the particular sites in a large enough supercell. Thereby, the concentration range in between $c = 0.25$, 0.5 and 0.75 can be interpolated by means of the MS-CPA where some lattice sites changed continuously their atomic occupation in the supercell. Hence, only the total concentration inside the different supercells

$$c = \frac{1}{N_{\mathrm{sub}}} \sum_{s=1}^{N_{\mathrm{sub}}} c_{\mathrm{Ag},s}\,, \tag{6.1}$$

with the N_{sub} sublattices is comparable with the results of the CPA calculations. Different occupations of the sublattices might lead to the same global Ag:Pd ratio. This offers a high degree of flexibility to examine very different structures within a unified setup. The complex cell used to describe the three basic structures within one cell needs 8 sublattices (see table 6.2). In principle, 2 or 4 sublattices are enough to describe a periodic lattice with $\mathrm{L1}_1$ and $\mathrm{L1}_2$, respectively, but exceed their possibilities when including also $\mathrm{L1}_1^+$ and covering the whole concentration range $c \in [0, 1]$ (see figures 6.4a to 6.4c).

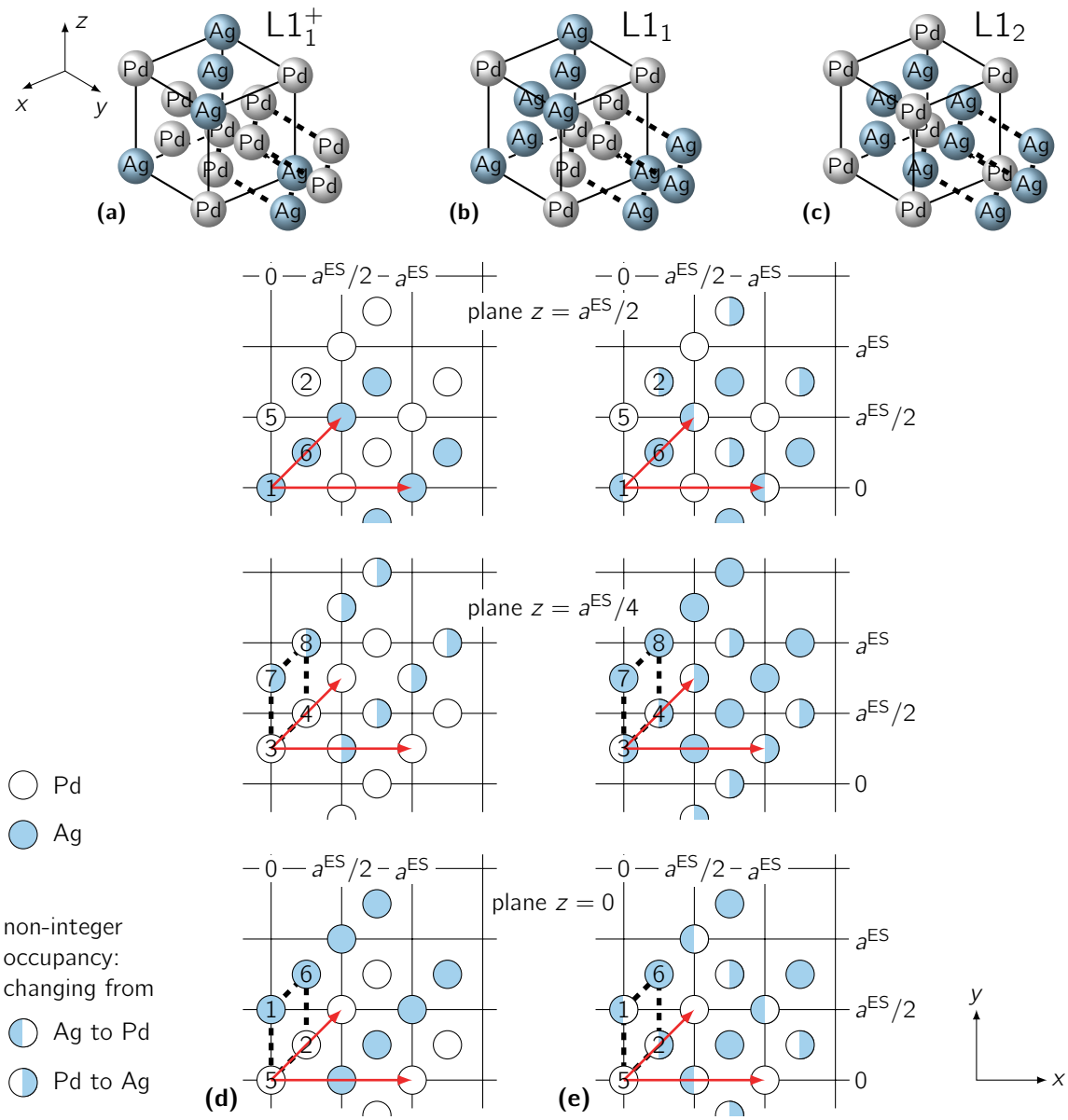

Figure 6.4: Schematic representation of the ordered structures (a) to (c) used for LRO case study. (d) The transition between $L1_1^+$ and $L1_1$. (e) The transition between $L1_1$ and $L1_2$. Both are shown in the extended setup described by the vectors in table 6.2 ($\boldsymbol{R}_1^{ES}$ and $\boldsymbol{R}_2^{ES}$ are red, $\boldsymbol{R}_3^{ES}$ points out of the plain). The supercell is illustrated with 3 slices orthogonal to the z axis (from bottom to top: $z = 0$, $0.25\,a^{ES}$ and $0.5\,a^{ES}$). The thick dashed lines link the basis sites in the corresponding plain. Circles in different colors at the nodes of a simple cubic (sc) lattice (underlying grid) denote different atomic occupation at the corresponding sublattices, either pure Ag or Pd or varying occupation treated with CPA.

Table 6.2: List of the $N_{\text{sub}} = 8$ nonequivalent sublattices used to compare the 3 LRO structures $L1_1$, $L1_2$ and $L1_1^+$ within a unified framework. The basis vectors of the extended supercell are $\boldsymbol{R}_1^{\text{ES}} = a^{\text{ES}}(1, 0, 0)$, $\boldsymbol{R}_2^{\text{ES}} = a^{\text{ES}}(1/2, 1/2, 0)$, $\boldsymbol{R}_3^{\text{ES}} = a^{\text{ES}}(0, 1/2, 1/2)$.

Sublattice	Origin	Sublattice	Origin
$\boldsymbol{a}_1$	$(0, 1/2, 0)$	$\boldsymbol{a}_5$	$(0, 0, 0)$
$\boldsymbol{a}_2$	$(1/4, 1/4, 0)$	$\boldsymbol{a}_6$	$(1/4, 3/4, 0)$
$\boldsymbol{a}_3$	$(0, 1/4, 1/4)$	$\boldsymbol{a}_7$	$(0, 3/4, 1/4)$
$\boldsymbol{a}_4$	$(1/4, 1/2, 1/4)$	$\boldsymbol{a}_8$	$(1/4, 1, 1/4)$

The concentration change between the three ordered structures was simulated with some basis sites having different non-integer occupation (see figures 6.4d and 6.4e). The sketch illustrates two particular situations. The transition between the $L1_1^+$ and $L1_1$ structures ($c = 0.25, 0.5$) is depicted in figure 6.4d. The sublattices $\boldsymbol{a}_i$, $i = 1, \ldots, 6$ are fixed and occupied by an Ag, 4 Pd and again an Ag atom, respectively, whereas the two sublattices sites $\boldsymbol{a}_7$ and $\boldsymbol{a}_8$ exhibit the same concentration $c_7 = c_8$ with $c_7 \in [0, 1]$ varying from pure Pd ($c_7 = 0$) to pure Ag ($c_7 = 1$).

The same procedure can be applied for a transition between the $L1_1$ and $L1_2$ structures ($c = 0.5, 0.75$) depicted in figure 6.4e, where this concentration range is limited to $c_1 \in [1, 0]$, while the Ag concentration on the remaining sublattices varies like $c_2 = c_3 = c_4 = 1 - c_1$. The sublattices $\boldsymbol{a}_5$, $\boldsymbol{a}_6$, $\boldsymbol{a}_7$ and $\boldsymbol{a}_8$ are occupied by Pd, Ag, Ag and Ag, respectively.

The material was now characterized by a set of $N_{\text{sub}} = 8$ concentrations, one for each sublattice of the extended supercell. The fully uncorrelated alloy may still be obtained by assigning the same concentration to each site, regardless of its coordination with neighbors. In terms of the SRO parameter $\alpha_{BA}(p_{BA}(r))$ in (3.107), the concentrations c_s represent the probabilities p_{BA} of their respective sublattices. The calculation procedure was similar as described in section 3.4.5 with only one configuration and the possibility of

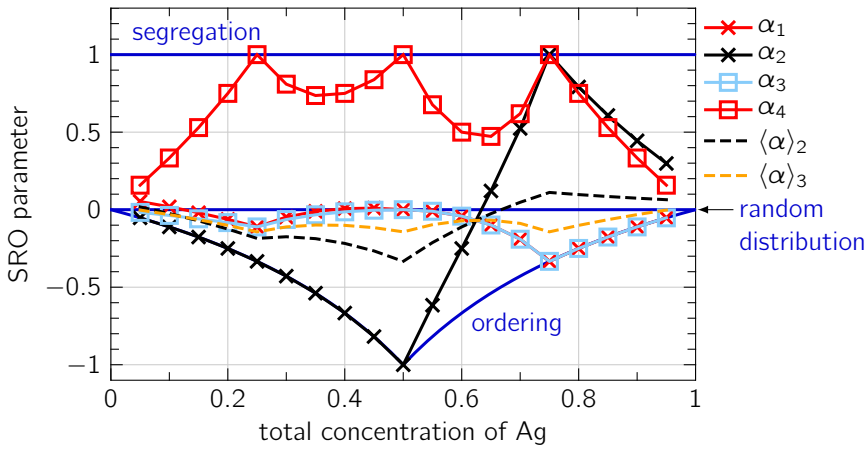

Figure 6.5: The shell dependent SRO parameter α_s of the ordered regime (LRO) with the MS-CPA as a function of the total concentration up to $s = 4$. The SRO parameters $\langle\alpha\rangle_2$ and $\langle\alpha\rangle_3$ are averaged over 2 and 3 shells, respectively. The blue lines show the limits of the SRO parameter, ordering, random distribution or segregation.

noninteger occupation number.

The resulting shell dependent SRO parameter was compared with the uncorrelated case and its limits up to the fourth shell or the average over the first two coordination shells via (3.151) (figure 6.5). It becomes obvious that the simple interpolation between the three ordered structures with the MS-CPA represents not the ideal LRO case in terms of the SRO parameter but α behaved rather differently in the different concentration regimes. For the nearest neighbor shell, $L1_1^+$ and $L1_2$ show an ordering tendency, whereas the SRO parameter is $\alpha = 0$ for the $L1_1$ structure. The twelve nearest neighbor atoms in $L1_1$ are occupied by 6 Ag and 6 Pd atoms. In contrast, the occupation of the second shell showed up to $c = 0.5$ a minimal α and segregation in the $L1_2$ structure. These results for the first two shells as well the segregation tendency of the fourth shell are contradictory with the used ideal LRO structures. In case of the $L1_1$ structure, the average over the first two shells $\langle\alpha\rangle_2$ yields ordering tendencies while it remained positive for $L1_2$. The different behavior of the SRO parameter is caused by the different periodicity of the ordered structures. One type of atom repeats itself completely in the second coordination shell for the $L1_2$ structure while it happens just after four shells in $L1_1$. So, the ordering in $L1_2$ is practically ideal and characterized by α_1. On the contrary, the ideal order at $c = 0.5$ would be achieved in a rock salt-type structure. $L1_1$ is less ordered, since the single atomic layer can be recognized as partially segregation. This segregation averages to zero for α_1 with the different atomic types in the next sheet and the order should be described by an average over several shells, e.g., $\langle\alpha\rangle_2$ or $\langle\alpha\rangle_3$. This means according to (3.151) in particular for $L1_1$ that

$$\langle\alpha\rangle_2 = (-12 \times 0 - 6 \times (-1))/18) = -1/3\,, \tag{6.2}$$

$$\langle\alpha\rangle_3 = (-12 \times 0 - 6 \times (-1) - 24 \times 0)/42) = -1/7\,. \tag{6.3}$$

The same is valid for $L1_1^+$ and the averaged SRO parameter are

$$\langle\alpha\rangle_2 = (-12 \times 1/9 - 6 \times 1/3)/18) = -5/27\,, \tag{6.4}$$

$$\langle\alpha\rangle_3 = (-12 \times 1/9 - 6 \times 1/3 - 24 \times 1/9)/42) = -1/7\,. \tag{6.5}$$

In conclusion, a single average of the SRO parameter with the coordination number (3.151) might not be a reliable approach to differentiate between different ordered structures, since the periodicity of the structures changes gradually throughout the concentration range. The choice of the right SRO parameter was not obvious. However, qualitative statements were possible using either $\langle\alpha\rangle_3$ or $\min(\alpha_1, \langle\alpha\rangle_3)$. All three ordered structure ($c = 0.25$, 0.5 or 0.75) show a distinct minimum, which indicates ordering. The crossing point between α_1 and $\langle\alpha\rangle_3$ is exactly between $L1_1$ and $L1_2$ at $c = 0.625$ (figure 6.5). In particular, the latter choice of $\min(\alpha_1, \langle\alpha\rangle_3)$, takes into account the segregation in the second shell for $L1_2$ and the different degree of ordering when going from $c = 0.5$ to $c = 0.75$. It allowed some qualitative statements with respect to physical quantities, as it is showed in the following section.

6.2.3. Comparing random distribution and long-range order

The equilibrium properties were calculated for the LRO setup, which was described in the last section, and compared with those of the single-site CPA calculations in section 6.2.1.

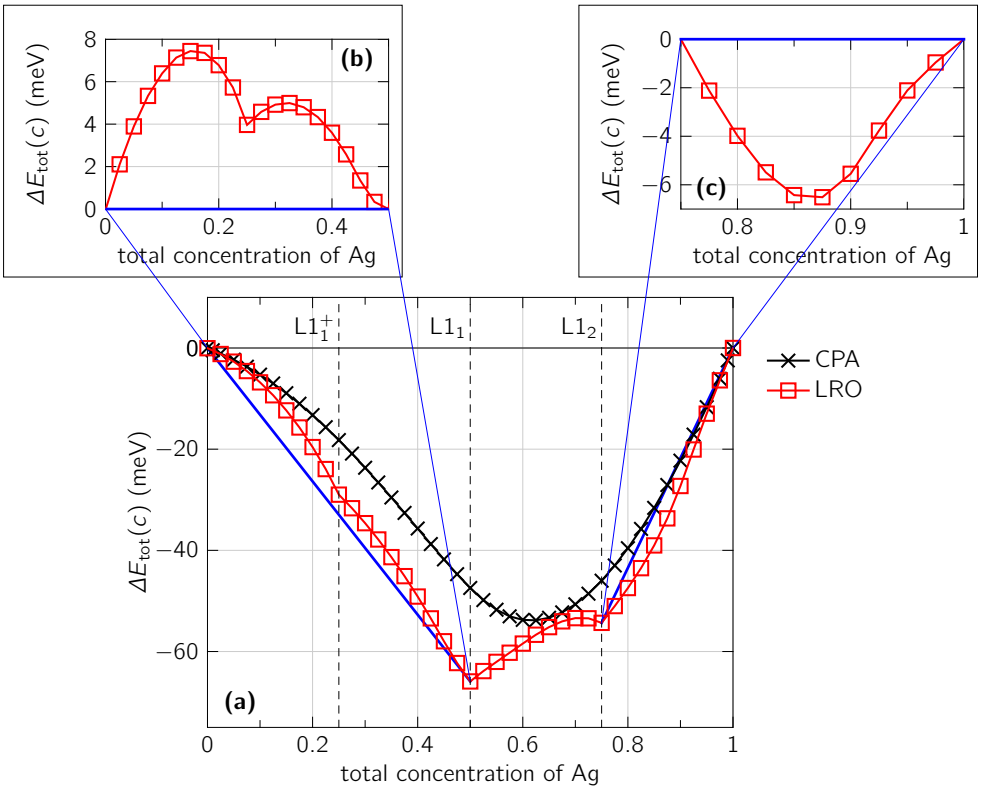

Figure 6.6: The non-linear component of the equilibrium total energy as a function of a total concentration interval in Ag_cPd_{1-c}: (a) Over the whole total concentration range ($c \in [0,1]$). The total energy of the supercell described in table 6.2 (squares) is compared with those of the single-site representation (crosses). The blue lines visualize the connection to the shorter concentration intervals $c \in [0, 0.5]$ and $c \in [0.75, 1]$ depicted in (b) or (c). The linear reference is also marked in blue.

Comparable results only require to account for the enlarged direct space volume of the supercell with $N_{sub} = 8$ instead of one sublattice in the fcc unit cell. The number of sampling points in the reciprocal space Brillouin zone integrals could be reduced to $k_{mesh} = 40$ ($40^3 = 64000 \simeq 80^3(a^{fcc}/a^{ES})^3$). In the same way, as for the single-site approximation the equation of states (3.56) was fitted to a number of total energies as a function of the lattice constant a^{ES}. For the derivation of the differences to the Vegard's law the linear fit (3.59) between the results of the pure Pd and Ag systems were used.

In order to validate the choice of the LRO setup, the higher stability of these crystalline phases with respect to the fully uncorrelated CPA results was compared with the equilibrium total energy deviation from the linear behavior (see figure 6.6). Over the whole concentration range, the extended setup exhibits a lower total energy. At the particular Ag:Pd ratios 1:3, 1:1 and 3:1, three clear local minima were obtained as expected. They correspond to the $L1_1^+$, $L1_1$ and $L1_2$ geometries indicated with dashed lines in figure 6.6a. In between $L1_1$ and $L1_2$ at ≈ 0.65, the total energies get close to each other. This might correspond to the crossing point in the SRO parameter in figure 6.5. The SRO parameter of the chosen LRO setup gets close to $\alpha = 0$ and the total energies of LRO or random distribution might be of a similar order of magnitude. At higher concentrations, the $L1_2$

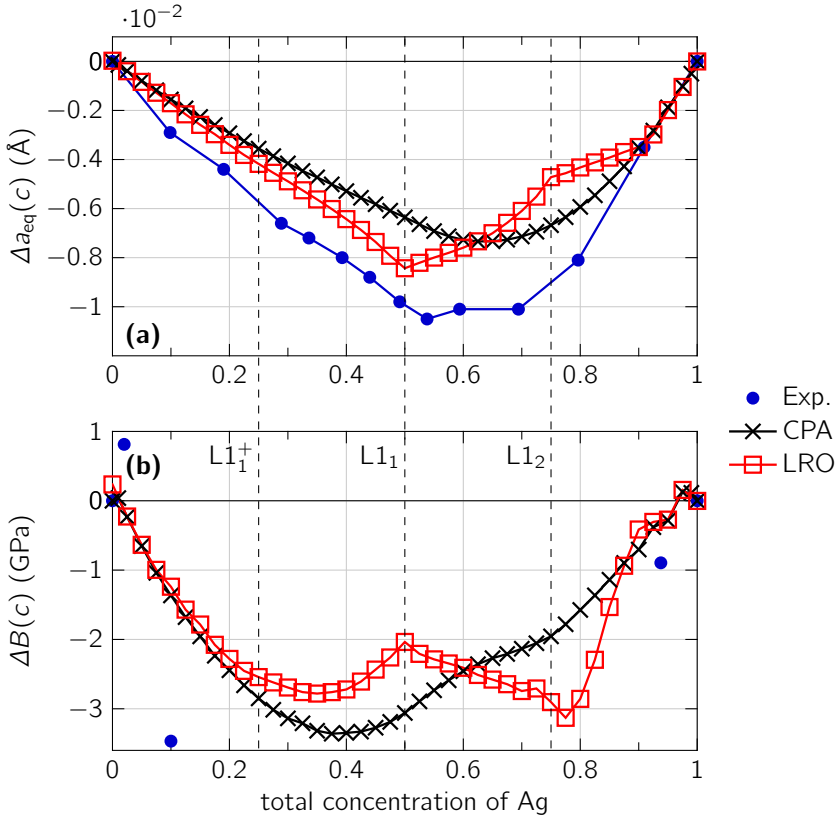

Figure 6.7: The deviation from the Vegard's law (3.59) of the equilibrium properties as a function of the total concentration: (a) Equilibrium lattice constant. (b) Bulk modulus. The results of the single-site representation (crosses) are compared with those of the extended setup described in table 6.2 (squares) and with experimental values [141, 142].

structure becomes more distinct and the local minimum appears.

When varying c between the pure Pd and the $L1_1$ structure (sites $\boldsymbol{a}_5 - \boldsymbol{a}_8$ fixed), the deviation from linear behavior of total energy within this concentration range highlights a shallow local minimum for the newly suggested $L1_1^+$ ordered phase [24] (see figure 6.6b). The smaller range of $c \in [0.75, 1]$ was chosen to emphasize the appearance of a concave deviation from linearity, which hints to another possible ordered phase for the Ag_cPd_{1-c} alloy within this concentration range (see figure 6.6c). The LPS_3 structure [146] was found to be about 6 meV/atom more stable than the $L1_2$ structure, representing about 10 % of the calculated formation energy for the $L1_2$ phase. Thus, taking into account the formation energy for the LPS_3 in figure 6.6 does not rule out the existence of another ordered phase for the $c \in [0.75, 1]$ interval.

Furthermore, a comparison of the other equilibrium properties with the single-site CPA evaluations shows significant differences in the medium concentration range $c \in [0.25, 0.9]$ while they appear independent of the different ordering in the low concentration limits (see figure 6.7). As before for the variation of the total energy, the results obtained in the CPA were much smoother over the whole concentration range.

Starting from a low Ag concentration adding more and more Ag shows a similar reduction of the equilibrium lattice constant, which matches well with respect to the experiment

for $c_{\mathrm{Ag}} < 0.5$. This reduction is stronger in the ordered regime, but changes its qualitative behavior at $c \approx 0.6$ (see figure 6.7a). This crossing point might correspond, as for the total energy, with the qualitative variation of the SRO parameter at $c = 0.625$ (see figure 6.5). At the end of the concentration range, both results match again very well with the measurements. A similar variation between the LRO and CPA setups at $c \approx 0.6$ was found for the bulk modulus as well (see figure 6.7b). It varies in absolute terms in a range of 1 GPa to 1.5 GPa, and reflects similar findings in the order vs. disorder differences obtained in a recent, independent EMTO study of the $Ag_{0.5}Pd_{0.5}$ case [23]. Unfortunately, a comparison to the few experimental data points and, thereby, any conclusions about the ordering are not possible at this point.

In general, the observed slope change may result from the differences between the $L1_1^+$ and $L1_1$ vs. $L1_2$ arrangements of the unit cell. The latter case represents an isotropic construction, while both former ones describe an anisotropic structure along the [111] direction (see figures 6.4a and 6.4b). In particular, for the $L1_1$ case Delczeg-Czirjak *et al.* [23] showed that the structural anisotropy translates into different compressibilities along the a and c axis. The ordered $L1_1$ phase consists in fact of alternate Ag and Pd layers, perpendicular to the c axis, and has a larger bulk modulus that places related arrangements also closer to the ideal, linear $B_0(c)$ trend of Vegard's law.

The expectation of a linear behavior finds its origin in the idea of simple combination of bulk moduli of the two pure elements, only weighted by the relative concentration. A layered arrangement such as the $L1_1$ structure describes the regular repetition of the same elements along parallel planes. This sort of phase separation may reasonably lead to expect higher robustness of individual pure elements' properties against the stronger smearing of a fully disordered distribution. This hypothesis may be tested by considering other cases of even larger alike elements repetition. Increasing the layer thickness of the reference $L1_1$ structure from an Ag/Pd/Ag/Pd/Ag/Pd stacking (corresponding to ABC ABC in the [111] direction of the fcc cell) to the AgAg/PdPd/AgAg/... sequence (with ABC ABC ABC ABC), further reduction of bulk modulus deviations from linearity by $\approx$ 1 GPa was indeed observed, despite loss of stability for such rather artificial arrangement.

Similar arguments may be applicable for the $L1_1^+$ reference. In this case, structural anisotropy is reduced because of the development of Ag chains perpendicular to the [111], [$\bar{1}$10] and [001] directions (see figure 6.4a). This does not apply to the more isotropic $L1_2$ structure, which cannot be simply modified to form layers or chains in any particular directions. The stiffer constituent Pd always forms only a loose "skeleton" of atoms, embedded within an Ag matrix.

6.3. Electronic topological transitions in different disorder regimes

As originally showed by Bruno *et al.* [27, 28], a continuous change in the concentration can lead to a series of discrete transitions in the Fermi surface, so-called electronic topological transitions (ETT) or Lifshitz transitions. The connectivity of the Fermi surface may change radically, as some necks close or new ones develop between repeated instances of the

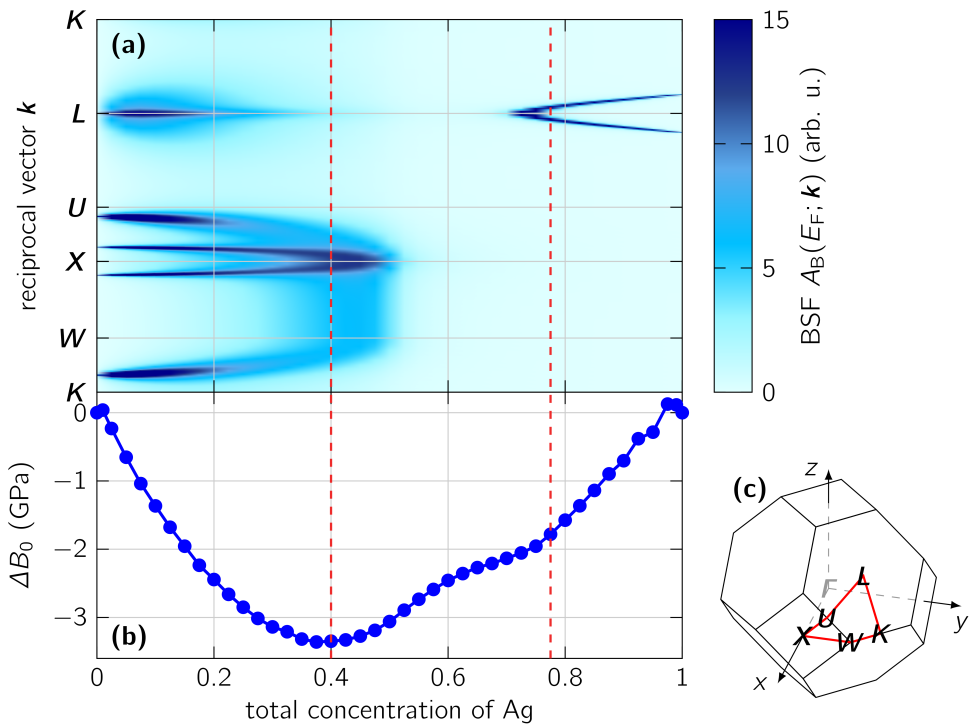

Figure 6.8: (a) Contour plot of the Bloch spectral function at the Fermi energy along the $\boldsymbol{K} - \boldsymbol{W} - \boldsymbol{X} - \boldsymbol{U} - \boldsymbol{L} - \boldsymbol{K}$ reciprocal space path (red line in (c)) and evaluated for different concentrations c for the single-site CPA study of the Ag_cPd_{1-c} system. (b) The bulk modulus deviation as shown in figure 6.3d. (c) The fcc Brillouin zone with its high symmetry points. The values in between the $c = 0.05$ intervals are linearly interpolated. The dashed red lines mark substantial changes in the Fermi surface topology.

Brillouin zone (see figure 3.3). Such variations should be correlated with the changes in the trends of the equilibrium properties as observed in section 6.2.3. Therefore, the electronic structure represented by means of the BSF (3.29) was at first calculated for the single-site CPA and the LRO setup [E12].

If $A_B(E_F, \boldsymbol{k})$ is calculated along a line in the $\boldsymbol{k}$ space from the origin of the Brillouin zone to its surface, there might appear several peaks in $A_B(E_F, \boldsymbol{k})$ indicating the electronic states with E_F at $\boldsymbol{k}$. The peak closest to the surface of the Brillouin zone defines a point of the Fermi surface along the considered line in the $\boldsymbol{k}$ space [26]. This holds true in particular for the disordered case within the CPA. In terms of the fcc lattice structure of the AgPd alloy such a line is, e.g., going from $\boldsymbol{\Gamma}$ to $\boldsymbol{L}$ in the fcc Brillouin zone shown in figure 6.8c.

However, the actual calculations were done slightly different, since the exact shape of the Fermi surface is not needed to track an ETT. Instead of starting at Γ, only the Brillouin zone surface is considered. In the moment a peak of $A_B(E_F, \boldsymbol{k})$ appears at the surface, a part of the Fermi surface crosses the Brillouin zone boundary and the electronic connectivity varies. Considering all the high symmetry points in the Brillouin zone allows to reduce the number of calculations to a path along the surface of the Brillouin zone (red line in figure 6.8c). This path plotted as the ordinate in figure 6.8a. It shows the color

coded variation of the Bloch spectral function with changing concentration. Dark blue colors indicate a peak in the BSF at the Brillouin zone surface appearing or vanishing when going from Pd to Ag. These ETT were correlated with the anomalies of the bulk modulus $\Delta B_0(c)$ depicted below the contour plot (see figure 6.8b).

It is possible to observe several peaks for pure Pd ($c = 0$) and the typical neck around the $\boldsymbol{L}$ point for Ag ($c = 1$). While alloying Pd with Ag, the valence band of Pd (see figure 3.3e) moves towards and crosses the Brillouin zone surface. Thereby, the peaks in $A_{\mathrm{B}}(E_{\mathrm{F}}, \boldsymbol{k})$ merge or the neck around the $\boldsymbol{X}$ point closes for $c \approx 0.4$ (dashed red lines draw the connection between figure 6.8a and 6.8b). For further increasing the Ag content, another band crosses the Brillouin zone surface at $c \approx 0.75$ and evolves into the neck around the $\boldsymbol{L}$ point. This opening of a neck seems to be connected with the curvature change in ΔB_0. Hence, the relative smoothness of the single-site CPA effective medium results leaves some uncertainty with respect to the exact placement of such connecting lines. In any case, three qualitatively different concentration intervals $c \in [0, \simeq 0.4]$, $c \in [\simeq 0.4, \simeq 0.75]$, and $c \in [\simeq 0.75, 1]$ can be observed. They have different curvatures and correspond to the different ranges in the BSF. A cautious conclusion from these calculations might be the association of open necks with positive curvature ($c \in [0, \simeq 0.4]$ and $c \in [\simeq 0.75, 1]$) and no intersection of the Brillouin zone with negative curvature ($c \in [\simeq 0.4, \simeq 0.75]$).

A similar analysis of the BSF for LRO setup leads to a much more complicated contour plot (see figure 6.9). Due to the similar lattice structure, the Brillouin zone itself is the same as before, but the different occupation of the sublattices led to an increase of the irreducible Brillouin zone (see blue dashed line in figures 6.9f and 6.9g). In order to catch all significant ETT, four different paths along the Brillouin zone surface are needed (color coded in figure 6.9). In general, the integer occupancy on some sublattices gives rise to a sharper band structure over the whole concentration range and the larger cell supplies more bands than the fcc cell. Thus, two different regimes may be noted.

For $c \in [0, 0.5]$, the d bands of Pd cross the Fermi level, and are depicted as a rich set of clearly resolved features along all reciprocal space paths. This set forms a strong contrast to the simpler appearance of the first part in the plot for the CPA results (see figure 6.8a). There, most features appear smeared out and are left unresolved in the uncorrelated, single-site approach, whereas the ETT appear at different concentrations. The bulk modulus deviation $\Delta B_0^{\mathrm{ES}}(c)$ shows three main transitions in the first half of figure 6.9, at $c \simeq 0.225$, $c \simeq 0.325$, and $c \simeq 0.425$. More specifically, the first feature may be associated with the merging at the $\boldsymbol{X}_1$ point, while the subsequent interval $c \in [0.325, 0.425]$ could be correlated with changes occurring at the $\boldsymbol{L}_1$ point. Further variations at about $c = 0.5$ can be related to the merge at the $\boldsymbol{K}_2$ or the $\boldsymbol{U}_2$ point. However, the dominant closure of two peaks at the $\boldsymbol{L}_2$ point does not seem observable in ΔB_0^{ES}, which may be related to an unique character of this feature. It might be related to the threefold symmetry axis due to the layered stacking in this region $c \in [0.5, 0.75]$.

When the content of silver exceeds $c = 0.5$, only the sp bands cross the Fermi level. This leads to a simpler appearance in the contour of figure 6.9. It is again comparable to the CPA results calculated at the same concentration interval (see figure 6.8). In this regime, different topological transitions do not overlap with each other. The corresponding ΔB_0^{ES} curve shows more pronounced variations that relate more clearly with the BSF results. In particular, two ETT's can be observed, at the $\boldsymbol{X}_1$ point for $c \approx 0.775$ and at the $\boldsymbol{K}_1$ or $\boldsymbol{K}_4$

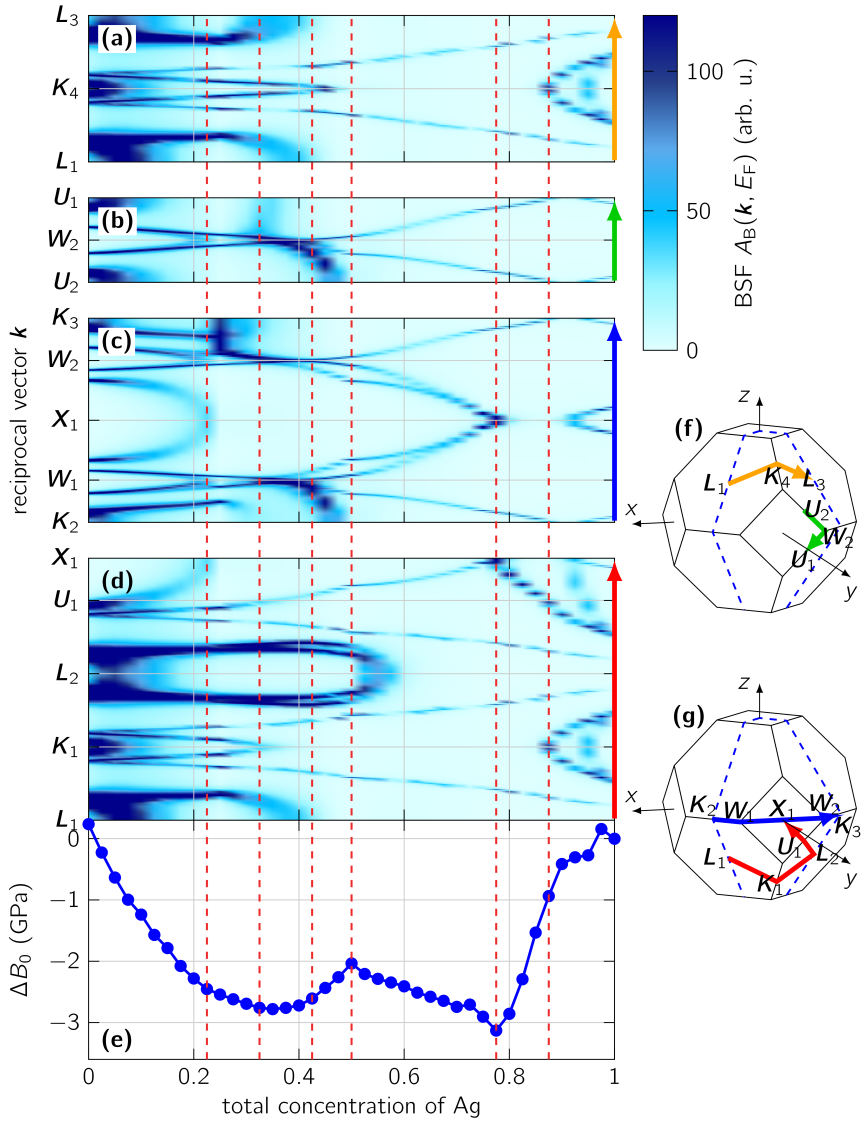

Figure 6.9: (a)-(d) Contour plot of the Bloch spectral function at the Fermi energy along various reciprocal space paths evaluated for different concentrations c of the extended LRO setup of figure 6.4. The dashed red lines are applied in the same way as in figure 6.8 with bulk modulus deviations depicted in (e). The paths in the reciprocal space are sketched and color coded atop the fcc Brillouin zone in (f) and (g). The blue dashed lines indicate the irreducible Brillouin zones.

point for $c \simeq 0.875$. For ΔB_0^{ES}, these translate into sharp kinks, and rather homogeneous slopes in the featureless regions in between ($c \in [0.5,\ 0.775]$ and $c \in [0.775,\ 0.875]$).

Thus, for both disorder regimes, microscopic changes in the Fermi surface are associated with variations of the macroscopic bulk modulus. This study will be complemented by considering a distinct regime of SRO in between $\alpha = 0$ and LRO for the $\mathrm{Ag}_c\mathrm{Pd}_{1-c}$ alloy with the MS-NL-CPA [E12]. Thereby, the extended supercell can be used again with $N_{\mathrm{c}} = 1$ and $N_{\mathrm{sub}} = 8$ (see table 6.2), which leads to $N_{tot} = 2^{N_{\mathrm{sub}}} = 256$ different configurations γ of 8 Ag or Pd atoms. On the one hand, the MS-NL-CPA framework allows

Table 6.3: MS-NL-CPA configurations corresponding to the LRO setup with the lattice structure of the extended setup (table 6.2). By choosing the probability $P(\gamma)$, the concentration range $c \in [0.25, 0.75]$ can be sampled. For the first interval $\gamma_1 \leftrightarrow \gamma_2$, the probability is a linear function of the concentration: $p_{1\leftrightarrow 2}(c) = 4c - 1$ with $p_{1\leftrightarrow 2}(0.25) = 0$ and $p_{1\leftrightarrow 2}(0.5) = 1$. For the second interval $\gamma_2 \leftrightarrow \gamma_3$, the slope of the concentration dependent probability function is negative: $p_{2\leftrightarrow 3}(c) = 3 - 4c$ with $p_{2\leftrightarrow 3}(0.5) = 1$ and $p_{2\leftrightarrow 3}(0.75) = 0$. At $c = 0.5$, the probabilities are the same for both functions.

γc_s , $s = 1, \ldots, N_{\text{sub}}$		c	structure	$P(\gamma)$
1	1 0 0 0 0 1 0 0	0.25	$L1_1^+$	$1 - p_{1\leftrightarrow 2}(c)$
2	1 0 0 0 0 1 1 1	0.5	$L1_1$	$p_{1\leftrightarrow 2}(c)$
3	0 1 1 1 0 1 1 1	0.75	$L1_2$	$1 - p_{2\leftrightarrow 3}(c)$

to recover LRO results when only one, periodically repeating configuration occurs with probability one. On the other hand, single-site results are also reproduced when a fully uncorrelated probability distribution

$$P(\gamma) = \prod_{I,s}^{N_c;N_{\text{sub}}} c_{I,s}\,, \text{ with } c_{I,s} = \begin{cases} c & \text{if Ag occupies sublattice } s \text{ in } \gamma \\ 1-c & \text{if Pd occupies sublattice } s \text{ in } \gamma \end{cases} \tag{6.6}$$

with I clusters in the reciprocal space and s sublattices is used instead. The concentrations $c_{I,s}$ are related to the total concentration of Ag c, e.g., $P_{\alpha=0}(\text{Ag Ag Ag Ag}) = c^4$ or $P_{\alpha=0}(\text{Ag Ag Pd Pd}) = c^2(1-c)^2$. Intermediate scenarios and different forms of SRO can also be set up by properly tuning such statistics [94, 147] .

As a preliminary validation step, the concentration interval $c \in [0.25, 0.75]$ of figure 6.9 is considered with the MS-NL-CPA. In particular for $c \in [0.25, 0.5]$, the calculation is restricted to the configurations γ_1 and γ_2, and for $c \in [0.5, 0.75]$ the configurations γ_2 and γ_3, with probabilities given in table 6.3. Thereby, configurations γ_1 to γ_3 correspond to $L1_1^+$, $L1_1$, or $L1_2$. Similarly to the previous LRO calculation setup of section 6.2.2, a set of 6 sites ($\boldsymbol{a}_1, \ldots \boldsymbol{a}_6$), and 4 sites ($\boldsymbol{a}_5, \ldots \boldsymbol{a}_8$) is kept periodically repeated when going from γ_1 to γ_2 and from γ_2 to γ_3, respectively (see table 6.3). The agreement in the corresponding effective medium observables is then indeed recovered, at the level of the resulting bulk modulus, for the Bloch spectral function and for the SRO parameter.

The previous assumptions for the MS-NL-CPA were now expanded and the gradual collapse of the above LRO structures into a fully disordered scenario was studied only with respect to variations in the BSF. Using the MS-NL-CPA within the $N_{\text{sub}} = 8$ supercell did not allow to determine equilibrium properties within a reasonable computation time. The proposed ordered structures for Ag_cPd_{1-c} are locally realized in different orientations modeling the appearance of different domains of the same basic lattice structure. According to this model, the configuration γ_1 in table 6.3 associated with a $L1_1^+$ arrangement may branch into 4 locally equivalent orientations $\gamma_{1a}, \ldots, \gamma_{1d}$, each occurring with the same probability. The same approach is also applied to the case of the γ_2 configuration for the $L1_1$ structure and the γ_3 configuration for the $L1_2$ structure (see table 6.4).

Table 6.4: MS-NL-CPA configurations for the inclusion of SRO in the $c \in [0.25, 0.5]$ and $c \in [0.5, 0.75]$ concentration regimes. The probabilities $p_{1\leftrightarrow 2}$ and $p_{2\leftrightarrow 3}$ are taken from table 6.3.

γ	c_s, $s = 1, \ldots, N_{\text{sub}}$	structure	$P(\gamma)$
1*a*	1 0 0 0 0 1 0 0	$L1^+$ in	$(1 - p_{1\leftrightarrow 2}(c))/4$
1*b*	0 0 0 0 1 1 0 0	its 4 local	$(1 - p_{1\leftrightarrow 2}(c))/4$
1*c*	1 1 0 0 0 0 0 0	permutations	$(1 - p_{1\leftrightarrow 2}(c))/4$
1*d*	0 1 0 0 1 0 0 0	...	$(1 - p_{1\leftrightarrow 2}(c))/4$
2*a*	1 0 0 0 0 1 1 1	$L1_1$ in	$p_{1\leftrightarrow 2}(c)/8$
2*b*	0 1 0 0 1 0 1 1	its 8 local	$p_{1\leftrightarrow 2}(c)/8$
2*c*	0 0 1 0 1 1 0 1	permutations	$p_{1\leftrightarrow 2}(c)/8$
2*d*	0 0 0 1 1 1 1 0	...	$p_{1\leftrightarrow 2}(c)/8$
2*e*	1 1 1 0 0 0 0 1	...	$p_{1\leftrightarrow 2}(c)/8$
2*f*	1 1 0 1 0 0 1 0	...	$p_{1\leftrightarrow 2}(c)/8$
2*g*	1 0 1 1 0 1 0 0	...	$p_{1\leftrightarrow 2}(c)/8$
2*h*	0 1 1 1 1 0 0 0	...	$p_{1\leftrightarrow 2}(c)/8$
3*a*	0 1 1 1 0 1 1 1	$L1_2$ in	$(1 - p_{2\leftrightarrow 3}(c))/4$
3*b*	1 0 1 1 1 0 1 1	its 4 local	$(1 - p_{2\leftrightarrow 3}(c))/4$
3*c*	1 1 0 1 1 1 0 1	permutations	$(1 - p_{2\leftrightarrow 3}(c))/4$
3*d*	1 1 1 0 1 1 1 0	...	$(1 - p_{2\leftrightarrow 3}(c))/4$

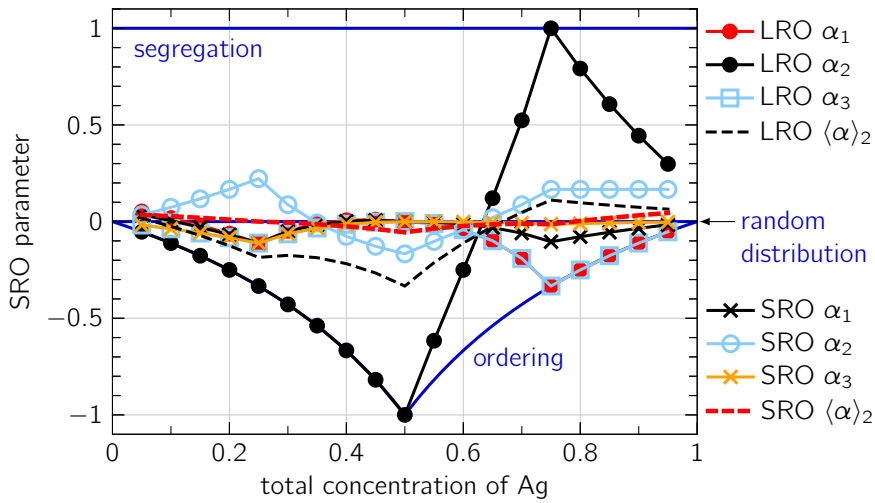

Figure 6.10: The shell dependent SRO parameter with the MS-NL-CPA for the SRO regime with configurations given in table 6.4 as a function of the total concentration. The blue lines show the limits of the SRO parameter, ordering, random distribution or segregation.

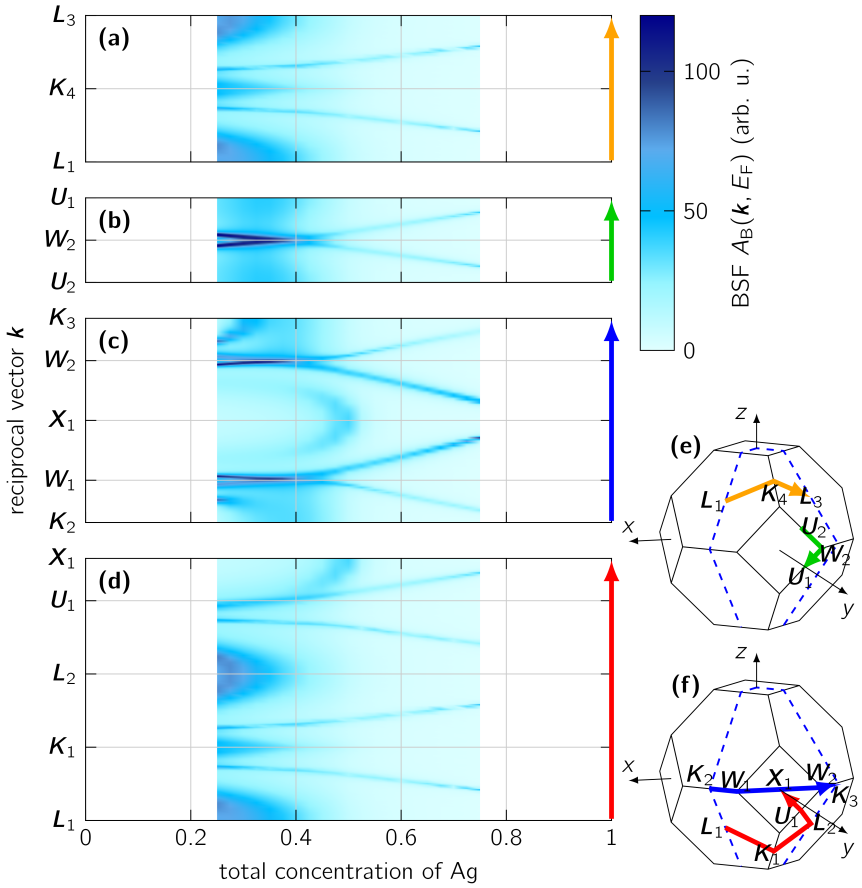

Figure 6.11: Bloch spectral function at the Fermi energy along the same paths as in figure 6.9, restricted to the concentration range $c \in [0.25, 0.75]$. The SRO is defined by a restriction to the configurations listed in table 6.4.

For these configurations, the six step definition of the SRO parameter within the MS-NL-CPA described section 3.4.5 was used and showed clearly the intended reduction of the LRO towards $\alpha = 0$ (see figure 6.10). For example, the ordering tendencies of $L1_2$, visible in α_1, or of $L1_1$, visible in $\langle\alpha\rangle_2$, are strongly reduced and practically vanish in higher coordination numbers. On the contrary, the different permutations in the $L1_1^+$ structure were ill-chosen, since the SRO parameters for concentrations around $c = 0.25$ exhibit still a stronger periodicity and α_3, α_4, ... do not vanish (see figure 6.10).

With this SRO setup, the BSF as a function of the total concentration shows a degree of softening in all the Fermi surface features when compared with the results of the LRO setup (see figure 6.11). This occurs on the one hand side for the Pd-rich portion of the phase diagram. The previously nonequivalent high symmetry points $\boldsymbol{L}_1$, $\boldsymbol{K}_1$, and $\boldsymbol{W}_1$ begin to recover the degeneracy of the fcc lattice across the respective $\boldsymbol{K}_2$, $\boldsymbol{K}_3$ anisotropic instances. This range is particularly dominated by the d states crossing the Brillouin zone and causing strong variations. While taking into account the SRO, it shows traces in the BSF similar as obtained in the fully uncorrelated scenario. At the $\boldsymbol{X}_1$ point for instance, the merging of two BSF branches around $c \approx 0.45$ hints towards the corresponding topology already probed in the evaluation of figure 6.8. The development of the corresponding

single-site features from the LRO starting point can be traced in the neighborhood of the $\boldsymbol{L}_1$ point, this time with a more spread out appearance. For example, a bifurcation in $A_{\mathrm{B}}^{\mathrm{ES}}$, originally observed around $c = 0.4$ at the $\boldsymbol{L}_1$ point, remains unresolved in the SRO setup all the way down to $c = 0.25$. The sharp structure at the $\boldsymbol{W}_1$ point also undergoes similar modifications. On the other hand side, the region for $c > 0.5$ concentrations leads to only minor differences in features at the Fermi energy in all the different single-site CPA, LRO and SRO regimes (figures 6.8, 6.9 and 6.11), since the crossing *sp* band structure for the two elements remains similar.

Conclusions The three considered ordering regimes for the $\mathrm{Ag}_c\mathrm{Pd}_{1-c}$ alloy show significant differences in the equilibrium lattice constant, the bulk modulus and the electronic connectivity in respect of varying chemical composition. The correlation between the equilibrium properties and the electronic structure was verified for the extremal ordering cases, totally random distribution, or assumed LRO, both modeled with the CPA within a unit or a supercell. The comparison of both yielded small variations in the bulk modulus of few GPa but also a qualitative change around $c = 0.6$.

In particular, the single SRO step in between two extremal ordering regimes exhibited substantial features of both of them. Unfortunately, the unit cell of $N_{\mathrm{sub}} = 8$ was too large for additional investigations and distinct steps of short-range order. The determined SRO parameter was only a consequence of its definition, the choice of the structure and the chosen parameter set for the probabilities $P(\gamma_i)$. Although the usage of these parameters is an unsatisfactory concept with respect to the desired first-principle method, but it allows a quantitative estimation of the different degrees of SRO.

6.4. Varying explicitly the SRO parameter

In order to study the effect of SRO more quantitatively, not the probabilities but the SRO parameter itself should be explicitly varied. Then, the influence of the SRO parameter on different physical quantities can be traced. It is demonstrated hereinafter for the DOS calculated for $\mathrm{Ag}_c\mathrm{Pd}_{1-c}$ at the concentrations $c = 0.25$, 0.5 and 0.75 where ordered structures were previously proposed [24].

6.4.1. Coarse screening of the configuration probabilities

However, particular configurations and their probabilities were still needed as input for the MS-NL-CPA calculations but they would be determined by the desired value for the SRO parameter. This concept for the determination of the probabilities was only discussed for a very simple example in section 3.4.5. Therein, the probability of all configurations γ_i was coarse screened from 0 to 1 in steps of 0.05 and the SRO parameter was obtained. Hence, it is not possible to consider all 256 possible configurations of the previous supercell, which included 8 sublattices. The number of possible configurations γ_i to occupy the sublattices either with Ag or Pd atoms was drastically reduced to 16, by using a simple cubic unit cell with $N_{\mathrm{sub}} = 4$ sublattices to resemble the fcc lattice. Nevertheless, this cell still allowed a certain complexity of SRO scenarios.

Table 6.5: All 16 possibilities for the occupation of $N_{\text{sub}} = 4$ sublattices in fcc $\text{Ag}_c\text{Pd}_{1-c}$. The configurations are grouped according to the Ag occupation number operator $\widehat{N}_{\text{Ag}}$ and a new probability $\tilde{P}(\widehat{N}_{\text{Ag}})$ is defined.

configurations				c_{Ag}	c_{Pd}	
Ag	Ag	Ag	Ag	1	0	$\tilde{P}(4)$
Ag	Ag	Ag	Pd	3/4	1/4	$\tilde{P}(3)$
Ag	Ag	Pd	Ag	3/4	1/4	
Ag	Pd	Ag	Ag	3/4	1/4	
Pd	Ag	Ag	Ag	3/4	1/4	
Ag	Ag	Pd	Pd	1/2	1/2	$\tilde{P}(2)$
Ag	Pd	Ag	Pd	1/2	1/2	
Ag	Pd	Pd	Ag	1/2	1/2	
Pd	Ag	Ag	Pd	1/2	1/2	
Pd	Ag	Pd	Ag	1/2	1/2	
Pd	Pd	Ag	Ag	1/2	1/2	
Ag	Pd	Pd	Pd	1/4	3/4	$\tilde{P}(1)$
Pd	Ag	Pd	Pd	1/4	3/4	
Pd	Pd	Ag	Pd	1/4	3/4	
Pd	Pd	Pd	Ag	1/4	3/4	
Pd	Pd	Pd	Pd	0	1	$\tilde{P}(0)$

The coarse screening of the probability parameter space for 16 different $P(\gamma_i)$ presented still a large computational task. For a further reduction, the configurations γ_i were grouped according to the same number of Ag or Pd atoms (see table 6.5). This is possible, since all 4 fcc sublattices have the same interatomic distance and the configurations with the same occupation possess rotation symmetry. The 16 configurations could be sorted into 5 groups, with a new probability $\tilde{P}$, with different Ag and Pd concentrations. A variation of probabilities inside one of those groups does not influence the total concentration (6.1). Hence, the redefined probabilities $\tilde{P}(\widehat{N}_{\text{Ag}})$ formed a similar system of equations as (3.152) to (3.154)

$$\tilde{P}(4) + 3/4\tilde{P}(3) + 1/2\tilde{P}(2) + 1/4\tilde{P}(1) = c\,, \tag{6.7}$$

$$1/4\tilde{P}(3) + 1/2\tilde{P}(2) + 3/4\tilde{P}(1) + \tilde{P}(0) = 1 - c\,, \tag{6.8}$$

$$\sum_i^4 \tilde{P}(i) = 1\,, \tag{6.9}$$

$$0 \leq \tilde{P}(i) \leq 1\,. \tag{6.10}$$

In particular for $c = 0.5$, the system of equations has two solutions.[1] The simple solution

$$\tilde{P}(0) = \frac{1 - \tilde{P}(2)}{3}\,, \tag{6.11}$$
$$\tilde{P}(1) = \tilde{P}(4) = 0\,, \tag{6.12}$$
$$\tilde{P}(3) = 2/3\,, \tag{6.13}$$

has only $0 \leq \tilde{P}(2) \leq 1$ as a free parameter, while the second solution exhibits a larger parameter space, spanned by $\tilde{P}(2)$, $\tilde{P}(3)$, and $\tilde{P}(4)$, but is restricted by the condition

$$\begin{aligned}&\big(2\tilde{P}(2) + 3\tilde{P}(3) + 4\tilde{P}(4) \leq 2\big) \wedge \\ &\qquad \Big\{ \big[\big(\tilde{P}(2) + 2\tilde{P}(3) + 3\tilde{P}(4) \geq 1\big) \wedge \big(\tilde{P}(2) + 2\tilde{P}(3) \leq 1\big)\big] \vee \\ &\qquad\qquad \big[\big(\tilde{P}(2) + 2\tilde{P}(3) \geq 1\big) \wedge \big(2\tilde{P}(2) + 3\tilde{P}(3) \leq 2\big)\big] \Big\}\,. \end{aligned} \tag{6.14}$$

The remaining probabilities are then given by

$$\tilde{P}(0) = \tilde{P}(2) + 2\tilde{P}(3) + 3\tilde{P}(4) - 1\,, \tag{6.15}$$
$$\tilde{P}(1) = 2 - 2\tilde{P}(2) - 3\tilde{P}(3) - 4\tilde{P}(4)\,. \tag{6.16}$$

A similar solution was found for the other concentrations $c = 0.25$ and 0.75 (see appendix B.2).

6.4.2. Calculation details

In order to reduce the computational load even more, only one configuration for every concentration group with $\tilde{P}(\widehat{N}_{\mathrm{Ag}})$ was considered, namely

$$\begin{aligned}
&\tilde{P}(4) \to \gamma_1 = \mathrm{Ag\ Ag\ Ag\ Ag}\,. \\
&\tilde{P}(3) \to \gamma_2 = \mathrm{Ag\ Ag\ Ag\ Pd}\,, \\
&\tilde{P}(2) \to \gamma_6 = \mathrm{Ag\ Ag\ Pd\ Pd}\,, \\
&\tilde{P}(1) \to \gamma_{12} = \mathrm{Ag\ Pd\ Pd\ Pd}\,, \\
&\tilde{P}(0) \to \gamma_{16} = \mathrm{Pd\ Pd\ Pd\ Pd}\,.
\end{aligned} \tag{6.17}$$

Thereby, not all probabilities were free to chose In particular, $\tilde{P}(0)$ and $\tilde{P}(1)$ were determined for $c = 0.5$ by $\tilde{P}(2)$, $\tilde{P}(3)$, and $\tilde{P}(4)$ via (6.15) and (6.16) and under the condition (6.14). The probabilities for the other two concentrations were obtained similarly by (B.1) to (B.3) and (B.7) to (B.9) for $c = 0.25$ or 0.75.

The values $\tilde{P}(2)$, $\tilde{P}(3)$, and $\tilde{P}(4)$ form a probability space, which was sampled in steps of 0.05. Then, the corresponding SRO parameter α_1 was calculated at each step with the configurations and $\tilde{P}(0)$ to $\tilde{P}(4)$ (not shown). Finally, few representative values were chosen from the large sets of calculated SRO parameters. The chosen α_1 for $c = 0.25$, 0.5,

[1] Solved with *Mathematica*.

Table 6.6: Experimental binding energies (in eV, relative to the Fermi energy) of the main spectral peaks estimated from the experimental (He II) spectra by McLachlan *et al.* [148] and interpolated to the concentrations used in the present calculations. Values in parenthesis refer to the scaled values E^{scaled} in (C.1). The upper two rows are for the Pd 4*d* section of the spectrum and the lower two rows belong to the Ag 4*d* section.

$Ag_{0.25}Pd_{0.75}$		$Ag_{0.50}Pd_{0.50}$		$Ag_{0.75}Pd_{0.25}$	
0.5	(0.5)	1.0	(1.0)	1.4	(1.5)
2.4	(2.5)	2.3	(2.4)	–	(–)
4.9	(3.9)	4.6	(3.5)	4.4	(3.3)
5.5	(4.6)	5.7	(4.9)	6.0	(5.3)

and 0.75 are presented together with the corresponding configurations and probabilities in the tables 6.7, 6.8, and 6.9, respectively. The data of the tables served as input for self-consistent calculation with the MS-NL-CPA within the GF method, and the density of states was calculated. The principle calculation setup and the lattice constants remained the same as described before in section 6.1 for the previous calculations of the Ag_cPd_{1-c} alloy. Only the expansion cut-off and the number of $\boldsymbol{k}$ points could be reduced to $l_{\text{max}} = 3$ and $20 \times 20 \times 20$ for the $N_{\text{sub}} = 4$ supercell, since the calculation results for the electronic properties converge much faster with l_{max} and k_{mesh} than for the equilibrium properties.

6.4.3. DOS compared with experimental binding energies

The calculated valence DOS of the Ag_cPd_{1-c} alloys for $c = 0.25, 0.50, 0.75$ in dependence of the nearest neighbor SRO parameter α_1 are presented in figures 6.12, 6.13 and 6.14, respectively. The three figures show significant changes in the DOS with varying SRO. Some spectral peaks vanish, move or grow. When going from the ordered regime ($\alpha_1 < 0$) via the random distribution ($\alpha_1 = 0$) towards segregation behavior ($\alpha_1 > 0$), the spiky structure of the DOS looses contrast and becomes smoother. Simultaneously, the band width is enhanced with increasing α_1.

The restriction to only the nearest neighbor SRO parameter α_1 followed again from the periodicity of the chosen cubic cell. The $N_{\text{sub}} = 4$ sublattices were always nearest neighbors. Also, they were the only ones, which were influenced by the different SRO configurations. The next nearest neighbor sublattices in the cubic cell suffer already from the underlying periodicity, hosting always the same type of atom, which is occupying also the actual origin. Hence, α_2 will include already traces of the periodic lattice. The same issue was already discussed in the context of the extended supercell in section 6.2.2. A comparison of SRO regimes within a particular structure model remained reasonable but other structures like the ordered phases $L1_1^+$ or $L1_1$ could not be sufficiently described in the small cubic unit cell with $N_{\text{sub}} = 4$. However, the averaged SRO parameters $\langle\alpha\rangle_2$ or $\langle\alpha\rangle_3$ were used for the qualitative comparison between $L1_1^+$ or $L1_1$ and the other SRO configurations further below.

In addition, the DOS for different SRO regimes were compared with the experimental

Table 6.7: Nearest neighbor SRO parameter and the corresponding configurations used for fcc $Ag_{0.25}Pd_{0.75}$ with $N_{sub} = 4$. For $\alpha = 0$, all 16 configurations are used and their probabilities are given by (6.6).

γ_i	configurations	c_{Ag}	Probabilities $P(\gamma_i)$ for $\alpha_1 =$ $-1/3$	-0.201	-0.141	-0.095	$-1/12$	-0.04	0.099	$1/4$
1	Ag Ag Ag Ag	1	0	0	0.05	0.05	0	0.1	0.15	1/4
2	Ag Ag Ag Pd	3/4	0	0.05	0	0.05	0	0	0	0
3	Ag Ag Pd Pd	1/2	0	0.05	0.05	0	1/6	0	0.05	0
4	Ag Pd Pd Pd	1/4	1	3/4	0.7	0.65	1/4	0.6	0.3	0
5	Pd Ag Pd Pd	1/4	0	0	0	0	1/4	0	0	0
6	Pd Pd Ag Pd	1/4	0	0	0	0	1/4	0	0	0
7	Pd Pd Pd Ag	1/4	0	0	0	0	1/4	0	0	0
8	Pd Pd Pd Pd	0	0	0.15	0.2	1/4	0	0.3	1/2	3/4

valence band PES of Ag-Pd alloys measured by McLachlan *et al.* [148]. The experimental He II (40.81 eV) spectrum was particularly preferred as it is found to better represent initial state effects in comparison to the He I (21.22 eV) spectrum. Although the He II technique is in general rather surface sensitive, its application to metals with a highly efficient screening mechanism can lead to useful insights on bulk properties from analysis of the surveying signal. This is further confirmed by comparison of the specific He II results used in this study against the experimental XPS spectra of Hüfner *et al.* [149], where the measured probing depth was reported to be about 50 Å [150], thus including

Table 6.8: Nearest neighbor SRO parameter and the corresponding configurations used for fcc $Ag_{0.5}Pd_{0.5}$ with $N_{sub} = 4$. For $\alpha = 0$, all 16 configurations are used and their probabilities are given by (6.6).

γ_i	configurations	c_{Ag}	Probabilities $P(\gamma_i)$ for $\alpha_1 =$ -0.270[a]	-0.198	-0.140[a]	$-1/12$	-0.04	0.108	$1/4$
1	Ag Ag Ag Ag	1	0	0.1	0	0	0.2	0.3	1/2
2	Ag Ag Ag Pd	3/4	0.05	0	0.15	0	0	0.1	0
3	Ag Ag Pd Ag	3/4	0.05	0	0.15	0	0	0	0
4	Ag Ag Pd Pd	1/2	0.8	0.7	0.5	1/6	0.6	0.2	0
5	Ag Pd Ag Pd	1/2	0	0	0	1/6	0	0	0
6	Ag Pd Pd Ag	1/2	0	0	0	1/6	0	0	0
7	Pd Ag Ag Pd	1/2	0	0	0	1/6	0	0	0
8	Pd Ag Pd Ag	1/2	0	0	0	1/6	0	0	0
9	Pd Pd Ag Ag	1/2	0	0	0	1/6	0	0	0
10	Ag Pd Pd Pd	1/4	0.1	0.2	0.1	0	0	0.1	0
11	Pd Pd Pd Pd	0	0	0	0.1	0	0.2	0.3	1/2

[a] The choice of (6.17) was varied. Instead of one, two configurations with three Ag atoms ($\tilde{P}(3)$) were taken with $P(\gamma_2) = P(\gamma_3) = \tilde{P}(3)/2$.

Table 6.9: Nearest neighbor SRO parameter and the corresponding configurations used for fcc $Ag_{0.75}Pd_{0.25}$ with $N_{sub} = 4$. For $\alpha = 0$, all 16 configurations are used and their probabilities are given by (6.6).

γ_i	configurations	c_{Ag}	Probabilities $P(\gamma_i)$ for $\alpha_1 =$					
			-0.238	-0.141	$-1/12$	-0.04	0.106	$1/4$
1	Ag Ag Ag Ag	1	1	0.2	0	0.3	0.6	3/4
2	Ag Ag Ag Pd	3/4	0.85	0.7	1/4	0.6	0.1	0
3	Ag Ag Pd Ag	3/4	0	0	1/4	0	0	0
4	Ag Pd Ag Ag	3/4	0	0	1/4	0	0	0
5	Pd Ag Ag Ag	3/4	0	0	1/4	0	0	0
6	Ag Ag Pd Pd	1/2	0	0.05	0	0	0.05	0
7	Ag Pd Pd Pd	1/4	0.05	0	0	0	0.2	0
8	Pd Pd Pd Pd	0	0	0.05	0	0.1	0.05	1/4

substantial bulk contributions. The actual binding energies are given in table 6.6. In order to take into account the typical shortcomings of the exchange-correlation functionals, the binding energies were linearly scaled (see appendix C).

However, a direct comparison between the experimental and theoretical results is hardly possible. The binding energies can at least be related with some pronounced peaks in

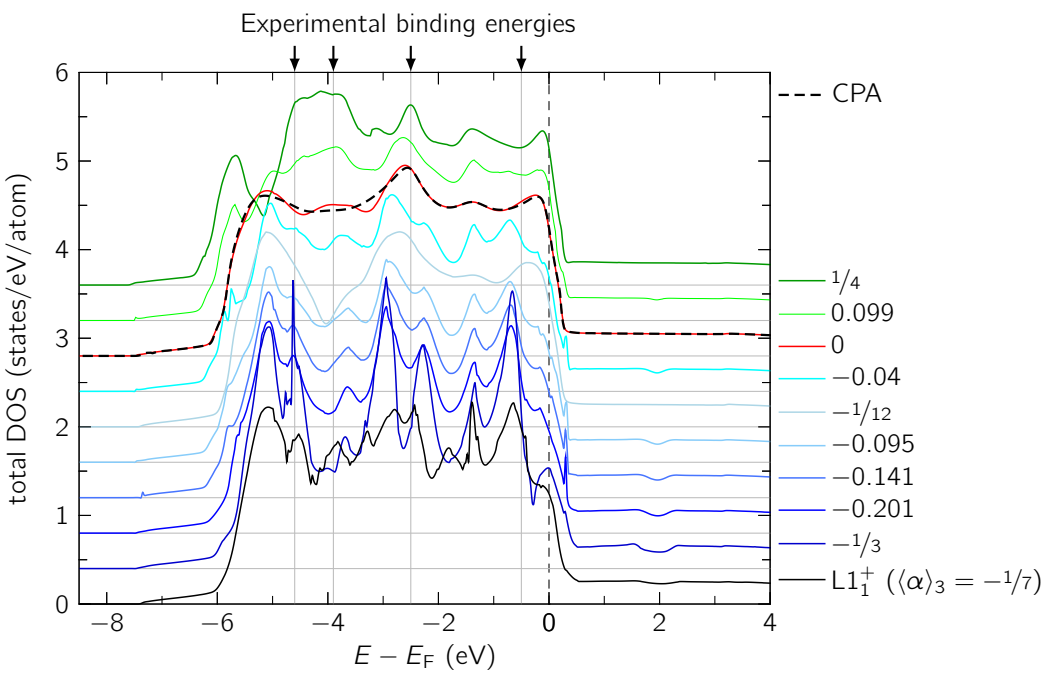

Figure 6.12: Calculated density of states of $Ag_{0.25}Pd_{0.75}$ for different degrees of nearest neighbor SRO α_1, beginning with the ordered $L1_1^+$ structure. The corresponding configurations used for the SRO parameter are given in table 6.7. An offset is added to the curves (horizontal gray line represents zero). The binding energies of the main spectral peaks of the experimental PES (table 6.6) are highlighted by arrows and vertical gray lines.

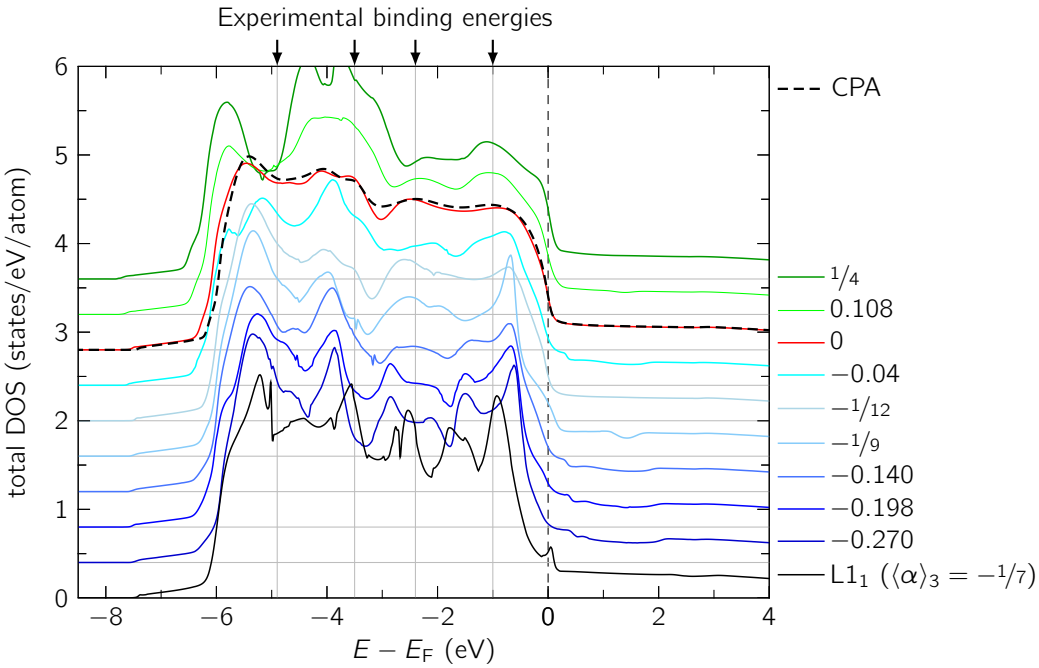

Figure 6.13: Calculated density of states of $Ag_{0.5}Pd_{0.5}$ for different degrees of nearest neighbor SRO α_1, beginning with the ordered $L1_1$ structure. The corresponding configurations used for the SRO parameter are given in table 6.8. An offset is added to the curves (horizontal gray line represents zero). The binding energies of the main spectral peaks of the experimental PES (table 6.6) are highlighted by arrows and vertical gray lines.

the DOS for all three concentrations but the resolution of the older measurements allows only a crude estimation and comparison with the different SRO scenarios. For $Ag_{0.25}Pd_{0.75}$, the best agreement with the scaled binding energies would be achieved with the assumption of the fully uncorrelated disorder $\alpha_1 = 0$ (see figure 6.12). Otherwise, the experiment would not capture all pronounced spectral peaks, e.g., the states at low energies for $\alpha_1 = 1/4$ or the spiky DOS for the ordered structures. Nevertheless, the variation of the amount of SRO in $Ag_{0.25}Pd_{0.75}$ visualizes the gradually collapse or development of several spectral peaks when going from negative to positive α_1. The minimal $\alpha_1 = -1/3$ represents the $L1_2$ structure (Ag at the corners and Pd at the faces of the cube), although $L1_1^+$ was found to be energetically more favorable. The latter structure should be described by an averaged SRO parameter $\langle\alpha\rangle_2 = -5/27 \approx -0.185$ or $\langle\alpha\rangle_3 = -1/7 \approx -0.143$. The different amount of SRO in $L1_2$ or $L1_1^+$ is directly visible in the DOS of both structures. While the DOS of $L1_2$ yielded sharper spectral peaks, the DOS of $L1_1^+$ ranges better between $\alpha_1 = 0.141$ and $\alpha_1 = 0.201$ (see figure 6.12).

The analysis for the DOS of $Ag_{0.5}Pd_{0.5}$ was quite similar as for $Ag_{0.25}Pd_{0.75}$. Several spectral peaks become wider and shift their positions (see figure 6.13). Also for this concentration, the proposed ordered structure $L1_1$ has not the lowest possible SRO parameter (minimum: $\alpha = -1$, for $L1_1$: $\langle\alpha\rangle_2 = -1/3$ or $\langle\alpha\rangle_3 = -1/7$) while its DOS matches rather less with the DOS of the remaining SRO scenarios. It might be that the symmetric cubic cell catches only badly the layered structure of $L1_1$. On the other hand, the experimental binding energies agree again only for $\alpha_1 = 0$ well with the theoretically calculated

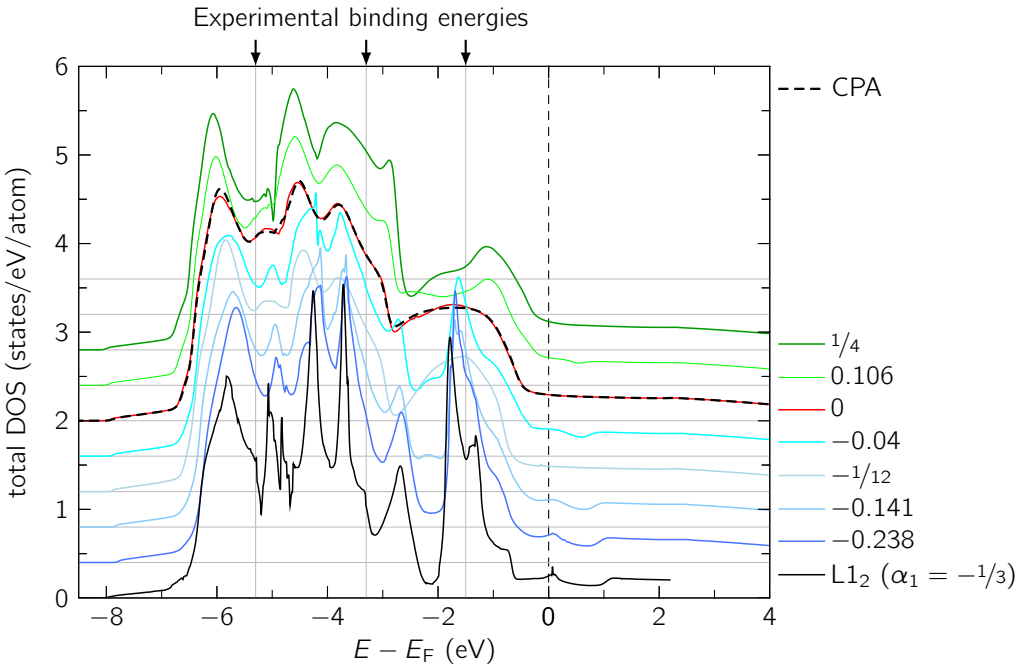

Figure 6.14: Calculated density of states of $Ag_{0.75}Pd_{0.25}$ for different degrees of nearest neighbor SRO α_1, beginning with the ordered $L1_2$ structure. The corresponding configurations used for the SRO parameter are given in table 6.9. An offset is added to the curves (horizontal gray line represents zero). The binding energies of the main spectral peaks of the experimental PES (table 6.6) are highlighted by arrows and vertical gray lines.

number of spectral peaks and their positions.

By further raising the concentration of Ag to $Ag_{0.75}Pd_{0.25}$, the gradually widening of the spectral peaks of the ordered structure $L1_2$ can be traced with the increasing of the SRO parameter (see figure 6.14). $L1_2$ has already the lowest possible SRO parameter and is described well by the small cubic cell. Thus the large peak in $L1_2$ of the Pd $4d$ states close to the Fermi energy loses its height and becomes much broader for $\alpha_1 = 0$. At lower energies, the spectral peaks of the well-structured DOS overlap each other and end up in few broad peaks as well. Hence, the comparison with the experimental binding energies at this concentration $c = 0.75$ is less useful. Their position can not be correlated with the theoretically calculated spectral peak position (see arrows in figure 6.14).

Finally, the calculated DOS at $c = 0.25$, 0.5 and 0.75 were also compared with the PES measurements of Norris and Nilsson [151], Hüfner *et al.* [149, 152], Chae *et al.* [153] and Traditi *et al.* [154]. In general, the experimental spectra agree best with the DOS of the random ($\alpha_1 = 0$) or ordering ($\alpha_1 < 0$) cases, the clustering ($\alpha_1 > 0$) features being less probable. This is in agreement with the complete solubility of Ag and Pd at ambient temperatures and with the ordering tendency at low temperatures [24].

Conclusions The SRO induced changes in the DOS curves are significantly larger than the typical energy resolution in the valence band PES measurements [148]. So, the PES technique can be considered as one potential experimental method to investigate SRO structures of alloys. In particular in combination with first-principle calculations within

the MS-NL-CPA, statements about the local structure and potential SRO could be possible in future investigations.

Chapter 7.

Conclusions

This thesis unites the theoretical discussion of adatoms, vacancies, and substitutional defects, which can be found in materials research, in two or three dimensional systems. The computational method of choice was the Green's function method HUTSEPOT, which performed very well in the description of the magnetic, electronic or equilibrium properties of single adatoms, point defects or larger substitutional disorder. In particular, the underlying multiple scattering theory allowed the efficient self-consistent calculation of the considerably differing characteristics of these defects, if it was either a perfect two-dimensional system with a perturbative cluster, a strongly correlated systems three-dimensional systems or the consideration of local short-range order in an alloy.

The degree of disorder was gradually increased for the Ag_cPd_{1-c} while the defined SRO parameter allowed for a quantitative comparison between the chosen configurations inside a complex unit cell. The variation of specific SRO regimes could be studied through the MS-NL-CPA. The changes in the spectral peaks in the DOS at a certain concentration c act as a fingerprint for a certain amount of SRO and might be compared with experimental photoemission spectra. Unfortunately, the large computational effort of the MS-NL-CPA within HUTSEPOT hinders a more flexible variation of the SRO parameters or the investigation of a broader concentration interval in Ag_cPd_{1-c}. Moreover, the definition of a short-range order parameter is also restricted to a particular lattice structure, since the comparability remains a controversial point.

Once more, the single-site approximation of the CPA proofed to be a reliable tool for the description of various physical observables. The variation of the magnetic properties in dependence of the oxygen-deficiency agreed very well with experimental measurements for the strongly-correlated system $SrCoO_{3-\delta}$, whereas an potential increase of T_C with δ for $Sr_2FeMoO_{6-\delta}$ promise good possibility for applications.

The symmetry-related highly stable magnetic ground state of a single Holmium adatom on top of Pt(111) also shows the great reliability of the GF method. The implemented technique for the calculation the crystal-field parameters yielded precise results, which led to an excellent agreement between the theoretical and experimental excitation spectrum.

Appendix A.

Eigenstates and Eigenvalues of Holmium on Pt(111)

Table A.1: The eigenvalue (energy) and $\widehat{J}_z$ expectation value for all eigenstates $|\Psi_i\rangle$ of the matrix eigenvalue problem (4.14). The eigenstates (4.9) are a linear combination of the pure states $|M\rangle$ with the expansion coefficients given in tables A.2 and A.3.

	Energy	$\langle \widehat{J}_z \rangle$
$\|\Psi_{-8}\rangle$	0	−7.999 94
$\|\Psi_{+8}\rangle$	0	7.999 94
$\|\Psi_{-7}\rangle$	7.706 58	6.999 91
$\|\Psi_{+7}\rangle$	7.706 58	−6.999 91
$\|\Psi^{\mathrm{s}}_{\pm 6}\rangle$	16.3256	0
$\|\Psi^{\mathrm{a}}_{\pm 6}\rangle$	16.3259	0
$\|\Psi_{-5}\rangle$	24.5807	−4.998 76
$\|\Psi_{+5}\rangle$	24.5807	4.998 76
$\|\Psi_{-4}\rangle$	31.7345	−3.989 87
$\|\Psi_{+4}\rangle$	31.7345	3.989 87
$\|\Psi^{\mathrm{s}}_{\pm 3}\rangle$	37.3103	0
$\|\Psi^{\mathrm{a}}_{\pm 3}\rangle$	37.5407	0
$\|\Psi_{-2}\rangle$	41.5095	−1.995 22
$\|\Psi_{+2}\rangle$	41.5095	1.995 22
$\|\Psi_{-1}\rangle$	43.9529	−0.992 87
$\|\Psi_{+1}\rangle$	43.9529	0.992 87
$\|\Psi_{0}\rangle$	44.7654	0

Table A.2: Expansion coefficients in (4.9) for the eigenstates $|\Psi_i\rangle$. Only those for the pure states from $|-8\rangle$ to $|0\rangle$ are shown. It is continued in table A.3.

eigenstates	$\|-8\rangle$	$\|-7\rangle$	$\|-6\rangle$	$\|-5\rangle$	$\|-4\rangle$	$\|-3\rangle$	$\|-2\rangle$	$\|-1\rangle$	$\|0\rangle$
$\|\Psi_{-8}\rangle$	0.999991	0	0	-0.00425	0	0	-0.000523763	0	0
$\|\Psi_{+8}\rangle$	0	4.39443E-8	0	0	1.56819E-6	0	0	-7.09619E-6	0
$\|\Psi_{-7}\rangle$	-7.85693E-8	-0.00242479	0	-5.92356E-6	-2.3492E-6	0	6.1456E-7	2.81973E-6	0
$\|\Psi_{+7}\rangle$	-1.90515E-10	0.999996	0	-1.43635E-8	0.000968821	0	1.49019E-9	-0.00116287	0
$\|\Psi^{s}_{\pm 6}\rangle$	0	0	-0.70707	0	0	-0.00681761	0	0	0.00314227
$\|\Psi^{a}_{\pm 6}\rangle$	0	0	0.707074	0	0	0.00679133	0	0	0
$\|\Psi_{-5}\rangle$	-0.00425954	0	0	-0.999785	0	0	-0.0198267	-1.33991E-9	0
$\|\Psi_{+5}\rangle$	1.31372E-9	-0.0000110167	0	3.08352E-7	0.0000558681	0	6.1149E-9	-0.00434447	0
$\|\Psi_{-4}\rangle$	-1.83568E-7	0.000933148	0	3.92913E-6	-0.999072	0	-0.000306984	-0.0299004	0
$\|\Psi_{+4}\rangle$	6.29826E-6	0.0000271973	0	-0.00013481	-0.0291187	0	0.0105327	-0.000871469	0
$\|\Psi^{s}_{\pm 3}\rangle$	0	0	-0.00669111	0	0	0.706093	0	0	0.0526898
$\|\Psi^{a}_{\pm 3}\rangle$	0	0	-0.00679133	0	0	0.707074	0	0	0
$\|\Psi_{-2}\rangle$	-0.000439442	-2.42954E-9	0	0.0196308	4.7569E-7	0	-0.998886	-1.66756E-6	0
$\|\Psi_{+2}\rangle$	1.77633E-8	-0.0000601039	0	-7.93524E-7	0.011768	0	0.0000403774	-0.0412535	0
$\|\Psi_{-1}\rangle$	3.25595E-7	-0.00118851	0	-0.000243101	0.0294171	0	0.00195315	-0.997584	0
$\|\Psi_{+1}\rangle$	6.90896E-6	0.0000560103	0	-0.00515848	-0.00138632	0	0.0414449	0.0470126	0
$\|\Psi_{0}\rangle$	0	0	-0.00257796	0	0	0.0372344	0	0	-0.998606

Table A.3: Continuation from table A.2. Expansion coefficients in (4.9) for the eigenstates $|\Psi_i\rangle$. Only those for the pure states from $|1\rangle$ to $|8\rangle$ are shown.

eigenstates	$\|1\rangle$	$\|2\rangle$	$\|3\rangle$	$\|4\rangle$	$\|5\rangle$	$\|6\rangle$	$\|7\rangle$	$\|8\rangle$
$\|\Psi_{-8}\rangle$	7.09619E-6	0	0	1.56819E-6	0	0	-4.39442E-8	0
$\|\Psi_{+8}\rangle$	0	-0.000523763	0	0	0.00425	0	0	0.999991
$\|\Psi_{-7}\rangle$	0.00116287	-1.49019E-9	0	0.000968821	-1.43635E-8	0	-0.999996	1.90515E-10
$\|\Psi_{+7}\rangle$	2.81973E-6	6.1456E-7	0	2.3492E-6	5.92356E-6	0	-0.00242479	-7.85693E-8
$\|\Psi^{s}_{\pm 6}\rangle$	0	0	0.00681761	0	0	-0.70707	0	0
$\|\Psi^{a}_{\pm 6}\rangle$	0	0	0.00679133	0	0	-0.707074	0	0
$\|\Psi_{-5}\rangle$	0.00434447	-6.1149E-9	0	0.0000558681	3.08352E-7	0	0.0000110167	-1.31372E-9
$\|\Psi_{+5}\rangle$	-1.33991E-9	-0.0198267	0	0	0.999785	0	0	-0.00425954
$\|\Psi_{-4}\rangle$	-0.000871469	0.0105327	0	0.0291187	0.00013481	0	0.0000271973	6.29826E-6
$\|\Psi_{+4}\rangle$	0.0299004	0.000306984	0	-0.999072	3.92913E-6	0	-0.000933148	1.83568E-7
$\|\Psi^{s}_{\pm 3}\rangle$	0	0	-0.706093	0	0	-0.00669111	0	0
$\|\Psi^{a}_{\pm 3}\rangle$	0	0	0.707074	0	0	0.00679133	0	0
$\|\Psi_{-2}\rangle$	-0.0412535	0.0000403774	0	-0.011768	7.93524E-7	0	-0.0000601039E	1.77633E-8
$\|\Psi_{+2}\rangle$	1.66756E-6	0.998886	0	4.7569E-7	0.0196308	0	2.42954E-9	0.000439442
$\|\Psi_{-1}\rangle$	-0.0470126	-0.0414449	0	-0.00138632	-0.00515848	0	-0.0000560103E	-6.90896E-6
$\|\Psi_{+1}\rangle$	-0.997584	0.00195315	0	-0.0294171	0.000243101	0	-0.00118851	3.25595E-7
$\|\Psi_{0}\rangle$	0	0	-0.0372344	0	0	-0.00257796	0	0

Appendix B.

SRO Parameters for the AgPd Alloy

B.1. The smallest cell with two sublattices

Table B.1: Comparison of nearest neighbor SRO parameter for $N_{\text{sub}} = 2$, $c = 0.5$ and varied probabilities $P(\gamma_i)$ in steps of 0.05 (under the restrictions imposed by (3.137) to (3.139)). All entries, except those marked with 1 in the first column, are symmetric in the γ_2 and γ_3 configurations.

	probability P of					
sym	γ_1	γ_2	γ_3	γ_4	α_1	α_1^{stat}
1	0	0.5	0.5	0	−0.083 333	−0.083 620
	0	0.45	0.55	0	−0.082 500	−0.082 255
	0	0.4	0.6	0	−0.08	−0.080 198
	0	0.35	0.65	0	−0.075 833	−0.075 838
	0	0.3	0.7	0	−0.07	−0.070 104
1	0.05	0.45	0.45	0.05	−0.066 667	−0.066 253
	0.05	0.4	0.5	0.05	−0.065 833	−0.065 702
	0.05	0.35	0.55	0.05	−0.063 333	−0.062 928
	0	0.25	0.75	0	−0.062 500	−0.062 276
	0.05	0.3	0.6	0.05	−0.059 167	−0.059 450
	0.05	0.25	0.65	0.05	−0.053 333	−0.053 132
	0	0.2	0.8	0	−0.053 333	−0.053 164
1	0.1	0.4	0.4	0.1	−0.05	−0.050 256
	0.1	0.35	0.45	0.1	−0.049 167	−0.048 601
	0.1	0.3	0.5	0.1	−0.046 667	−0.046 341
	0.05	0.2	0.7	0.05	−0.045 833	−0.045 708
	0.1	0.25	0.55	0.1	−0.042 500	−0.042 553
	0	0.15	0.85	0	−0.042 500	−0.042 341
	0.1	0.2	0.6	0.1	−0.036 667	−0.036 489
	0.05	0.15	0.75	0.05	−0.036 667	−0.036 285
1	0.15	0.35	0.35	0.15	−0.033 333	−0.033 167
	0.15	0.3	0.4	0.15	−0.032 500	−0.032 898
	0.15	0.25	0.45	0.15	−0.03	−0.029 547
	0	0.1	0.9	0	−0.03	−0.029 815
	0.1	0.15	0.65	0.1	−0.029 167	−0.029 341

Table B.1: (continued)

sym	probability P of γ_1	γ_2	γ_3	γ_4	α_1	α_1^{stat}
	0.15	0.2	0.5	0.15	−0.025 833	−0.026 011
	0.05	0.1	0.8	0.05	−0.025 833	−0.025 836
	0.15	0.15	0.55	0.15	−0.02	−0.020 340
	0.1	0.1	0.7	0.1	−0.02	−0.020 215
1	0.2	0.3	0.3	0.2	−0.016 667	−0.017 211
	0.2	0.25	0.35	0.2	−0.015 833	−0.015 807
	0	0.05	0.95	0	−0.015 833	−0.015 739
	0.05	0.05	0.85	0.05	−0.013 333	−0.013 372
	0.2	0.2	0.4	0.2	−0.013 333	−0.012 689
	0.15	0.1	0.6	0.15	−0.012 500	−0.012 662
	0.2	0.15	0.45	0.2	−0.009 167	−0.009 296
	0.1	0.05	0.75	0.1	−0.009 167	−0.009 242
	0.2	0.1	0.5	0.2	−0.003 333	−0.003 747
	0.15	0.05	0.65	0.15	−0.003 333	−0.003 476
	0	0	1	0	0	0
1	0.25	0.25	0.25	0.25	0	−0.000 026
	0.05	0	0.9	0.05	0.000 833	0.000 871
	0.25	0.2	0.3	0.25	0.000 833	0.000 736
	0.25	0.15	0.35	0.25	0.003 333	0.003 662
	0.1	0	0.8	0.1	0.003 333	0.003 394
	0.2	0.05	0.55	0.2	0.004 167	0.004 309
	0.25	0.1	0.4	0.25	0.007 500	0.007 198
	0.15	0	0.7	0.15	0.007 500	0.007 157
	0.25	0.05	0.45	0.25	0.013 333	0.013 357
	0.2	0	0.6	0.2	0.013 333	0.012 946
1	0.3	0.2	0.2	0.3	0.016 667	0.016 826
	0.3	0.15	0.25	0.3	0.017 500	0.017 117
	0.3	0.1	0.3	0.3	0.02	0.019 303
	0.25	0	0.5	0.25	0.020 833	0.021 144
	0.3	0.05	0.35	0.3	0.024 167	0.024 214
	0.3	0	0.4	0.3	0.03	0.029 823
1	0.35	0.15	0.15	0.35	0.033 333	0.033 096
	0.35	0.1	0.2	0.35	0.034 167	0.034 065
	0.35	0.05	0.25	0.35	0.036 667	0.036 254
	0.35	0	0.3	0.35	0.040 833	0.040 981
1	0.4	0.1	0.1	0.4	0.05	0.049 905
	0.4	0.05	0.15	0.4	0.050 833	0.050 902
	0.4	0	0.2	0.4	0.053 333	0.053 457
1	0.45	0.05	0.05	0.45	0.066 667	0.067 142
	0.45	0	0.1	0.45	0.067 500	0.067 752
1	0.5	0	0	0.5	0.083 333	0.083 534

B.2. Probability relations

By using the same system of equation (6.7) to (6.7), the probability relations for the concentrations $c = 0.25$ and 0.75 were found as done in section 6.4.1. Varying $\tilde{P}(2)$, $\tilde{P}(3)$ and $\tilde{P}(4)$ yields for $c = 0.25$

$$\tilde{P}(0) = \tilde{P}(2) + 2\tilde{P}(3) + 3\tilde{P}(4)\,, \tag{B.1}$$
$$\tilde{P}(1) = 1 - 2\tilde{P}(2) - 3\tilde{P}(3) - 4\tilde{P}(4)\,, \tag{B.2}$$

as long as

$$\left(2\tilde{P}(2) + \tilde{P}(3) \leq 1\right) \wedge \left(2\tilde{P}(2) + 3\tilde{P}(3) + 4\tilde{P}(4) \leq 1\right). \tag{B.3}$$

A simpler solution is

$$\tilde{P}(0) = \frac{(2 - \tilde{P}(2))}{3}\,, \tag{B.4}$$
$$\tilde{P}(3) = \frac{(1 - 2\tilde{P}(2))}{3}\,, \tag{B.5}$$

while

$$\tilde{P}(1) = 0\,,\ 0 \leq \tilde{P}(2) \leq 1/2\,,\ \tilde{P}(4) = 0\,. \tag{B.6}$$

On the other hand, the solution of the system of equations for $c_{\mathrm{Ag}} = 0.75$ is

$$\tilde{P}(0) = \tilde{P}(2) + 2\tilde{P}(3) + 3\tilde{P}(4) - 2\,, \tag{B.7}$$
$$\tilde{P}(1) = 3 - 2\tilde{P}(2) - 3\tilde{P}(3) - 4\tilde{P}(4)\,, \tag{B.8}$$

while

$$\left(2\tilde{P}(2) + \tilde{P}(3) \leq 1\right) \wedge \left(\tilde{P}(2) + 2\tilde{P}(3) + 3\tilde{P}(4) \geq 2\right) \wedge \left(2\tilde{P}(2) + 3\tilde{P}(3) + 4\tilde{P}(4) \leq 3\right). \tag{B.9}$$

A simpler solution is

$$\tilde{P}(0) = 0\,,\ \tilde{P}(1) = 0\,,\ 0 \leq \tilde{P}(2) \leq 1/2\,,\ \tilde{P}(3) = 1 - \tilde{P}(2)\,,\ \tilde{P}(4) = \tilde{P}(2)\,. \tag{B.10}$$

Appendix C.

Scaling of the Experimental Energies

Since DFT calculations based on LDA or GGA and beyond exchange-correlation functionals are commonly affected by imperfect prediction of band widths and absolute placement of energy levels, the comparison between calculated and experimental results can be improved by using a scaling function between the theoretical and experimental reference data.

For the comparison of the DOS with the experimental references in section 6.4, the band width of pure Ag and Pd was taken as a reference, and the following linear scaling function was used

$$E^{\text{scaled}} = E\left[\frac{E - E_{\text{b}}^{X}}{E_{\text{t}}^{X} - E_{\text{b}}^{X}}\beta_{\text{t}}^{X} + \left(1 - \frac{E - E_{\text{b}}^{X}}{E_{\text{t}}^{X} - E_{\text{b}}^{X}}\right)\beta_{\text{b}}^{X}\right], \tag{C.1}$$

where E_{t}^{X} and E_{b}^{X} denote the experimental binding energies of the top and bottom of the d band of a pure element X (=Ag or Pd), and β_i^X ($= E_i^{X,\text{calc}}/E_i^{X,\text{exp}}$) is the ratio between calculated and experimental values for the top and bottom of the same band. Following McLachlan *et al.* [148], the parameters of table C.1 were used in the scaling function (C.1).

Table C.1: Parameters of pure Ag and Pd used in (C.1).

X	E_{b}^{X} (eV)	E_{t}^{X} (eV)	β_{b}^{X}	β_{t}^{X}
Ag	7.0	3.9	0.96	0.70
Pd	4.7	0.0	1.11	1.00

Bibliography

[1] HUTSEPOT is a Green's function method and developed by A. Ernst *et al.* at the Max Planck Institute of Microstructure Physics, Germany. The basic features were described in M. Lüders et al. "*Ab initio* angle-resolved photoemission in multiple-scattering formulation". *J. Phys.: Condens. Matter* 13 (2001), p. 8587. DOI: 10.1088/0953-8984/13/38/305; A. Ernst. "Multiple-scattering theory: new developments and applications". Kumulative Habilitationsschrift. Martin-Luther-Universität Halle-Wittenberg, 2007.

[2] S. Loth et al. "Bistability in atomic-scale antiferromagnets". *Science* 335 (2012), p. 196. DOI: 10.1126/science.1214131.

[3] A. A. Khajetoorians et al. "Current-driven spin dynamics of artificially constructed quantum magnets". *Science* 339 (2013), p. 55. DOI: 10.1126/science.1228519.

[4] A. J. Heinrich et al. "Single-atom spin-flip spectroscopy." *Science* 306 (2004), p. 466. DOI: 10.1126/science.1101077.

[5] C. F. Hirjibehedin et al. "Large magnetic anisotropy of a single atomic spin embedded in a surface molecular network." *Science* 317 (2007), p. 1199. DOI: 10.1126/science.1146110.

[6] S. Loth et al. "Measurement of fast electron spin relaxation times with atomic resolution." *Science* 329 (2010), p. 1628. DOI: 10.1126/science.1191688.

[7] R. Zeller and P. H. Dederichs. "Electronic Structure of Impurities in Cu, Calculated Self-Consistently by Korringa-Kohn-Rostoker Green's-Function Method". *Phys. Rev. Lett.* 42 (1979), p. 1713. DOI: 10.1103/PhysRevLett.42.1713.

[8] S. Parkin. "Spin-Polarized Current in Spin Valves and Magnetic Tunnel Junctions". *MRS Bull.* 31 (2006), p. 389.

[9] W. F. Egelhoff et al. "Optimizing the giant magnetoresistance of symmetric and bottom spin valves (invited)". *J. Appl. Phys.* 79 (1996), p. 5277. DOI: 10.1063/1.361352.

[10] S. Balamurugan et al. "Specific-heat evidence of strong electron correlations and thermoelectric properties of the ferromagnetic perovskite $SrCoO_{3-\delta}$". *Phys. Rev. B* 74 (2006), p. 172406. DOI: 10.1103/PhysRevB.74.172406.

[11] F. K. Patterson, C. W. Moeller, and R. Ward. "Magnetic oxides of molybdenum(V) and tungsten(V) with the ordered perovskite structure". *Inorg. Chem.* 2 (1963), p. 196. DOI: 10.1021/ic50005a050.

[12] F. S. Galasso, F. C. Douglas, and R. J. Kasper. "Relationship Between Magnetic Curie Points and Cell Sizes of Solid Solutions with the Ordered Perovskite Structure". *J. Chem. Phys.* 44 (1966), p. 1672. DOI: 10.1063/1.1726907.

[13] Y. Tomioka et al. "Magnetic and electronic properties of a single crystal of ordered double perovskite Sr_2FeMoO_6". *Phys. Rev. B* 61 (2000), p. 422. DOI: 10.1103/PhysRevB.61.422.

[14] M. Itoh, I. Ohta, and Y. Inaguma. "Valency pair and properties of 1:1 ordered perovskite-type compounds Sr_2MMoO_6 (M = Mn,Fe,Co)". *Mater. Sci. Eng. B* 41 (1996), p. 55. DOI: 10.1016/S0921-5107(96)01623-6.

[15] P. Paturi, M. Metsänoja, and H. Huhtinen. "Optimization of deposition temperature and atmosphere for pulsed laser deposited Sr_2FeMoO_6 thin films". *Thin Solid Films* 519 (2011), p. 8047. DOI: 10.1016/j.tsf.2011.06.059.

[16] M. Saloaro et al. "Absence of traditional magnetoresistivity mechanisms in Sr_2FeMoO_6 thin films grown on $SrTiO_3$, MgO and $NdGaO_3$ substrates". *J. Phys.: Condens. Matter* 24 (2012), p. 366003. DOI: 10.1088/0953-8984/24/36/366003.

[17] A. B. Muñoz-García, M. Pavone, and E. A. Carter. "Effect of Antisite Defects on the Formation of Oxygen Vacancies in Sr_2FeMoO_6: Implications for Ion and Electron Transport". *Chem. Mater.* 23 (2011), p. 4525. DOI: 10.1021/cm201799c.

[18] P. Soven. "Coherent-Potential Model of Substitutional Disordered Alloys". *Phys. Rev.* 156 (1967), pp. 809–813. DOI: 10.1103/PhysRev.156.809.

[19] B. L. Györffy. "Coherent-Potential Approximation for a Nonoverlapping-Muffin-Tin-Potential Model of Random Substitutional Alloys". *Phys. Rev. B* 5 (1972), p. 2382.

[20] L. Karvonen, H. Yamauchi, and M. Karppinen. "Homologous Series of $SrCoO_{(3n-1)/n}$ Perovskites Obtained Through Br_2 Oxygenation of $SrCoO_{2.5}$". *Chem. Mater.* 20 (2008), p. 7143. DOI: 10.1021/cm801761p.

[21] A. Marmodoro et al. "Generalized inclusion of short-range ordering effects in the coherent potential approximation for complex-unit-cell materials". *Phys. Rev. B* 87 (2013), p. 125115. DOI: 10.1103/PhysRevB.87.125115.

[22] E. K. Délczeg-Czirjak et al. "*Ab initio* study of the elastic anomalies in Pd-Ag alloys". *Phys. Rev. B* 79 (2009), p. 85107. DOI: 10.1103/PhysRevB.84.094205.

[23] E. K. Délczeg-Czirjak et al. "Effect of long-range order on elastic properties of $Pd_{0.5}Ag_{0.5}$ alloy from first principles". *Phys. Rev. B* 84 (2011), p. 094205. DOI: 10.1103/PhysRevB.84.094205.

[24] S. Müller and A. Zunger. "First-Principles Predictions of Yet-Unobserved Ordered Structures in the Ag-Pd Phase Diagram". *Phys. Rev. Lett.* 87 (2001), p. 165502. DOI: 10.1103/PhysRevLett.87.165502.

[25] L. Vegard. "Die Konstitution der Mischkristalle und die Raumfüllung der Atome". *Z. Physik A* 5 (1921), p. 17. DOI: 10.1007/BF01349680.

[26] E. Bruno et al. "Fermi surfaces and electronic topological transitions in metallic solid solutions". *Phys. Rep.* 249 (1994), p. 353. DOI: 10.1016/0370-1573(94)90056-6.

[27] E. Bruno, B. Ginatempo, and E. S. Giuliano. "Fermi surfaces and electronic topological transitions in metallic random alloys. I. The influence on equilibrium properties". *Phys. Rev. B* 52 (1995), p. 14544. DOI: 10.1103/PhysRevB.52.14544.

[28] E. Bruno, B. Ginatempo, and E. S. Giuliano. "Fermi surfaces and electronic topological transitions in metallic random alloys. II. Ag_cPd_{1-c}". *Phys. Rev. B* 52 (1995), p. 14557. DOI: 10.1103/PhysRevB.52.14557.

[29] L. H. Thomas. "The calculation of atomic fields". *Math. Proc. Cambridge* 23 (1927), p. 542. DOI: 10.1017/S0305004100011683.

[30] E. Fermi. "Eine statistische Methode zur Bestimmung einiger Eigenschaften des Atoms und ihre Anwendung auf das Periodensystem der Elemente". *Z. Physik A* 48 (1928), p. 73. DOI: 10.1007/BF01351576.

[31] D. R. Hartree. "The Wave Mechanics of an Atom with a Non-Coulomb Central Field. Part I. Theory and Methods". *Math. Proc. Cambridge* 24 (2008), p. 89. DOI: 10.1017/S0305004100011919.

[32] V. Fock. "Näherungsmethode zur Lösung des quantenmechanischen Mehrkörperproblems". *Z. Physik A* 61 (1930), p. 126. DOI: 10.1007/BF01340294.

[33] P. Hohenberg and W. Kohn. "Inhomogeneous Electron Gas". *Phys. Rev.* 136 (1964), B864. DOI: 10.1103/PhysRev.136.B864.

[34] W. Kohn and L.J. Sham. "Self-consistent equations including exchange and correlation effects". *Phys. Rev.* 140 (1965), A1133.

[35] E. N. Economou. *Green's Functions in Quantum Physics*. Vol. 7. Springer Series in Solid-State Sciences. Berlin Heidelberg: Springer-Verlag, 2006. ISBN: 978-3-540-28841-1. DOI: 10.1007/3-540-28841-4.

[36] J. Zabloudil et al., eds. *Electron Scattering in Solid Matter*. Vol. 147. Springer Series in Solid-State Sciences. Berlin Heidelberg: Springer-Verlag, 2005, p. 382. ISBN: 978-3-540-27001-0. DOI: 10.1007/b138290.

[37] A. Gonis, E. Sowa, and P. Sterne. "Exact treatment of Poisson's equation in solids with space-filling cells". *Phys. Rev. Lett.* 66 (1991), p. 2207. DOI: 10.1103/PhysRevLett.66.2207.

[38] J. Kollár, L. Vitos, and H. L. Skriver. "From ASA Towards the Full Potential". In: *Electronic Structure and Physical Properies of Solids*. Ed. by Hugues Dreyssé. Vol. 535. Lecture Notes in Physics. Berlin Heidelberg: Springer-Verlag, 2000. Chap. 2, p. 85. ISBN: 978-3-540-46437-2. DOI: 10.1007/3-540-46437-9{_}2.

[39] Y. Wang, G.M. Stocks, and J.S. Faulkner. "General method for evaluating shape truncation functions of Voronoi polyhedra". *Phys. Rev. B* 49 (1994), p. 5028. DOI: 10.1103/PhysRevB.49.5028.

[40] J. P. Perdew, K. Burke, and M. Ernzerhof. "Generalized Gradient Approximation Made Simple". *Phys. Rev. Lett.* 77 (1996), p. 3865. DOI: 10.1103/PhysRevLett.77.3865.

[41] J. P. Perdew and Y. Wang. "Accurate and simple analytic representation of the electron-gas correlation energy". *Phys. Rev. B* 45 (1992), p. 13244. DOI: http://dx.doi.org/10.1103/PhysRevB.45.13244.

[42] J. P. Perdew et al. "Restoring the Density-Gradient Expansion for Exchange in Solids and Surfaces". *Phys. Rev. Lett.* 100 (2008), p. 136406. DOI: 10.1103/PhysRevLett.100.136406.

[43] K. Binder and D. W. Heermann. *Monte Carlo Simulation in Statistical Physics: An Introduction*. 5th ed. Graduate Texts in Physics. Berlin Heidelberg: Springer-Verlag, 2010, p. 202. ISBN: 978-3-642-03162-5. DOI: 10.1007/978-3-642-03163-2.

[44] N. Metropolis et al. "Equation of State Calculations by Fast Computing Machines". *J. Chem. Phys.* 21 (1953), p. 1087. DOI: 10.1063/1.1699114.

[45] H. Müller-Krumbhaar and K. Binder. "Dynamic properties of the Monte Carlo method in statistical mechanics". *J. Stat. Phys.* 8 (1973), p. 1. DOI: 10.1007/BF01008440.

[46] D. Liberman, J. T. Waber, and Don T. Cromer. "Self-Consistent-Field Dirac-Slater Wave Functions for Atoms and Ions. I. Comparison with Previous Calculations". *Phys. Rev.* 137 (1965), A27. DOI: 10.1103/PhysRev.137.A27.

[47] M. Richter and H. Eschrig. "Electronic structure of ferromagnetic rare-earth-transition-metal compounds". *Physica B* 172 (1991), p. 85. DOI: 10.1016/0921-4526(91)90420-J.

[48] M.S.S. Brooks, L. Nordström, and B. Johansson. "Rare-earth transition-metal intermetallics". *Physica B* 172 (1991), p. 95. DOI: 10.1016/0921-4526(91)90421-A.

[49] O. V. Farberovich, S. I. Kurganskii, and E. P. Domashevskaya. "Problems of the OPW Method I. Transition Metals". *Phys. Status Solidi B* 94 (1979), p. 51. DOI: 10.1002/pssb.2220940105.

[50] H. Eschrig. *Optimized LCAO Method and the Electronic Structure of Extended Systems*. 1st ed. Research reports in physics. Berlin Heidelberg: Springer-Verlag, 1989, p. 221. ISBN: 978-3-662-02564-2.

[51] M. Hadis and Ü. Özgür. *Zinc Oxide: Fundamentals, Materials and Device Technology*. Weinheim: Wiley-VCH Verlag GmbH & Co. KGaA, 2009. ISBN: 978-3-527-40813-9. DOI: 10.1002/9783527623945.

[52] M. Lüders et al. "Self-interaction correction in multiple scattering theory". *Phys. Rev. B* 71 (2005), p. 205109. DOI: 10.1103/PhysRevB.71.205109.

[53] J. S. Faulkner and G. M. Stocks. "Calculating properties with the coherent-potential approximation". *Phys. Rev. B* 21 (1980), p. 3222. DOI: 10.1103/PhysRevB.21.3222.

[54] G. Fischer et al. "Exchange coupling in transition metal monoxides: Electronic structure calculations". *Phys. Rev. B* 80 (2009), p. 014408. DOI: 10.1103/PhysRevB.80.014408.

[55] Z. Szotek et al. "Electronic structure of half-metallic double perovskites". *Phys. Rev. B* 68 (2003), p. 104411. DOI: 10.1103/PhysRevB.68.104411.

[56] V. I. Anisimov, J. Zaanen, and O. K. Andersen. "Band theory and Mott insulators: Hubbard *U* instead of Stoner *I*". *Phys. Rev. B* 44 (1991), p. 943. DOI: 10.1103/PhysRevB.44.943.

[57] A. Kotani and T. Yamazaki. "Systematic Analysis of Core Photoemission Spectra for Actinide Di-Oxides and Rare-Earth Sesqui-Oxides". *Progr. Theor. Phys. Suppl.* 108 (1992), p. 117. DOI: 10.1143/PTPS.108.117.

[58] S. L. Dudarev et al. "Electron-energy-loss spectra and the structural stability of nickel oxide: An LSDA+*U* study". *Phys. Rev. B* 57 (1998), p. 1505. DOI: 10.1103/PhysRevB.57.1505.

[59] J.-P. Poirier. *Introduction to the Physics of the Earth's Interior*. 2nd ed. Cambridge: Cambridge University Press, 2000, p. 328. ISBN: 978-0-521-66392-2.

[60] L. Vitos. *Computational Quantum Mechanics for Materials Engineers: The EMTO Method and Applications (Engineering Materials and Processes)*. 1st ed. London: Springer-Verlag, 2007, p. 237. ISBN: 978-1-84628-951-4. DOI: 10.1007/978-1-84628-951-4.

[61] F.D. Murnaghan. "The compressibility of media under extreme pressures". *Proc. Natl. Acad. Sci. U.S.A.* 30 (1944), p. 244.

[62] C. L. Fu and K. M. Ho. "First-principles calculation of the equilibrium ground-state properties of transition metals: Applications to Nb and Mo". *Phys. Rev. B* 28 (1983), p. 5480. DOI: 10.1103/PhysRevB.28.5480.

[63] F. Birch. "Finite elastic strain of cubic crystals". *Phys. Rev.* 71 (1947), p. 809. DOI: 10.1103/PhysRev.71.809.

[64] A. R. Oganov and P. I. Dorogokupets. "All-electron and pseudopotential study of MgO: Equation of state, anharmonicity, and stability". *Phys. Rev. B* 67 (2003), p. 224110. DOI: 10.1103/PhysRevB.67.224110.

[65] L. D. Landau and E. M. Lifschitz. *Lehrbuch der theoretischen Physik: Elastizitätstheorie*. Trans. by Benjamin Kozik. 1st ed. Vol. VII. Berlin: Akademie-Verlag GmbH, 1965, p. 183. ISBN: 978-3-817-11336-1.

[66] P. Vinet et al. "A universal equation of state for solids". *J. Phys. C* 19 (1986), p. L467. DOI: 10.1088/0022-3719/19/20/001.

[67] P. Vinet et al. "Universal features of the equation of state of solids". *J. Phys.: Condens. Matter* 1 (1989), p. 1941. DOI: 10.1088/0953-8984/1/11/002.

[68] V. L. Moruzzi, J. F. Janak, and K. Schwarz. "Calculated thermal properties of metals". *Phys. Rev. B* 37 (1988), p. 790. DOI: 10.1103/PhysRevB.37.790.

[69] W. Nolting and A. Ramakanth. *Quantum Theory of Magnetism*. Berlin Heidelberg: Springer-Verlag, 2009, p. 752. ISBN: 978-3-540-85415-9. DOI: 10.1007/978-3-540-85416-6.

[70] M. Getzlaff. *Fundamentals of Magnetism*. 1st ed. Berlin Heidelberg: Springer-Verlag, 2006, p. 388. ISBN: 978-3-540-31150-8. DOI: 10.1007/978-3-540-31152-2.

[71] N. W. Ashcroft and N. D. Mermin. *Festkörperphysik*. Trans. by Jochen Greß. 2nd ed. München: Oldenbourg Wissenschaftsverlag GmbH, 2005, p. 1050. ISBN: 978-3-486-57720-4.

[72] A. I. Liechtenstein et al. "Local spin density functional approach to the theory of exchange interactions in ferromagnetic metals and alloys". *J. Magn. Magn. Mater.* 67 (1987), p. 65. DOI: 10.1016/0304-8853(87)90721-9.

[73] M. Methfessel and J. Kubler. "Bond analysis of heats of formation: application to some group VIII and IB hydrides". *J. Phys. F: Met. Phys.* 12 (1982), p. 141. DOI: 10.1088/0305-4608/12/1/013.

[74] P. Lloyd and P.V. Smith. "Multiple scattering theory in condensed materials". *Adv. Phys.* 21 (1972), p. 69. DOI: 10.1080/00018737200101268.

[75] S. S. A. Razee, J. B. Staunton, and F. J. Pinski. "First-principles theory of magnetocrystalline anisotropy of disordered alloys: Application to cobalt platinum". *Phys. Rev. B* 56 (1997), p. 8082. DOI: 10.1103/PhysRevB.56.8082.

[76] K. W. H. Stevens. "Matrix elements and operator equivalents connected with the magnetic properties of rare earth ions". *Proc. Phys. Soc. A* 65 (1952), p. 209. DOI: 10.1088/0370-1298/65/3/308.

[77] M. Richter et al. "Calculated crystal-field parameters of $SmCo_5$". *Phys. Rev. B* 46 (1992), p. 13919. DOI: 10.1103/PhysRevB.46.13919.

[78] L. Steinbeck. "Elektronische Struktur von Seltenerd-Übergangsmetall-Systemen: *ab initio*-Berechnung von Kristallfeld-Parametern". PhD thesis. Technische Universität Dresden, 1995.

[79] M. T. Hutchings. "Point-Charge Calculations of Energy Levels of Magnetic Ions in Crystalline Electric Fields". In: *Solid State Physics*. Ed. by F. Seitz and D. Turnbull. Vol. 16. Solid State Physics. New York: Academic Press Inc., 1964, p. 227. ISBN: 978-0-12-607716-2. DOI: 10.1016/S0081-1947(08)60517-2.

[80] M. M. Otrokov et al. "Intralayer magnetic ordering in Ge/Mn digital alloys". *Phys. Rev. B* 83 (2011), p. 155203. DOI: 10.1103/PhysRevB.83.155203.

[81] M. M. Otrokov et al. "*Ab initio* study of the magnetic ordering in Si/Mn digital alloys". *Phys. Rev. B* 84 (2011), p. 144431. DOI: 10.1103/PhysRevB.84.144431.

[82] O. E. Peil, A. V. Ruban, and B. Johansson. "Self-consistent supercell approach to alloys with local environment effects". *Phys. Rev. B* 85 (2012), p. 165140. DOI: 10.1103/PhysRevB.85.165140.

[83] J. Cowley. "An Approximate Theory of Order in Alloys". *Phys. Rev.* 77 (1950), p. 669. DOI: 10.1103/PhysRev.77.669.

[84] B. E. Warren. *X-ray diffraction*. New York: Dover Publications, Inc., 1990, p. 381. ISBN: 978-0-486-66317-3.

[85] B. C. Anusionwu. "Concentration Fluctuations and Chemical Complexes in the Zn-Au Liquid Alloy". *Phys. Chem. Liq.* 38 (2000), p. 671. DOI: 10.1080/00319100008030314.

[86] F. Ducastelle. *Order and Phase Stability in Alloys*. Vol. 3. Cohesion and structure. Amsterdam: North-Holland, 1991, p. 511. ISBN: 978-0-444-86973-9.

[87] R. Mills, L. J. Gray, and T. Kaplan. "Analytic approximation for random muffin-tin alloys". *Phys. Rev. B* 27 (1983), p. 3252. DOI: 10.1103/PhysRevB.27.3252.

[88] B. Ginatempo and J. B. Staunton. "The electronic structure of disordered alloys containing heavy elements-an improved calculational method illustrated by a study of a copper-gold alloy". *J. Phys. F: Met. Phys.* 18 (1988), p. 1827. DOI: 10.1088/0305-4608/18/8/018.

[89] A. J. Pindor, W. M. Temmerman, and B. L. Györffy. "KKR CPA for two atoms per unit cell: application to Pd and PdAg hydrides". *J. Phys. F: Met. Phys.* 13 (1983), p. 1627. DOI: 10.1088/0305-4608/13/8/009.

[90] J. B. Staunton et al. "The "disordered local moment" picture of itinerant magnetism at finite temperatures". *J. Magn. Magn. Mater.* 45 (1984), p. 15. DOI: 10.1016/0304-8853(84)90367-6.

[91] B. L. Gyorffy et al. "A first-principles theory of ferromagnetic phase transitions in metals". *J. Phys. F: Met. Phys.* 15 (1985), p. 1337. DOI: 10.1088/0305-4608/15/6/018.

[92] J. B. Staunton and B. L. Gyorffy. "Onsager cavity fields in itinerant-electron paramagnets". *Phys. Rev. Lett.* 69 (1992), p. 371. DOI: 10.1103/PhysRevLett.69.371.

[93] J. B. Staunton, A. Marmodoro, and A. Ernst. "Using density functional theory to describe slowly varying fluctuations at finite temperatures: local magnetic moments in Gd and the 'not so local' moments of Ni." *J. Phys.: Condens. Matter* 26 (2014), p. 274210. DOI: 10.1088/0953-8984/26/27/274210.

[94] D. A. Rowlands et al. "Density functional theory for disordered alloys with short-range order: Systematic inclusion of charge-correlation effects". *Phys. Rev. B* 73 (2006), p. 165122. DOI: 10.1103/PhysRevB.73.165122.

[95] M. Jarrell and H. Krishnamurthy. "Systematic and causal corrections to the coherent potential approximation". *Phys. Rev. B* 63 (2001), p. 125102. DOI: 10.1103/PhysRevB.63.125102.

[96] N. Takano. "First-principles calculations of short-range order parameters in $Ag_{0.5}Pd_{0.5}$ alloy". *Solid State Commun.* 107 (1998), p. 213. DOI: 10.1016/S0038-1098(98)00199-9.

[97] I. Mirebeau, M. Hennion, and G. Parette. "First Measurement of Short-Range-Order Inversion as a Function of Concentration in a Transition Alloy". *Phys. Rev. Lett.* 53.7 (1984), p. 687. DOI: 10.1103/PhysRevLett.53.687.

[98] P. E. Blöchl. "Projector augmented-wave method". *Phys. Rev. B* 50 (1994), p. 17953. DOI: 10.1103/PhysRevB.50.17953.

[99] G. Kresse and J. Hafner. "*Ab initio* molecular-dynamics simulation of the liquid-metal–amorphous-semiconductor transition in germanium". *Phys. Rev. B* 49 (1994), p. 14251. DOI: 10.1103/PhysRevB.49.14251.

[100] G. Kresse and J. Furthmüller. "Efficiency of *ab initio* total energy calculations for metals and semiconductors using a plane-wave basis set". *Comp. Mater. Sci.* 6 (1996), p. 15. DOI: 10.1016/0927-0256(96)00008-0.

[101] J. Hafner. "*Ab initio* simulations of materials using VASP: Density-functional theory and beyond." *J. Comp. Chem.* 29 (2008), p. 2044. DOI: 10.1002/jcc.21057.

[102] B. G. Wybourne. *Spectroscopic Properties of Rare Earths*. New York: Interscience Publishers (John Wiley & Sons, Inc.), 1965, p. 236. ISBN: 978-0-470-96507-8.

[103] P. Bezdicka et al. "Preparation and characterization of Fully stoichiometric $SrCoO_3$ by electrochemical oxidation". *Z. anorg. allge. Chem.* 619 (1993), p. 7. DOI: 10.1002/zaac.19936190104.

[104] Y. Long et al. "Synthesis of cubic $SrCoO_3$ single crystal and its anisotropic magnetic and transport properties." *J. Phys.: Condens. Matter* 23 (2011), p. 245601. DOI: 10.1088/0953-8984/23/24/245601.

[105] L. Karvonen et al. "Chemical Oxidation of $SrCoO_{3-\delta}$". *Chem. Lett.* 36 (2007), p. 1176. DOI: 10.1246/cl.2007.1176.

[106] The picture of the structure, bonds and polyhedra was done with the visualization program VESTA described in K. Momma and F. Izumi. "VESTA 3 for three-dimensional visualization of crystal, volumetric and morphology data". *J. Appl. Crystallogr.* 44.6 (2011), p. 1272. DOI: 10.1107/S0021889811038970.

[107] J. Kuneš et al. "Spin State of Negative Charge-Transfer Material $SrCoO_3$". *Phys. Rev. Lett.* 109 (2012), p. 117206. DOI: 10.1103/PhysRevLett.109.117206.

[108] R. H. Potze, G. A. Sawatzky, and M. Abbate. "Possibility for an intermediate-spin ground state in the charge-transfer material $SrCoO_3$". *Phys. Rev. B* 51 (1995), p. 11501. DOI: 10.1103/PhysRevB.51.11501.

[109] J. H. Lee and K. M. Rabe. "Coupled magnetic-ferroelectric metal-insulator transition in epitaxially strained $SrCoO_3$ from first principles". *Phys. Rev. Lett.* 107 (2011), p. 067601. DOI: 10.1103/PhysRevLett.107.067601.

[110] H.-P. Wu et al. "Electronic and magnetic properties of $SrCoO_3$: The first principles study". *Acta Phys. Sin.* 61 (2012), p. 037101. DOI: 10.7498/aps.61.037101.

[111] T. Takeda and H. Watanabe. "Magnetic Properties of the System $SrCo_{1-x}Fe_xO_{3-y}$". *J. Phys. Soc. Jpn.* 33 (1972), p. 973. DOI: 10.1143/JPSJ.33.973.

[112] S. Balamurugan. "Impact of High Pressure and High Temperature on Annealed Oxygen-deficient $CoSrO_{3-\delta}$ Perovskites: Structural and Magnetization Studies". *J. Supercond. Nov. Magn.* 23 (2010), p. 225. DOI: 10.1007/s10948-009-0519-0.

[113] R. Le Toquin et al. "Time-resolved in situ studies of oxygen intercalation into $SrCoO_{2.5}$, performed by neutron diffraction and x-ray absorption spectroscopy." *J. Amer. Chem. Soc.* 128 (2006), p. 13161. DOI: 10.1021/ja063207m.

[114] A. Nemudry, P. Rudolf, and R. Schöllhorn. "Topotactic electrochemical redox reactions of the defect perovskite $SrCoO_{2.5+x}$". *Chem. Mater.* 4756 (1996), p. 2232. DOI: 10.1021/cm950504+.

[115] Y. Moritomo et al. "Crystal and Magnetic Structure of Conducting Double Perovskite Sr_2FeMoO_6". *J. Phys. Soc. Jpn.* 69 (2000), p. 1723. DOI: 10.1143/JPSJ.69.1723.

[116] Y. Moritomo et al. "Electron doping effects in conducting Sr_2FeMoO_6". *Phys. Rev. B* 62 (2000), p. 14224. DOI: 10.1103/PhysRevB.62.14224.

[117] S.-I. Park et al. "Neutron diffraction and magnetic properties of $Sr_2Fe_{0.9}Cr_{0.1}MoO_6$". *Physica B* 345 (2004), p. 99. DOI: 10.1016/j.physb.2003.11.032.

[118] S. B. Kim, B. W. Lee, and C. S. Kim. "Neutron and Mössbauer studies of the double perovskite A_2FeMoO_6 (A = Sr and Ba)". *J. Magn. Magn. Mater.* 242-245 (2002), p. 747. DOI: 10.1016/S0304-8853(01)01015-0.

[119] E. Burzo et al. "The effects of thermal treatment on the physical properties of $Sr_2FeMo_{1-x}M_xO_6$ perovskite with M = W, Ta and $x \leq 0.3$". *J. Alloys Comp.* 509 (2011), p. 105. DOI: 10.1016/j.jallcom.2010.08.126.

[120] S. Nakamura and K. Oikawa. "Precise Structure Analysis Consistent with Mössbauer Quadrupole Effect: A Case of the Ordered Double Perovskites Sr_2FeMO_6 (M = Mo and Re)". *J. Phys. Soc. Jpn.* 72 (2003), p. 3123. DOI: 10.1143/JPSJ.72.3123.

[121] Y. Zhai et al. "Synthesis, magnetic and electrical transport properties of magnetoresistance material Sr_2FeMoO_6 by microwave sintering". *J. Magn. Magn. Mater.* 324 (2012), p. 2006. DOI: 10.1016/j.jmmm.2012.01.029.

[122] A. K. Azad et al. "Electron doping effect on structural and magnetic phase transitions in $Sr_{2-x}Nd_xFeMoO_6$ double perovskites". *J. Solid State Chem.* 179 (2006), p. 1303. DOI: 10.1016/j.jssc.2006.01.043.

[123] C. Meneghini et al. "Nature of "disorder" in the ordered double perovskite Sr_2FeMoO_6". *Phys. Rev. Lett.* 103 (2009), p. 046403. DOI: 10.1103/PhysRevLett.103.046403.

[124] R. Kircheisen and J. Töpfer. "Nonstoichiometry, point defects and magnetic properties in $Sr2FeMoO_{6-\delta}$ double perovskites". *J. Solid State Chem.* 185 (2012), p. 76. DOI: 10.1016/j.jssc.2011.10.043.

[125] T. Yamamoto et al. "Novel methods of synthesis and wet-chemical redox analysis for magnetoresistive double-perovskite Sr_2FeMoO_{6-w}". *J. Mater. Chem.* 10 (2000), p. 2342. DOI: 10.1039/b003640o.

[126] S. Colis et al. "Structural defects in Sr_2FeMoO_6 double perovskite: Experimental versus theoretical approach". *J. Appl. Phys.* 98 (2005), p. 033905. DOI: 10.1063/1.1997286.

[127] K.-I. Kobayashi et al. "Room-temperature magnetoresistance in an oxide material with an ordered double-perovskite structure". *Nature* 395 (1998), p. 677. DOI: 10.1038/27167.

[128] D. D. Sarma et al. "Electronic Structure of Sr_2FeMoO_6". *Phys. Rev. Lett.* 85 (2000), p. 2549. DOI: 10.1103/PhysRevLett.85.2549.

[129] T. Saitoh et al. "Half-metallic density of states in Sr_2FeMoO_6 due to Hund's rule coupling". *Phys. Rev. B* 66 (2002), p. 035112. DOI: 10.1103/PhysRevB.66.035112.

[130] R. P. Panguluri et al. "Disorder effects in half-metallic Sr_2FeMoO_6 single crystals". *Appl. Physics Lett.* 94 (2009), p. 012501. DOI: 10.1063/1.3058441.

[131] T. Saha-Dasgupta and D. D. Sarma. "*Ab initio* study of disorder effects on the electronic and magnetic structure of Sr_2FeMoO_6". *Phys. Rev. B* 64 (2001), p. 064408. DOI: 10.1103/PhysRevB.64.064408.

[132] Z. Fang, K. Terakura, and J. Kanamori. "Strong ferromagnetism and weak antiferromagnetism in double perovskites: Sr_2FeMO_6 (M = Mo, W, and Re)". *Phys. Rev. B* 63 (2001), p. 180407. DOI: 10.1103/PhysRevB.63.180407.

[133] H.-T. Jeng and G. Y. Guo. "First-principles investigations of orbital magnetic moments and electronic structures of the double perovskites Sr_2FeMoO_6, Sr_2FeReO_6, and Sr_2CrWoO_6". *Phys. Rev. B* 67 (2003), p. 094438. DOI: 10.1103/PhysRevB.67.094438.

[134] V. Kanchana et al. "Electronic structure and x-ray magnetic circular dichroism of Sr_2FeMoO_6: *Ab initio* calculations". *Phys. Rev. B* 75 (2007), p. 220404. DOI: 10.1103/PhysRevB.75.220404.

[135] M. Besse et al. "Experimental evidence of the ferrimagnetic ground state of Sr_2FeMoO_6 probed by x-ray magnetic circular dichroism". *Europhys. Lett.* 60 (2002), p. 608. DOI: 10.1209/epl/i2002-00262-4.

[136] T. Koide et al. "Microscopic origin of ferrimagnetism of a double perovskite Sr_2FeMoO_6: An x-ray magnetic circular dichroism study". *J. Phys.: Confer. Ser.* 502 (2014), p. 12003. DOI: 10.1088/1742-6596/502/1/012003.

[137] B. García-Landa et al. "Magnetic and magnetotransport properties of the ordered perovskite Sr_2FeMoO_6". *Solid State Commun.* 110 (1999), p. 435. DOI: 10.1016/S0038-1098(99)00079-4.

[138] A. S. Ogale et al. "Octahedral cation site disorder effects on magnetization in double-perovskite Sr_2FeMoO_6: Monte Carlo simulation study". *Appl. Physics Lett.* 75 (1999), p. 537. DOI: 10.1063/1.124440.

[139] Ll. Balcells et al. "Cationic ordering control of magnetization in Sr_2FeMoO_6 double perovskite". *Appl. Physics Lett.* 78 (2001), p. 781. DOI: 10.1063/1.1346624.

[140] J. Navarro et al. "Raising the Curie temperature in Sr_2FeMoO_6 double perovskites by electron doping". *Phys. Rev. B* 64 (2001), p. 092411. DOI: 10.1103/PhysRevB.64.092411.

[141] B. R. Coles. "The lattice spacings of Nickel-Copper and Palladium-Silver alloys". *J. Inst. Met.* 84 (1955), p. 346.

[142] A. G. Every and A. K. McCurdy. *Second and Higher Order Elastic Constants*. Ed. by D. F. Nelson. Vol. 29a. Landolt-Börnstein - Group III Condensed Matter. Berlin Heidelberg: Springer-Verlag, 1992. ISBN: 978-3-540-47609-2. DOI: 10.1007/b44185.

[143] L. Vitos et al. "Application of the exact muffin-tin orbitals theory: the spherical cell approximation". *Comp. Mater. Sci.* 18 (2000), p. 24. DOI: 10.1016/S0927-0256(99)00098-1.

[144] L. Vitos. "Total-energy method based on the exact muffin-tin orbitals theory". *Phys. Rev. B* 64 (2001), p. 014107. DOI: 10.1103/PhysRevB.64.014107.

[145] L. Vitos, P. A. Korzhavyi, and B. Johansson. "Stainless steel optimization from quantum mechanical calculations". *Nat. Mater.* 2 (2002), p. 25. DOI: 10.1038/nmat790.

[146] A. V. Ruban et al. "Theroretical investigation of bulk ordering and surface segregation in Ag-Pd and other isoelectronic alloys". *Phys. Rev. B* 75 (2007), p. 54113. DOI: 10.1103/PhysRevB.75.054113.

[147] A. Marmodoro. "Beyond single-site disorder effects in first-principles studies of solid state systems". PhD thesis. University of Warwick, 2011.

[148] A. D. McLachlan et al. "A valence band study of Ag-Pd alloys using ultraviolet photoelectron spectroscopy". *J. Phys. F: Met. Phys.* 2415 (1975), p. 2415. DOI: 10.1088/0305-4608/5/12/028.

[149] S. Hüfner, G. K. Wertheim, and J. Wernick. "X-Ray Photoelectron Spectra of the Valence Bands of Some Transition Metals and Alloys". *Phys. Rev. B* 8 (1973), p. 4511. DOI: 10.1103/PhysRevB.8.4511.

[150] C. Caroli et al. "Inelastic Effects in Photoemission: Microscopic Formulation and Qualitative Discussion". *Phys. Rev. B* 8 (1973), p. 4552. ISSN: 0556-2805. DOI: 10.1103/PhysRevB.8.4552.

[151] C. Norris and P. O. Nilsson. "Photoemission from Pd". *Solid State Commun.* 6 (1968), p. 649. DOI: 10.1016/0038-1098(68)90186-5.

[152] S. Hüfner, G. K. Wertheim, and J. H. Wernick. "Virtual bound states of Pd in Cu, Ag and Au and of Pt in Ag". *Solid State Commun.* 17 (1975), p. 1585. DOI: 10.1016/0038-1098(75)91001-7.

[153] K. H. Chae et al. "Charge redistribution in ion-beam-mixed PdAg alloys". *Nucl. Instr. Meth. Phys. Res. B* 117 (1996), p. 123. DOI: 10.1016/0168-583X(96)00293-5.

[154] A. M. Tarditi, M. L. Bosko, and L. M. Cornaglia. "Alloying and surface composition of model Pd–Ag films synthesized by electroless deposition". *Int. J. Hydrogen Energy* 37 (2012), p. 6020. DOI: 10.1016/j.ijhydene.2011.12.128.

Eigene Veröffentlichungen

Teile dieser Arbeit sind bereits veröffentlicht.
Alle Veröffentlichungen sind absteigend nach Jahren sortiert.

[E1] Guntram Fischer et al. "*Ab initio* study of the *p*-Hole Magnetism at Polar Surfaces of ZnO: the Role of Correlations". Submitted to *J. Phys.: Condens. Matter* (2015).

[E2] Martin Hoffmann et al. "Impact of lattice defects and electron correlations on the magnetic properties of Sr_2FeMoO_6". ArXiv: 1504.02629. Submitted to *Phys. Rev. B* (2015).

[E3] Minnamari Saloaro et al. "Towards high Curie temperatures in Sr_2FeMoO_6 thin films". Submitted to *Adv. Mater.* (2015).

[E4] Martin Hoffmann et al. "Magnetic properties of defect-free and oxygen-deficient cubic $SrCoO_{3-\delta}$". *Phys. Rev. B* 92 (2015), p. 094427. DOI: 10.1103/PhysRevB.92.094427.

[E5] Martin Hoffmann et al. "Study of electronic and magnetic properties and related x-ray absorption spectroscopy of ultrathin Co films on $BaTiO_3$". *J. Phys.: Condens. Matter* 27 (2015), p. 426003. DOI: 10.1088/0953-8984/27/42/426003.

[E6] Israel Lorite et al. "Advances in methods to obtain and characterise room temperature magnetic ZnO". *Appl. Physics Lett.* 106 (2015), p. 082406. DOI: 10.1063/1.4913763.

[E7] Israel Lorite et al. "Study of the negative magneto-resistance of single proton-implanted lithium-doped ZnO microwires". *J. Phys.: Condens. Matter* 27 (2015), p. 256002. DOI: 10.1088/0953-8984/27/25/256002.

[E8] Claudia E. Rodríguez Torres et al. "Oxygen-vacancy-induced local ferromagnetism as a driving mechanism in enhancing the magnetic response of ferrites". *Phys. Rev. B* 89 (2014), p. 104411. DOI: 10.1103/PhysRevB.89.104411.

[E9] Sumalay Roy et al. "X-ray analysis of wurtzite-type CoO(111) films on Ir(001): Correlation of structure, stress, electronic, and magnetic properties". *Phys. Rev. B* 89 (2014), p. 165428. DOI: 10.1103/PhysRevB.89.165428.

[E10] Maia G. Vergniory et al. "Exchange interaction and its tuning in magnetic binary chalcogenides". *Phys. Rev. B* 89 (2014), p. 165202. DOI: 10.1103/PhysRevB.89.165202.

[E11] Toshio Miyamachi et al. "Stabilizing the magnetic moment of single holmium atoms by symmetry". *Nature* 503 (2013), p. 242. DOI: 10.1038/nature12759.

[E12] Martin Hoffmann et al. "Elastic anomalies and long/short-range ordering effects: A first-principles investigation of the Ag_cPd_{1-c} solid solution". *Phys. Rev. B* 86 (2012), p. 094106. DOI: 10.1103/PhysRevB.86.094106.

[E13] Tobias Schuh et al. "Magnetic excitations of rare Earth atoms and clusters on metallic surfaces". *Nano Lett.* 12 (2012), p. 4805. DOI: 10.1021/nl302250n.

[E14] Robert Speck, Paul Gibbon, and Martin Hoffmann. "Efficiency and scalability of the parallel Barnes-Hut tree code PEPC". In: *Parallel Computing: From Multicores and GPU's to Petascale*. Ed. by Barbara Chapman et al. Vol. 19. Advances in Parallel Computing. Amsterdam: IOS Press, 2010, p. 35. ISBN: 978-1-60750-530-3. DOI: 10.3233/978-1-60750-530-3-35.

[E15] Martin Hoffmann. "Structure Analysis of Communication and Memory Behavior in the Parallel Tree Code PEPC". In: *Beiträge zum Wissenschaftlichen Rechnen Ergebnisse des Gaststudentenprogramms 2008 des John von Neumann-Instituts für Computing*. Ed. by Matthias Bolten. Interner Bericht: FZJ-JSC-IB-2008-07. Jülich: Forschungszentrum Jülich GmbH, 2008, p. 27.

Danksagung

An dieser Stelle möchte ich gerne in Deutsch meinen Dank an all jene Personen aussprechen, die mich in den letzten Jahren auf meinem Weg begleitet haben. Ohne ihre kontinuierliche Unterstützung und Zusprache hätte ich die Arbeit nicht abschließen können.

Daher möchte ich mich zunächst bei meinen beiden Betreuern Herrn Prof. Wolfram Hergert und Herrn PD Arthur Ernst bedanken. Beide haben mich schon seit meines Studiums und auch beim Schreiben meiner Diplomarbeit begleitet. Sie hatten immer ein offenes Ohr für mich. Ich erinnere mich gerne an rege Diskussionen bei Tee und Keksen oder die Grillabende am Von-Seckendorff-Platz. Zusätzlich ermöglichten sie mir einen regen Austausch mit wissenschaftlichen Instituten in und außerhalb von Deutschland und zahlreiche Möglichkeiten auf wissenschaftlichen Konferenzen meine Ergebnisse zupräsentieren. Dadurch hatte ich die Gelegenheit in Argentinien die Universität von La Plata kennen zu lernen oder in Finnland der Universität von Turku regelmäße Besuche zum wissenschaftlichen Diskurs abzustatten. Bei diesen Gelegenheiten durfte ich viele neue Kollegen kennenlernen. Diesen möchte ich an dieser Stelle für ihre Gastfreundschaft und wissenschaftliche Zusammenarbeit danken: Eero Nurmi, Kalevi Kokko, Minnamari Saloaro, Petriina Paturi, Marko Punkkinen, Hannu Huhtinen, Levente Vitos, Claudia Rodríguez Torres, Karen Lizeth Salcedo und Silvana Stewart.

Des weiteren möchte ich mich bei den Kollegen vom Institut für Physik der Martin-Luther-Universität Halle-Wittenberg und vom Max-Planck-Institut für Mikrostrukturphysik für ein angenehmes und produktives Arbeitsklima im Büro und darüber hinaus bedanken. Dabei spreche ich besonders Sanjeev Kumar Nayak, Guntram Fischer, Waheed A. Adeagbo, Matthias Geilhufe, Stefan Thomas, Martin Hölzer und Falk Tandentzky an.

Neben dem Schreiben der Arbeit habe ich eine große Freude am Gesellschaftstanz entwickelt. Auf die Gefahr hin, dass ich jemand vergessen könnte, werde ich nicht alle beim Namen nennen. Ich bedanke mich aber bei allen Tänzerinnen und Tänzern des Formationskurses des Universitätssportzentrums, die im Laufe der Zeit zu einem wichtigen Bestandteil meines Lebens geworden sind. Die unzähligen Auftritte, Tanzkurse und geselligen Abende stellen eine unvergessliche Bereicherung dar, die ich nicht mehr missen möchte.

Zu guter Letzt möchte ich allen meinen Freunden, meinen Eltern und der übrigen Familie meinen Dank, auch wenn dieser kaum in Worte gefasst werden kann, ausdrücken. Ihr Rat und Tat, ihre Motivation und Unterhaltung sind und bleiben für mich unersätzlich. Danke!

Lebenslauf

Name: Martin Hoffmann
Staatsangehörigkeit: deutsch
Geburtsdatum: 25. Dezember 1984
Geburtsort: Querfurt

STUDIUM

seit 11/2010	Promotionsstudium Martin-Luther-Universität Halle-Wittenberg
11/2009 – 11/2010	Diplomarbeit: "Einfluss von Nahfeldkorrekturen und Nahordnungseffekten auf die elektronischen Eigenschaften binärer Legierungen"
10/2005 – 11/2010	Studium Diplom Physik Martin-Luther-Universität Halle-Wittenberg
08/2008 – 10/2008	Gaststudentenprogramm 2008 am Jülich Supercomputing Centre, Forschungszentrum Jülich Thema: "Structure Analysis of Communication and Memory Behavior in the Parallel Tree Code PEPC"

WEHRDIENST

07/2004 – 03/2005	Regionales Instandsetzungszentrum Celle

SCHULE

1995 – 2004	Allgemeine Hochschulreife Südstadt Gymnasium, Halle (Saale)
1991 – 1995	Grundschule Carl-Friedrich-Gauß, Halle (Saale)

Eidesstattliche Erklärung

Ich erkläre an Eides statt, gemäß §5 der Promotionsordnung der Naturwissenschaftlichen Fakultät II der Martin-Luther-Universität Halle-Wittenberg vom 13. Juni 2012, dass ich die vorliegende Arbeit

Multiple scattering theory for the description of defects in metallic alloys and oxide systems

selbständig und ohne fremde Hilfe verfasst, sowie keine als die von mir angegebenen Quellen und Hilfsmittel benutzt und die den benutzten Werken wörtlich oder inhaltlich entnommenen Stellen als solche kenntlich gemacht habe. Weiterhin erkläre ich, dass ich bisher keine vergeblichen Promotionsversuche unternommen habe und die Arbeit in gleicher oder ähnlicher Form weder einer anderen Prüfungsbehörde vorgelegt, noch veröffentlicht wurde.

Halle (Saale), den 2. November 2015

Martin Hoffmann